FOSSIL ENERGY

DOE/BC/14126-4
(DE88001248)

THE EFFECT OF METALLIC ADDITIVES ON THE KINETICS OF OIL OXIDATION REACTIONS IN IN-SITU COMBUSTION

Supri TR 63

By
C.F. De los Rios
W.E. Brigham
L.M. Castanier

November 1988

Performed Under Contract No. FG19-87BC14126

Stanford University Petroleum Research Institute
Stanford, California

Bartlesville Project Office
U. S. DEPARTMENT OF ENERGY
Bartlesville, Oklahoma

DISCLAIMER

Printed in the United States of America. Available from:
National Technical Information Service
U.S. Department of Commerce
5285 Port Royal Road
Springfield, VA 22161

NTIS price codes
Paper copy: **A05**
Microfiche copy: **A01**

DOE/BC/14126-4
Distribution Category UC-122

THE EFFECT OF METALLIC ADDITIVES ON THE KINETICS OF OIL OXIDATION REACTIONS IN IN-SITU COMBUSTION

Supri TR 63

By
C.F. De los Rios
W.E. Brigham
L.M. Castanier

November 1988

Work Performed Under Contract No. FG19-87BC14126

Prepared for
U.S. Department of Energy
Assistant Secretary for Fossil Energy

Thomas B. Reid, Project Manager
Bartlesville Project Office
P.O. Box 1398
Bartlesville, OK 74005

Prepared by
Stanford University Petroleum Research Institute
Stanford, CA 94305-4042

TABLE OF CONTENTS

LIST OF TABLES

LIST OF FIGURES

ACKNOWLEDGEMENTS

This author gratefully acknowledges the financial support received from Stanford University Petroleum Research Institute, under DOE contract DE-FG19-87BZ14126.

ABSTRACT

In-situ combustion is a process whose applicability is partly determined by the combustion characteristics of the specific crude oil in question. These characteristics are directly influenced by the rate of oxidation reactions occurring in the rock matrix ahead of the combustion front. A method is therefore sought by which these characteristics may be altered within a reservoir, thus making the process feasible for a wider variety of crude oils. The presence of catalysts may have a significant influence on the reactions. The effects of catalyzing agents on the kinetics of these reactions were therefore studied to gain a more thorough understanding of the mechanisms involved in the catalysis of crude oil oxidation.

Experiments were conducted wherein samples of a Huntington Beach oil/sand mixture were subjected to a continuous flow of air and a linear heating schedule. The effects of differing operating pressure and ten different metallic additives were examined in an experimental program of sixteen runs.

Oxygen consumption data from the kinetic experiments were analyzed by decoupling the total oxygen consumption curve into three parts representing the three competing oxidation reactions. A curve fitting algorithm was devised in order to standardize the procedure by which the temperature ranges were chosen that characterize each reaction. This algorithm resulted in data matches that were quite good near the reaction peaks, but that were poor in the temperature range between the medium and high temperature peaks. As a consequence, the kinetic parameters determined through this procedure failed to show trends consistent enough to quantitatively assess the effects of the metallic additives. These effects were therefore evaluated through visual comparisons of the effluent gas composition data in combination with comparisons of the reaction rates, as illustrated in Arrhenius graphs.

1. INTRODUCTION

The viability of any enhanced oil recovery process is dictated by the compatibility of the recovery mechanisms, which limit the technical success of each method, with the crude oil properties and reservoir characteristics of each field. In general, four basic mechanisms exist for recovering oils from porous media more effectively than from water injection alone. These mechanisms are: the reduction of interfacial tension between oil and water, the extraction of oil with a solvent, the reduction of mobility of the injection fluids, and the thermal reduction of oil viscosity. The later mechanism is, on the whole, the most effective in improving recovery from low gravity, heavy oil reservoirs.

Thermal energy may be introduced into an oil reservoir by means of injected fluids (usually steam), or it may be generated in-situ by burning a portion of the crude oil. In-situ combustion is generally the more complex of the two processes and can also be plagued with a number of operating problems such as corrosion, erosion, and pipe failures resulting from high temperatures at production wells. Consequently, steam injection has been the preferred thermal recovery method. Steam injection, however, is usually not considered viable for reservoirs at depths greater than 2500 feet due to excessive wellbore heat losses, and the danger of casing failure at the higher temperatures required at greater depths.

As with steam injection, in-situ combustion stimulates oil production by lowering the oil's viscosity and improving its mobility. In addition, the oil is subjected to gas drive from combustion gases, steam drive in the steam plateau ahead of the combustion front, hot water drive from condensing steam, and miscible displacement from recondensing light hydrocarbons (Wilson *et. al.*, 1958; Nelson and McNeil, 1959). Thermal cracking and some catalytic cracking also results in a slight increase in the API gravity of the oil. Since heat is generated inside the reservoir, the process can generally be carried out in deeper reservoirs and thinner, tighter sand sections where heat losses for steam injection are too great. An additional appeal for in-situ combustion comes from the fact that it uses inexpensive and plentiful fluids for injection: air and water.

A chief constraint limiting the applicability of in-situ combustion is the propensity of an oil for fuel formation in the reservoir matrix ahead of the combustion zone. If sufficient fuel is not deposited (high gravity oils), the combustion front will not be self-sustaining. Conversely, if excessive fuel is deposited (very low gravity oils), the rate of advance of the front will be slow and the quantity of air required to sustain combustion will be uneconomically high. It follows, therefore, that if this inclination for fuel deposition could be altered for a given oil, the process could be made feasible for a wider variety of crude oils.

The amount of fuel formation and the velocity of combustion front propagation are dictated by the kinetics of the oil oxidation and pyrolysis reactions that control the process. The presence of catalysts may have a significant influence on the extent and nature of these reactions and hence may directly affect the success of an in-situ combustion process. The introduction of catalyzing agents (ie., water soluble metallic compounds) should therefore be investigated as a means of artificially regulating the fuel formation and combustion characteristics of a crude oil within a reservoir.

2. LITERATURE REVIEW

The kinetics of crude oil oxidation reactions involved in in-situ combustion has been the subject of many investigations. Measurement of kinetic parameters has been achieved by oxidizing crude oil in packed beds under a heating schedule and analyzing the effluent gases (Bousaid and Ramey, 1968; Weijdema, 1968; Burger and Sahuquet, 1972; Dabbous and Fulton, 1974; Thomas *et. al.*, 1979; Fassihi, 1981). These studies have established that the overall oxidation mechanism of crude oils in porous media is the result of an overlap of several competing reactions occurring over different temperature ranges. These reactions can be grouped into three sequences:

1. Low-temperature oxidation reactions, which are heterogeneous (gas-liquid) and produce no carbon oxides.
2. Medium-temperature "fuel deposition" reactions, which are homogeneous (gas phase), involving the oxidation of the products of distillation and pyrolysis.
3. High-temperature fuel combustion reactions, which are heterogeneous (gas-solid), where oxygen reacts with the heavy coke-like residue deposited at lower temperatures.

2.1. LOW-TEMPERATURE OXIDATION

Low-temperature oxidation (LTO) can occur in an in-situ combustion process when combustion rates are insufficient to consume all of the oxygen in the high-temperature burn zone or when high permeability streaks enable oxygen to travel so rapidly through the combustion zone that it contacts insufficient fuel for complete oxygen utilization. LTO results in the production of partially oxygenated compounds such as carboxylic acids, aldehydes, ketones, alcohols, and hydroperoxides along with the associated production of water (Burger and Sahuquet, 1972). This partial oxidation alters fluid properties critical to the displacement process; namely, the viscosity and the boiling range are increased (Alexander *et. al.*, 1962; Bousaid and Ramey, 1968). In addition, several investigators have shown that fuel deposition increases in the presence of LTO reactions. Alexander *et. al.* (1962) demonstrated that gross fuel availability, in terms of net pounds of carbon consumed per pound of sand, can vary by a factor of three depending on the degree of LTO. Similarly, in one dimensional experimental simulation runs, Dabbous and Fulton (1974) observed a 22 percent increase in fuel deposition when LTO was permitted to occur. In contrast, however, Abu-Khamsin (1985) compared residual hydrocarbons recovered from oxidation runs to those recovered from pyrolysis runs and found reductions in residual oil ranging from 10.4 percent of the original oil in place, at a temperature of 502°K, to 3.25 percent at a temperature of 660°K. This inconsistency with other studies was attributed to a difference in operating procedures. Namely, continuous oxygen exposure at increasing temperatures caused continuous loss of oil to oxidation. Hence, smaller quantities of residual oil were deposited in comparison to the residual oil left when nonoxidizing gas was used while heating.

2.2. MEDIUM-TEMPERATURE OXIDATION

The region ahead of the combustion front is heated by conduction of heat, by convection of combustion gases, and by condensation of volatiles and steam generated from interstitial water. As the temperature rises, the crude oil undergoes three overlapping stages of pyrolysis: distillation, visbreaking, and coking (Abu-Khamsin, 1985). In distillation, light hydrocarbons

volatilize as their vapor pressures exceed their partial pressures in the gas phase. At higher temperatures (250-300°C), mild cracking of the oil occurs (visbreaking) in which the hydrocarbons lose small side groups and hydrogen atoms to form more stable, less branched compounds. At temperatures above 300°C, the residual oil cracks into a volatile fraction and a nonvolatile heavy residue consisting of coke, tar, and pitch which constitutes the primary fuel for combustion. Both cracking reactions produce hydrogen gas and some light hydrocarbons in the gas phase. In an oxygenated environment, a portion of these hydrocarbons is oxidized; hence, medium temperature oxidation occurs (Bardon and Gadelle, 1977; Fassihi, 1981).

2.3. HIGH-TEMPERATURE OXIDATION

In the combustion zone, heterogeneous reactions take place between oxygen in the gas phase and the heavy residue of oil that had been deposited on the rock matrix at lower temperatures. These reactions are characterized by the fact that practically all of the oxygen is combined in carbon oxides, thus giving the following overall stoichiometric equation:

$$CH_x + \left[1 - (1/2)m' + (1/4)x \right] O_2 \longrightarrow \left[1 - m' \right] CO_2 + m'\, CO + (1/2)\, x\, H_2O \qquad (2.1)$$

where x is the atomic hydrogen to carbon ratio of the fuel and m' is the molar ratio of carbon monoxide to total carbon oxides in the effluent gases.

$$m' = \frac{CO}{CO + CO_2} \qquad (2.2)$$

All of the oxygen not associated with the formation of CO or CO_2 is assumed to react with the hydrogen of the fuel to form water. The heat generated from these reactions provides the thermal energy which drives the process.

2.4. REACTION KINETICS

The oxidation of multicomponent hydrocarbon mixtures is complex, involving numerous homogeneous and heterogeneous reactions and their by-products, as described previously. The reactions encountered rarely correspond to elementary mechanisms. As a result, these reactions cannot be evaluated in a completely rigorous manner. Instead, the analysis of reaction rates is limited to an overall evaluation of the phenomena, in which the grouping of reactions becomes necessary (ie. low-temperature oxidation, coke combustion, etc.). The "reactant" is the crude oil or its residue, whatever its composition, and the resultant kinetic parameters are only accurate over limited temperature ranges.

The oxidation and combustion reaction rates of crude oil in porous media have been determined experimentally in the laboratory using the following three methods: (1) direct kinetic measurements at a given temperature (Weijdema, 1968; Dabbous and Fulton, 1974; Fassihi, 1981), (2) kinetic analysis of oxidation runs at variable temperatures (Weijdema, 1968; Burger and Sahuquet, 1972; Fassihi, 1981) and, (3) interpretation of numerical simulations of reverse combustion experiments (Burger and Sahuquet, 1972). Reaction rates have been expressed in terms of oxygen reacted rather than carbon oxides produced since LTO reactions consume more oxygen than can be accounted for in the effluent gases (Weijdema, 1968; Fasshi, 1981). Reaction rates, R_r , are generally given as functions of oxygen partial pressure and fuel concentration:

$$R_r = k\, P_{O_2}^m\, C_f^n \qquad (2.3)$$

where:

P_{O_2} = Partial pressure of oxygen

C_f = Instantaneous concentration of fuel

m,n = Reaction orders

and the reaction constant, k, is an exponential function of the absolute temperature according to Arrhenius' Law:

$$k = A_r \, exp(-E/RT) \tag{2.4}$$

where:

A_r = Arrhenius constant

E = Activation energy

R = Universal gas constant

T = absolute temperature

The reaction rate is often assumed to be first order with respect to fuel concentration, i.e., $n = 1$ (Weijdema, 1968; Fassihi, 1981). In heterogenous reactions, the constant, A_r , has been found to be a function of the grain size distribution of the porous medium (Smith, 1970; Burger and Sahuquet, 1971; Dabbous and Fulton, 1974; Bardon and Gadelle, 1977).

2.5. EFFECT OF METALLIC ADDITIVES

A catalyst is a substance which increases the rate at which a chemical system attains equilibrium by lowering the activation energy of the rate determining steps. Metals have long been recognized in the chemical industry for their catalytic potential in both hydrocarbon oxidation and cracking reactions. Metals catalyze by virtue of their ability to absorb the reactant molecules into a form in which they can more readily undergo reaction. The catalytic effect of metals on hydrocarbon oxidation reactions has been noted in many investigations, as discussed below.

Liquid phase, low-temperature oxidation occurs as the result of a chain reaction mechanism proceeding by a succession of elementary steps involving the formation of radical species containing free valences. These unstable, highly reactive molecular fragments propagate the chain reaction through their tendency to resaturate their chemical bonds. The chain reaction is categorized into three types of steps:

1. Initiation steps, in which the free radical species are formed. These steps might involve a simple collision where molecules aquire energy and then fall apart in a subsequent unimolecular step. Alternatively, initiation of the chain reaction might be induced by the absorption of a photon.

$$R\text{–}R + \text{Initiator} \longrightarrow 2R\cdot \tag{2.5}$$

where:

R– = alkyl chain

$R\cdot$ = alkyl radical

2. Propagation steps, in which radical species react with other molecules to form new radicals.

$$R\cdot + O_2 \longrightarrow RO_2\cdot \quad (2.6)$$

$$RO_2\cdot + RH \longrightarrow ROOH + R\cdot \quad (2.7)$$

3. Termination steps, where radicals recombine to form stable molecules.

$$R\cdot + R\cdot \longrightarrow R\text{–}R \quad (2.8)$$

Certain metallic derivatives can have a catalytic effect on this chain reaction mechanism (Van Tiggelen, 1968; Raćz, 1984). These derivatives can accelerate oxidation by participating directly in the chain reaction through the promotion of decomposition of peroxides:

$$Me^{2+} + ROOH \longrightarrow Me^{3+} + RO\cdot + OH^- \quad (2.9)$$

$$Me^{3+} + ROOH \longrightarrow Me^{2+} + RO_2\cdot + H^+ \quad (2.10)$$

where:

Me^{2+}, Me^{3+} = metal cations

In addition, metals also accelerate oxidation indirectly by destroying the antioxidants which are naturally present in most crude oils. Gureyev and Sablina (1965) showed that copper and brass consumed all of the wood resin antioxidant present in a benzene fuel within a six hour period. Other metals (iron, aluminum, zinc, tin, and lead) reduced the antioxidant concentration by 15-40 percent within a nine hour period. Gureyev and Sablina (1965) also showed that different fuels have different sensitivities to the catalytic activity of the metals, depending on the chemical composition of the fuels. Specifically, high molecular weight fuels were found to be more subject to the action of the metals than were fuels of lower molecular weight.

In studies undertaken to develop information on the effect of metal contamination on hydrocarbon cracking catalysts, it was reported that coke formation is promoted by the presence of various metals (Conner *et. al.*, 1957; Donaldson *et. al.*, 1961). The catalytic effect of these metals was found to be ordered as follows: $Cu < V < Cr = Zn < Ni$, with nickel about four to five times as active as vanadium.

Burger and Sahuquet (1972) compared the effluent gas compositions of kinetic experiments on a 27°API oil in a clean sand with those conducted with: (1) 1 percent nickel oxide added to the sand and, (2) a copper derivative (2000 ppm Cu) added to the oil. Two main observations were apparent. In the presence of additives: (1) the oxidation reactions were observed at lower temperature and, (2) the area under the high temperature peak increased. The first observation was explained by an increase in the oxidation rate when the catayst was present (lower activation energy). The second observation resulted from an increase in the fuel available for combustion and hence, an increase in the air requirement.

Similarly, Fassihi (1981) compared the effluent gas data from oxidation experiments using a 27°API French oil (Bardon and Gadelle, 1977) in a clean sand with data measured after addition of 2000 ppm copper. Analysis showed about a 50 percent decrease in the activation energy of the high temperature combustion reaction and a 50 percent increase in the activation energy of the medium temperature reaction. No significant change was detected in the activation energy of the low temperature reaction, but a higher Arrhenius constant, A_r, was observed.

Raćz *et. al.* performed kinetic experiments, using differential thermal analysis, on a 39°API Hungarian oil in the presence of metallic additives. In addition, the heat effects induced by these additives were determined from microcalorimetric measurements. They found that the rate of oxidation increased significantly in the temperature range of 140-200°C (depending on the pressure) in the presence of iron pentacarbonyl. The presence of iron pentacarbonyl resulted in greater heat generation at a lower temperature compared to experiments with the same oil without catalyst. The greatest increase in heat generation was in systems containing iron. A mixture containing manganese, vanadium, and a combination of other metals had a similar effect, but to a lesser degree.

Drici and Vossoughi (1985) studied the combustion of a 19.8°API crude oil in the presence of titanium, chromium, nickel, ferric, cupric, and vanadium oxides. Differential scanning calorimetry and thermogravimetric analysis were used to compare the combustion characteristics of the crude in the presence and absence of the metal oxides in the form of fine powders. As the solid content (metal oxides) of the mixtures was increased, two major observations were apparent: (1) the fractional amount of heat released in the lower temperature region gradually increased and attained a maximum level; (2) the coke combustion peak shifted to a lower temperature and became smaller. In contrast, experiments conducted on mixtures of coarse sand (mesh size less than 48), crude oil (5 percent by weight), and metal oxide (1 percent by weight) showed an increase in heat released during high temperature combustion of coke. This behavior was attributed to an increase in coke deposition. And finally, the effect of a small amount of metal oxides (1 percent by weight) in the presence of a fine silica powder (90 percent by weight) was found to be insignificant. They concluded that in the presence of a large surface area, the surface reactions are predominant and are unaffected by the addition of a small amount of metal oxide.

3. STATEMENT OF PURPOSE

In-situ combustion is a process whose applicabilty is largely determined by the combustion characteristics of the specific crude oil in question. These characteristics are directly influenced by the rate of oxidation and pyrolysis reactions occurring in the rock matrix ahead of the combustion front. A method is therefore sought by which these characteristics may be altered within a reservoir, thus making the process feasible for a wider variety of crude oils.

A review of past kinetic studies on the oxidation and pyrolysis reactions involved in in-situ combustion reveals the following generalities:

1. That certain metallic compounds increase the rates of these reactions and hence the extent and rate of fuel deposition and combustion.
2. That the sensitivity of different crude oils to the catalytic activity of these metals is dependent on the composition of the oil.
3. That the composition and surface area of the porous media are also important factors affecting the rates of these reactions.

In addition, the presence of metal catalysts is thought to have contributed to the formation of considerable quantities of fuel in several field operations (Earlougher *et. al.*, 1970; Hardy *et. al.*, 1972; Raćz, 1984).

Still, certain deficiencies are apparent in the published literature with regard to the use of catalyzing agents as a means of artificially regulating the combustion characteristics of crude oil within a reservoir. None of the existing literature addresses the feasibility of using water soluble metallic compounds as catalyzing agents. In addition, there is a need for a more thorough understanding of the mechanisms involved in the catalysis of crude oil oxidation through better quantitative assessment of kinetic parameters. Also, while certain metallic compounds have been identified that increase fuel deposition at low temperatures, none have been reported to induce the opposite effect.

As a result, this study was performed to investigate these deficiencies by examining the effect of several water soluble metallic compounds on the kinetics of crude oil oxidation reactions.

4. EXPERIMENTAL APPARATUS AND PROCEDURE

In this section, a description will be presented of the experimental apparatus and the procedure used to study the oxidation reaction kinetics of crude oil in porous media..

4.1. APPARATUS

Figure 4.1 shows a schematic of the apparatus used to study the reaction kinetics of oil oxidation reactions in porous media. Table 4.1 is a legend for Figure 4.1. The arrangement is essentially the same as the one built by Fassihi (1981) and modified by Abu-Khamsin (1985). The main components include a combustion cell located inside a furnace, three continuous gas analyzers, and equipment for the measurement and control of system temperature, pressure and flow rate. Table 4.2 lists the component specifications.

TABLE 4.1
LEGEND FOR FIGURE 4.1

1. Pressure Gauge	9. Pressure Regulator
2. Drierite Bed	10. Needle Valve
3. 3-Way Valve	11. 4-Way Valve
4. 60-μ Filter	12. 2-μ Filter
5. Mass Flow Controller	13. Rotameter
6. Furnace	14. Recorder
7. Temperature Controller	15. Mass Flow Meter
8. Digital Temperature Display	16. 5-Way Valve

TABLE 4.2
APPARATUS COMPONENT SPECIFICATIONS

Flow Controller	"Matheson" electronic mass flow controller, Model 8240, range 100-5000 sccm, with digital output
Gas Analyzers	"Beckman" Model 755, paramagnetic oxygen analyzer with 0-5, 0-10, 0-25, 0-50 % range and a suppressed range of 11-25, 16-21, 19-21, 20-21 %
	"Beckman" Model 864, nondispersive infrared carbon monoxide analyzer with linearizing circuit, 0-2 & 0-5 % range
	"Beckman" Model 864, nondispersive infrared carbon dioxide analyzer with linearizing circuit, 0-5 & 0-20 % range
Pressure Regulator	"Tescom" Model 26-1727-24-014, range 0-500 psi
Flow Meters	"Matheson" Model 8160, electronic mass flow indicator, range 100-2000 sccm, with digital output
	"Matheson" 0.1-2.0 scfh Rotameter

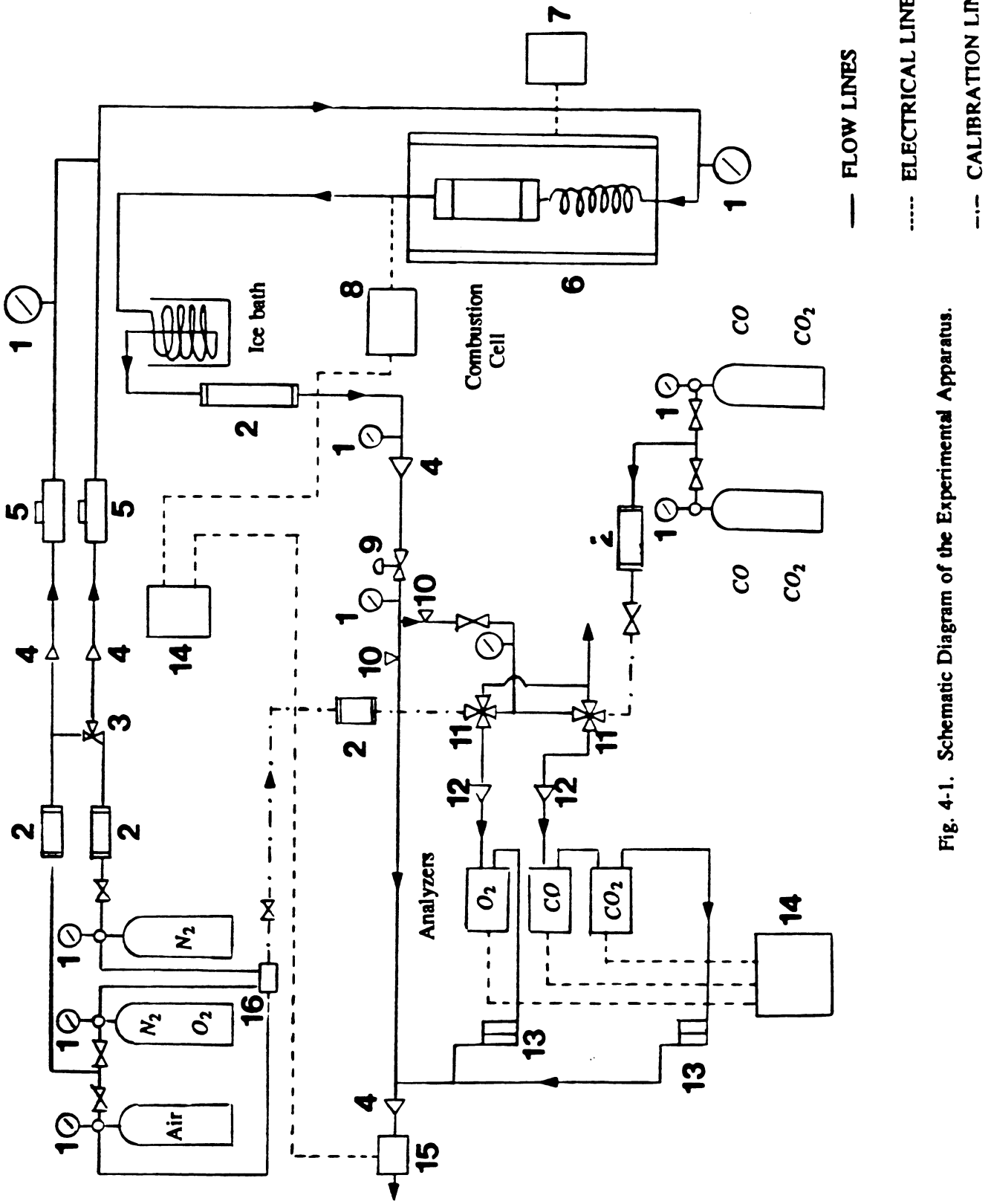

Fig. 4-1. Schematic Diagram of the Experimental Apparatus.

4.1.1. Combustion Cell

The combustion cell (Fig. 4.2) was constructed from a 4-1/4" long, 1-7/8" O.D. thick-wall stainless steel pipe which is closed on both ends by plugs held in place by screwed-on caps. A 0.065" O.D. tube was soldered into the upper plug to serve as a thermowell. A high-temperature, pressure seal was maintained by two brass "O" rings located between the end plugs and the pipe.

Two thin-wall stainless steel cups are housed inside the combustion cell, both with perforated bottoms. The lower cup, which is 1-1/16" long, was filled with dry sand; thus it acted as a preheater and flow distributer for the upper sample cup. The 2" long sample cup rests on the lower cup. A 1/8" O.D. tube was soldered into the bottom of the sample cup along the axis to act as a guide for the thermowell. Screens of 200 mesh were placed on the bottoms of the cups for added support.

Gas enters the bottom of the cell through a coil of 1/8" O.D. tubing , which serves as an additional preheater, and the gas exits at the top through a 1/4" O.D. tube. Complete specifications for the combustion cell are given in Table 4.3.

TABLE 4.3
COMBUSTION CELL SPECIFICATION

Combustion Cell		
	Body	Type 321 stainless steel, 4-1/4" length, 1-7/8" O.D., 1-3/16" I.D. (top), 1-1/8" I.D. (bottom)
	Caps	Type 321 stainless steel, 2-1/4" O.D., 1-1/16" length
	End Plugs	Type 321 stainless steal, 1-5/8" diameter
	Sample Cup	Type 321 stainless steel, 1-3/16" O.D., 1-1/16" I.D., 2" length
	Sand Cup	Type 321 stainless steel, 1-1/8" O.D., 1" I.D., 1-1/16" length
Thermowell		Type 321 stainless steel needle tube, 0.065"' O.D., 0.009" wall
Thermocouple		Type J iron-constantin, 0.04" O.D., 50" length
Preheater Coil		Type 347 stainless steel tube, 1/8" O.D., 0.01" wall, 148" length
Screens		200 mesh stainless steel
Gaskets		Brass "O" rings, 1-11/32" O.D., 1/16" wall, 1/8" height
Furnace		"Marshal" furnace model 1046, 3" bore, 10" diameter
Temperature Controller		"TECO" Model TP-2000, proportional 10 amp. triac output, range 0–1400 ^{o}F, type K thermocouple
Temperature Indicator		"Omega" Model 2176A, digital thermometer

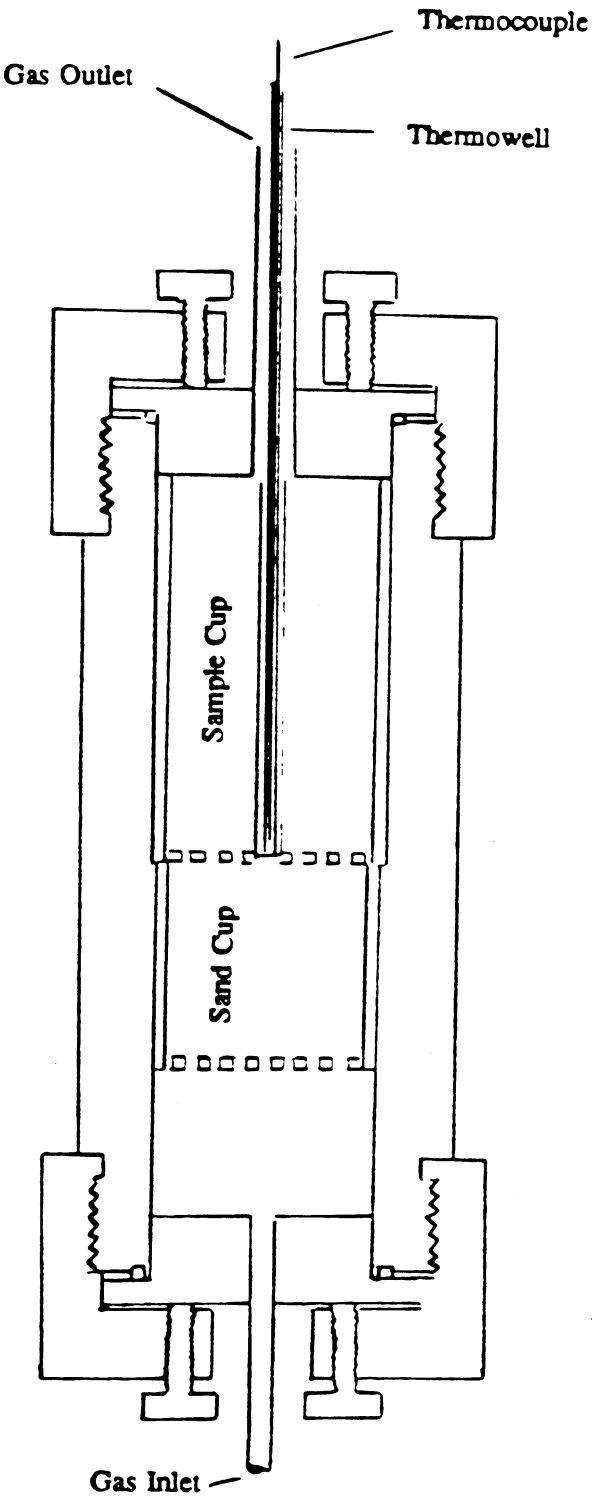

Fig. 4-2. Combustion Cell.

The combustion cell was placed in the center of a furnace which was controlled by a log/linear temperature controller. The controller may be programmed for different heating rates. Longitudinal and axial temperature gradients across the sample cup were previously found to be negligible (Fassihi, 1981; Abu-Khamsin, 1985).

4.1.2. Flow Control and Pressure Regulation

Feed gas from high pressure cylinders passes through two-stage pressure regulators into Dreirite beds for filtration and drying. Flow rates into the combustion cell were regulated by an electronic mass flow controller. Effluent gases from the combustion cell were cooled in a condenser made from a coil of 1/8" O.D. tubing situated in an ice bath. Liquid condensate was collected in a trap at the bottom of the condenser coil. The volume of the trap was increased in later experiments in order to deal with larger condensate volumes resulting from the addition of water to the oil/sand samples being tested. Another Dreirite bed was placed after the trap to further dry the gas before passage into a 0-500 psi, adjustable back-pressure regulator, used to control system pressure.

A constant portion of the gas stream was then diverted into the gas analyzers and later recombined with the remainder of the effluent before final measurement through an electronic mass flow meter. Flow rate through the analyzers was controlled with needle valves and measured through Rotameters.

4.1.3. Gas Analysis

A portion of the effluent gas stream was continuously measured for concentrations of CO, CO_2, and O_2 by three on-line gas analyzers. The analyzers were calibrated with appropriate high and low scale standard gas mixtures at conditions of pressure and flow rate equivalent to those encountered during the experiment. The sensitivity of the O_2 analyzer to changes in ambient air temperature and pressure required that it be calibrated at least every two hours during an experiment. Consequently, a system of two four-way valves was used to control flow through the calibration lines in order to minimize disturbances in the system when switching the analyzers between on-line and calibration modes.

4.1.4. Data Collection

Readings from the combustion cell temperature indicator, the mass flow meter, and the three gas analyzers were scanned by an Esterline-Angus data logger and recorded by a Compaq microcomputer at three minute intervals. Those readings were also recorded on strip charts for back-up and monitoring purposes. Data were then processed, analyzed, and printed by a Vax 11/750 computer.

4.2. EXPERIMENTAL PROCEDURE

In this section, properties of the crude oil and sand used in the experiments are discussed as well as the experimental procedure and design.

4.2.1. Test Materials

A 18.5° API crude oil from the Huntington Beach field was used in these experiments. Table 4.4 lists some of the oil's basic properties as well as an elemental analysis.

TABLE 4.4
CRUDE OIL PROPERTIES

Field	Zone	Gravity (°API)	%C	%H	Atomic H/C Ratio	%N	MW
Huntington Beach	Lower Main Zone	18.5	84.50	11.53	1.64	0.86	386

A large surface area can have a substantial effect on the kinetics of oil oxidation reactions. The total specific area available for reactions can increase considerably with the addition of even small amounts of clay. Consequently, in order to isolate the effects of the metals being tested, all runs were made using clean, unconsolidated, 20-30 mesh Ottawa sand. Table 4.5 shows a sieve analysis of the sand.

TABLE 4.5
SIEVE ANALYSIS OF SAND

Sieve Size	Percent by Weight Retained
20	0.40
24	41.40
28	57.70
32	0.43
60	0.05
>60	0.02
	100.00

4.2.2. Operating Procedure

Experiments were made with mixtures of oil, sand, and water in proportions that yielded approximate values of desired saturations. Test samples were prepared by adding 2 ml of a solution containing a dissolved metallic compound in water to approximately 40 g of a premixed oil/sand mixture; thus giving a water saturation of about twenty percent. An oil saturation of fifteen percent was chosen to minimize oxygen consumption (and hence heat generation) in order to allow for control of the linear temperature rise needed to analyze the data. A heating schedule of 50 °C/hr was selected to minimize radial temperature gradients across the sample while creating an experiment of reasonable duration (Fassihi, 1981).

After tamping the mixture into the sample cup, the combustion cell was pressure tested with nitrogen and placed inside the furnace. The system was brought to the desired pressure by flowing air and adjusting the back-pressure regulator. The combustion cell was then subjected to a linear temperature rise until the amount of produced carbon oxides became insignificant. After the system was cooled, the content of the sample cup was weighed.

4.2.3. Experimental Design

A total of sixteen runs were completed using the experimental apparatus and procedure described above. The purpose of these experiments was to examine the effects of different water soluble metallic compounds on the oxidation of crude oil at various pressures. nsequently, all runs were made using the same crude oil (Huntington Beach), inlet flowrate (0.60 l/m), oxygen concentration (21%), and heating schedule (50°C/hr). In addition, all runs were made using the same oil/sand mixture, so that oil saturations could be assumed constant from run to run. Table 4.6 lists the operating conditions of each run as well as the cold water solubilities of the metallic compounds.

TABLE 4.6
OPERATING CONDITIONS

Run No.	Additive	Pressure (psig)	Molar Concentration of Additive (mole %)	Cold Water Solubility of Additive (g/100 cc)
201	None	80		
202	None	43		
207	None	40		
203	$CuSO_4 \cdot 5H_2O$	40	1.01	32
205	$CuSO_4 \cdot 5H_2O$	81	1.01	32
209	$FeCl_2 \cdot 4H_2O$	79	1.99	160.1
211	$FeCl_2 \cdot 4H_2O$	43	1.99	160.1
216	$SnCl_2 \cdot 2H_2O$	82	2.02	83.9
223	$SnCl_2 \cdot 2H_2O$	39	2.02	83.9
213	$ZnCl_2$	83	1.90	432
214	$MgCl_2 \cdot 6H_2O$	83	1.98	167
215	$K_2Cr_2O_7$	80	2.02	4.9
217	$AlCl_3 \cdot 6H_2O$	82	2.00	69.9
218	$MnCl_2 \cdot 4H_2O$	80	2.00	151
222	$Ni(NO_3)_2 \cdot 6H_2O$	40	2.00	238
225	$3CdSO_4 \cdot 8H_2O$	40	2.00	113

5. DATA ANALYSIS

The total oxygen consumption resulting from nonisothermal kinetic experiments is a summation of the oxygen consumed by the three competing oxidation reactions. As a consequence, the identificaton of kinetic parameters for each of the reactions can only be accomplished after the total oxygen consumption curve has been decoupled into its three constituent parts. The following section outlines the mathematical model, as described by Fassihi (1981), and data analysis procedure used to interpret the kinetic data.

5.1. MODELING OF REACTIONS

The rate of reaction (Eq. 2.3) may be equated to the rate of oxygen consumption ($q\Delta\gamma$) per unit bulk volume:

$$R_r = \frac{q\Delta\gamma}{AL} = A_r P_{O_2}^n C_f \exp(-E/RT) \tag{5.1}$$

where:

- q = volumetric gas flow rate
- A = cross-sectional area
- L = length of pack
- $\Delta\gamma$ = change in molar oxygen concentration

This expression is also equivalent to the rate of decrease in fuel concentration:

$$R_r = \alpha \frac{dC_f}{dt} \tag{5.2}$$

where α is a proportionality factor equal to the amount of oxygen in moles that reacts with one gram of fuel. Integration of Eq. 5.2 yields:

$$\alpha C_f(t) = \int_t^\infty \frac{q\Delta\gamma}{AL} dt' \tag{5.3}$$

which may be combined with Eq. 5.1 to yield:

$$\frac{\Delta\gamma}{\int_t^\infty \Delta\gamma dt'} = \frac{A_r P_{O_2}^n}{\alpha} \exp(-E/RT) \tag{5.4}$$

The left hand side of Eq. 5.4 is referred to as the relative reaction rate of oxygen consumption and may be obtained directly from numerical integration of the oxygen consumption data.

From Eq. 5.4 it is apparent that, for single reactions, a semi-logarithmic graph of the relative reaction rate versus the inverse of absolute temperature will yield a straight line with a slope proportional to the activation energy of the reaction, E, and with an intercept:

$$intercept = \log [A_r P_{O_2}^n / \alpha] \tag{5.5}$$

Figure 5.1 shows such a graph for Run 201. At high temperatures, the data fall on a straight line as predicted by the model; but, at lower temperature (higher 1/T values) the data deviate from a straight line because of an overlap with medium temperature oxidation reactions. At very high temperatures, to the left of the graph, the data also deviate from a straight line, but this behavior is in the range where both terms in the relative reaction rate are small and hence the data would be expected to be inaccurate.

The high temperature reaction is assumed to occur at temperatures lower than the point of deviation according to a straight line extrapolation of the high temperature data. By subtracting this extrapolation (Curve I, Fig. 5.2a) from the original oxygen consumption curve, a new curve (Curve II, Fig. 5.2a) is obtained which describes oxygen consumption at lower temperatures. Similarly, Curve III may be obtained by subtraction. This curve describes the equivalent production of carbon oxides ($\delta = CO_2 + 1/2CO$) in the medium temperature range.

Calculation of the relative reaction rate from Curve II as a function of 1/T gives the Arrhenius graph labelled Curve II in Fig. 5.3a. This graph is not linear as it contains data from more than one reaction. Fassihi (1981) found, however, that if the production of carbon oxides, δ, was graphed rather than the disappearance of oxygen, the resulting data formed a straight line. Such a graph is shown in Fig. 5.3a, Curve III, where the carbon oxides rate function ($\delta / \int_t^\infty \delta dt'$) is graphed. This graph shows a definite straight line over a portion of the temperature range.

Fassihi (1981) recommended calculating the oxygen comsumption in the medium temperature range by assuming that the slopes (ie., activation energies) of the oxygen consumption and carbon oxides production curves (Fig. 5.3a, Curves II and III, respectively) are equivalent. However, the slopes of these curves are, by inspection, quite dissimilar and therefore, this assumption would be inappropriate.

Oxygen consumption may also be estimated from a stochiometric balance according to the combustion reaction (Eq. 2.1). A theoretical ratio of oxygen consumed to carbon oxides produced may then be determined from measured values of the atomic hydrogen to carbon ratio (x) and the carbon monoxide to carbon dioxide molar ratio (m'), as follows:

$$\frac{O_2}{\frac{1}{2}CO + CO_2} = \frac{1 - \frac{1}{2}m' + \frac{1}{4}x}{1 - \frac{1}{2}m'} \tag{5.6}$$

A comparison of this predicted ratio to the actual measured ratio of Curve II to Curve III (Table 5-1) shows that the values are similar at temperatures near the peak of Curve III (in the temperature range from 530 to 560 °K). It therefore appears reasonable to assume that the oxygen consumption at medium temperatures (Curve IV, Fig. 5.2b) may be calculated by applying a constant multiplying factor (determined at the peak of Curve III) to the carbon oxides production curve (Curve III, Fig. 5.2b).

Oxygen consumption in the low temperature reaction (Curve V, Fig. 5.2c) may then be determined by subtracting oxygen consumed at medium temperatures (Curve IV) from the remainder of the oxygen consumption curve (Curve II). When these data are evaluated using the integral $\Delta\gamma / \int_t^\infty \Delta\gamma dt'$, and the result is graphed as a function of 1/T (Fig. 5.3b), kinetic parameters for the low temperature oxidation reaction may be computed.

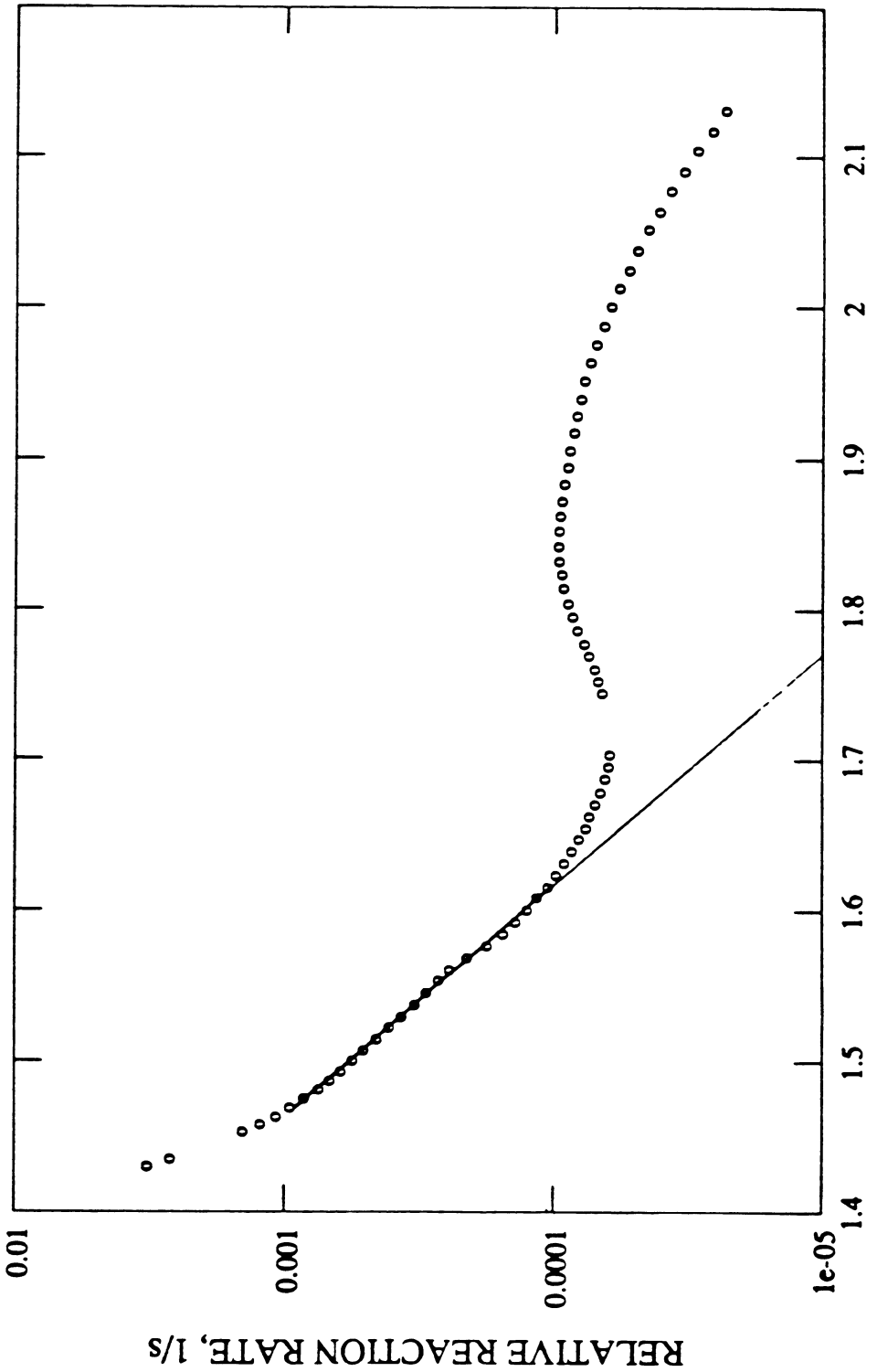

Fig. 5-1. Arrhenius Graph, Extrapolation of High Temperature Data, Run 201.

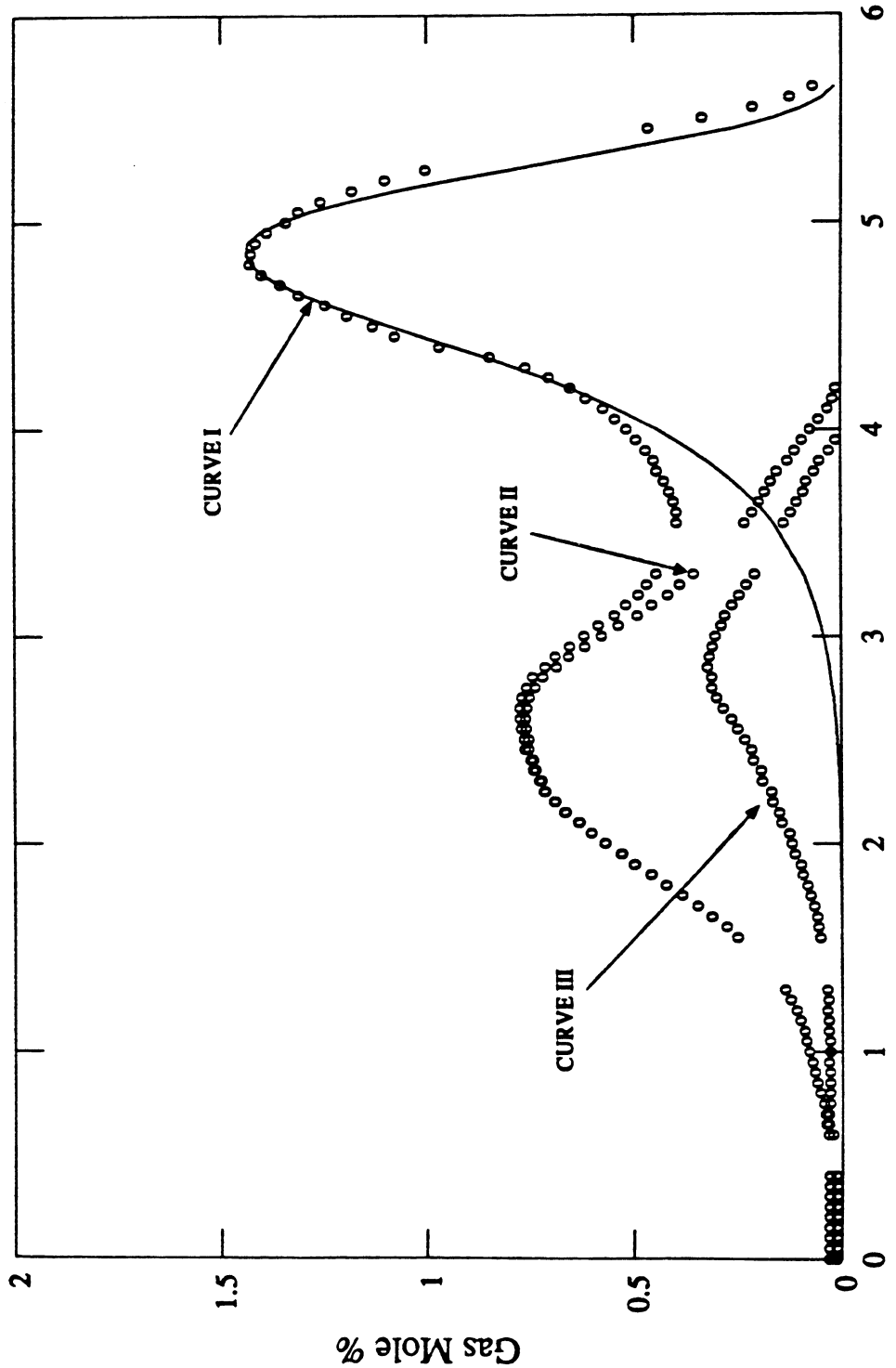

Fig. 5-2a. Decomposition of High Temperature Data, Run 201.

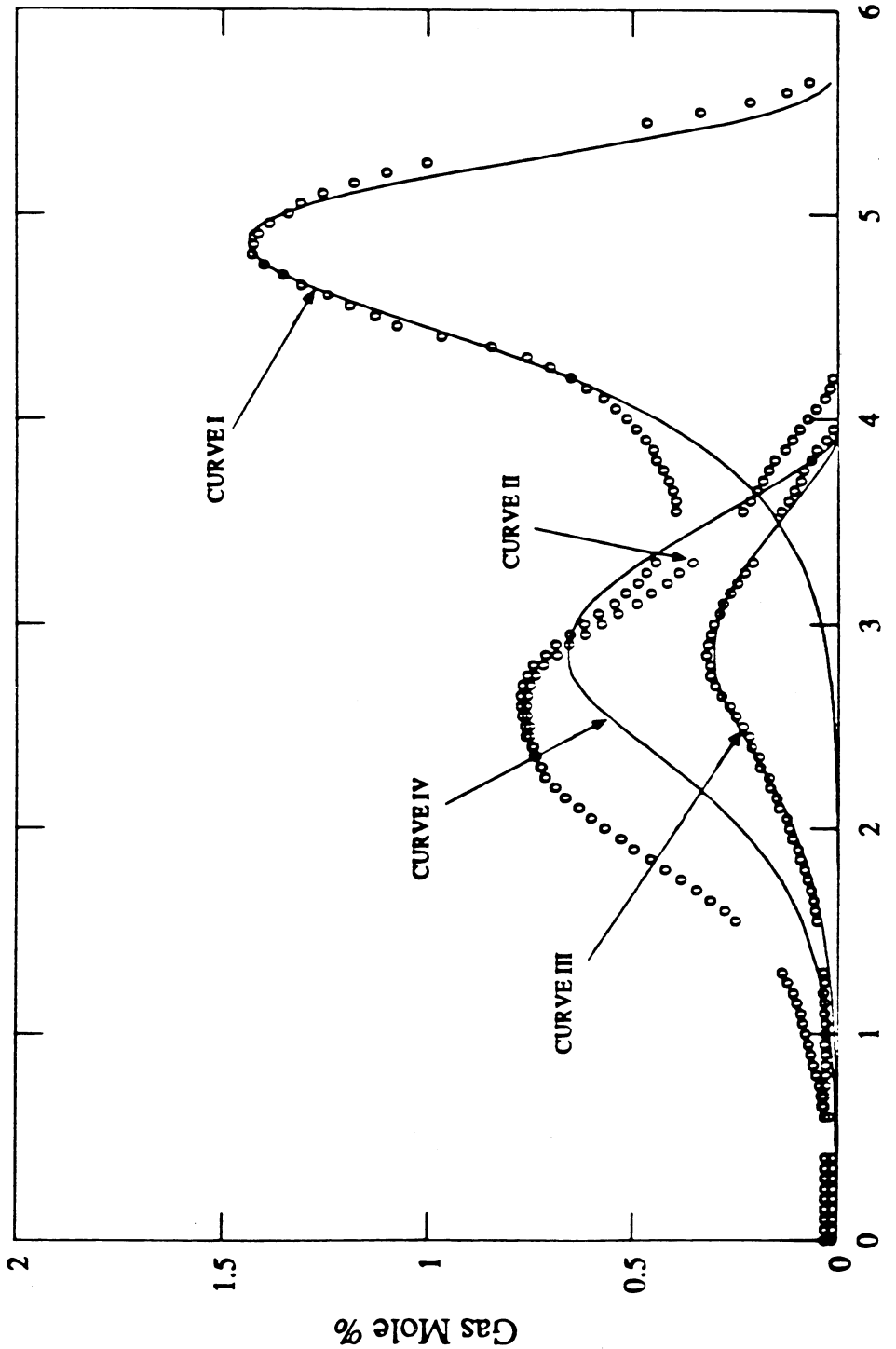

Fig. 5-2b. Decomposition of Medium Temperature Data, Run 201.

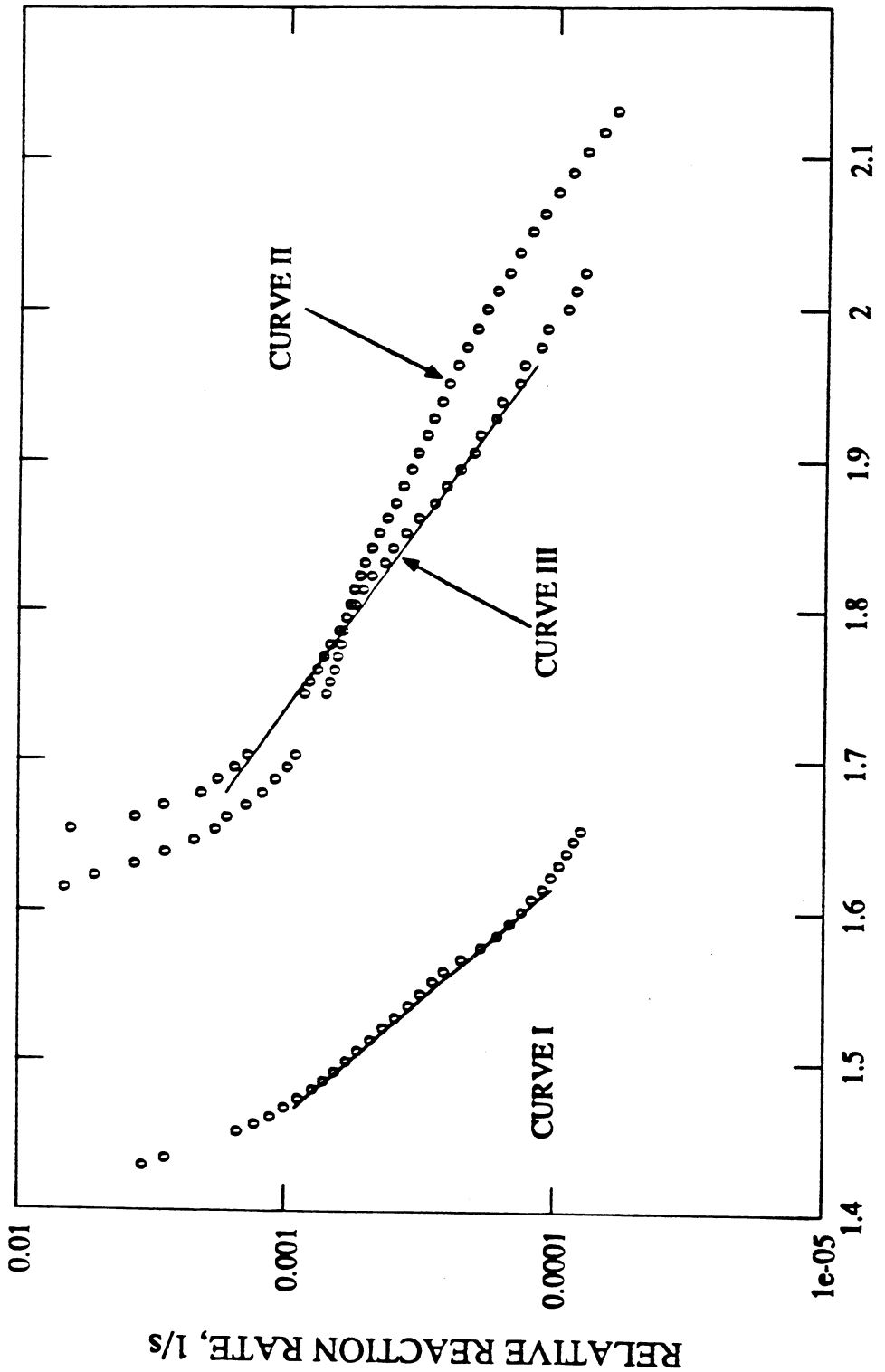

Fig. 5-3a. Arrhenius Graph, Medium Temperature Data, Run 201.

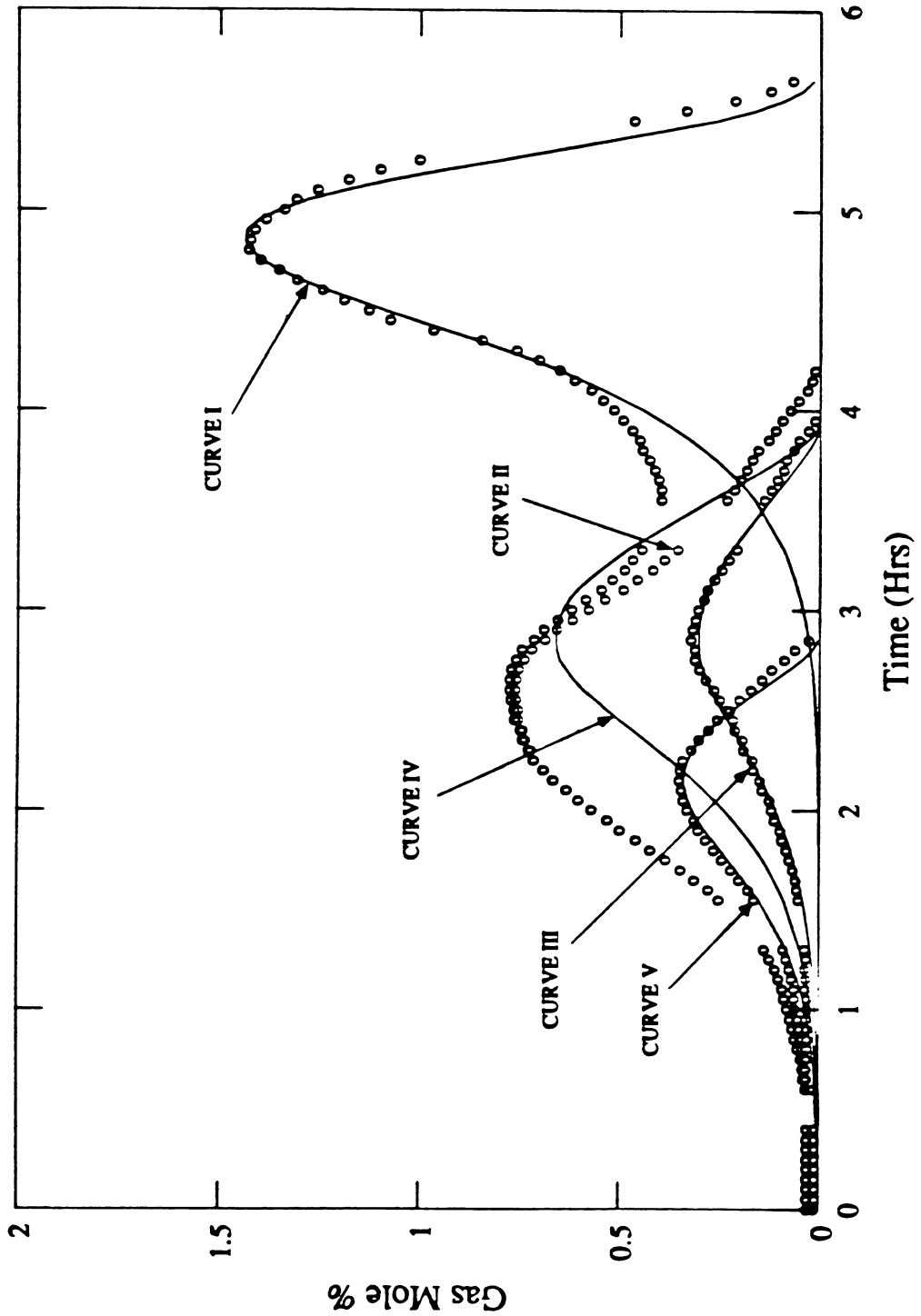

Fig. 5-2c. Decomposition of Low Temperature Data, Run 201.

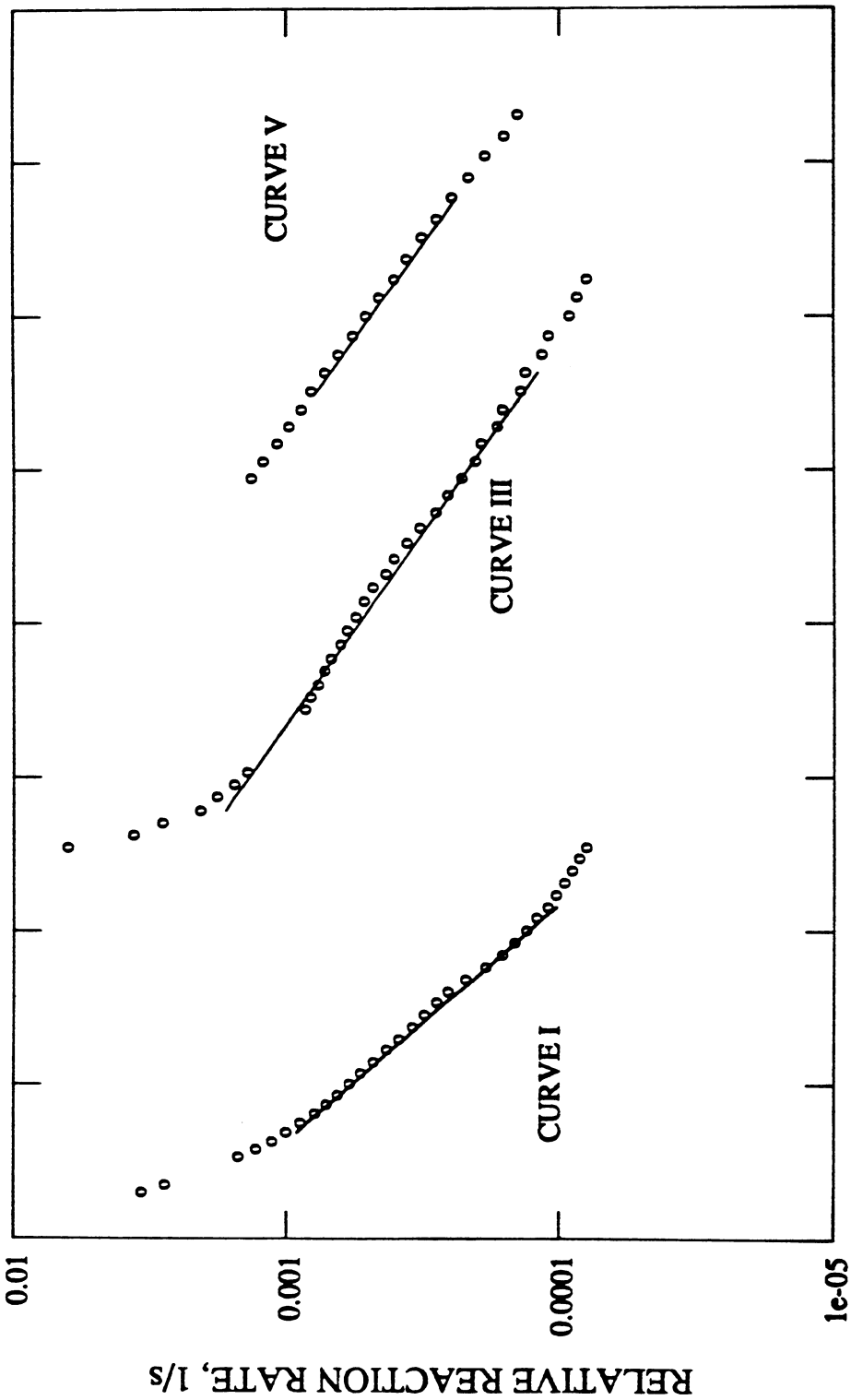

Fig. 5-3b. Arrhenius Graph, Low Temperature Data, Run 201.

TABLE 5.1
COMPARISON BETWEEN PREDICTED AND MEASURED RATIO
OF CURVE II/CURVE III

TIME (Hrs)	TEMPERATURE (K)	CURVE III Mole %	PREDICTED RATIO CURVE II/CURVEIII	MEASURED RATIO CURVE II/CURVE III
2.60	534	0.251	2.98	2.90
2.65	537	0.272	2.74	2.66
2.70	540	0.287	2.58	2.50
2.75	543	0.299	2.42	2.34
2.80	546	0.299	2.36	2.27
2.85	548	0.309	2.18	2.09
2.90	551	0.304	2.12	2.02
2.95	554	0.298	2.03	1.92
3.00	557	0.290	1.94	1.83
3.05	560	0.275	1.90	1.77

5.2. DATA MANIPULATION

The data anaysis technique described above is an interactive process, requiring subjective, visual determinations as to which data points constitute the best straight lines in the Arrhenius graphs; or more accurately, which temperature ranges best characterize each reaction. At each stage in the decomposition of the oxygen consumption data, errors may be introduced as a result of these subjective evaluations. Furthermore, analysis of the low temperature data is completely dependent on prior analysis of high temperature data, so these errors can propagate rapidly. As a consequence, this procedure often yields nonunique, poor matches of the overall oxygen consumption data, with inconsistent trends in the extracted kinetic parameters.

In order to improve the analysis, a standardization of the data selection procedure is required which would systematically identify the data which best represent the reactions. Logically, the analysis should include those data which are considered to be the most accurate. The relative reaction rate, R_{rr} , of oxygen consumption is defined by

$$\text{Relative Reaction Rate} = R_{rr} = \frac{\Delta\gamma_i}{\int_{t_i}^{\infty} \Delta\gamma dt'} \tag{5.7}$$

Examination of the factors contributing to the errors in this term reveals that the errors in $\Delta\gamma_i$ are likely to be equivalent from case to case (instrument error), whereas the errors in the integral term are likely to be dependent on the size of the integral itself. That is, when the integral is large (around the peak of the curve), the error in the relative rate is smaller and vice versa. Indeed, intuition would suggest that the analysis should include the peak consumption data since it is these peaks which best characterize the reactions.

A criterion for determining the accuracy of a curve fit is the standard deviation (or variance) between the measured data and those values predicted by the mathematical model,

$$\sigma^2 = \frac{\sum_{i=1}^{n} (y_i - y_{calc})^2}{n-p} \tag{5.8}$$

where:

y_i = measured data

y_{calc} = values predicted by model

n = number of data points considered

p = number of degrees of freedom used up in the characterization of the system

σ^2 = standard deviation

In this case, two degrees of freedom are used, corresponding to the two independent parameters of the model (E/R and $A_r P_{O_2}^m / \alpha$). A minimum standard deviation, however, would always occur with the least amount of data points. We would instead prefer that as many data as possible be used in the analysis. In order to achieve this end, the standard deviation was divided by a term representing the area under the portion of the oxygen consumption curve being considered

$$\sigma_{new}^2 = \frac{\sigma^2}{\int_{t_i}^{t_n} \Delta\gamma dt'} \tag{5.9}$$

where:

σ_{new}^2 = modified standard deviation

With the above considerations in mind, the following algorithm was used to curve fit each reaction peak:

1. For a given set of data, a linear least squares fit of the Arrhenius graph was used to determine the activation energy and pre-exponential constant ($A_r P_{O_2}^m / \alpha$). (See Appendix A for a derivation of the minimizing equations.)
2. The predicted oxygen consumption curve was generated using these parameters.
3. A standard deviation (Eq. 5.9) was determined between this curve and the actual oxygen consumption data.
4. The minimum standard deviation was determined for the sets of data centered around each data point within a four point range of the peak consumption value.
5. The curve fit corresponding to the minimum of these minima was selected as the best fit of the reaction peak.

An example of this curve fitting algorithm on the high temperature data from Run 201 is presented in Appendix B.

5.3. TEMPERATURE ADJUSTMENT

The rate of temperature rise in these experiments was programmed to increase linearly as a function of time. Small deviations from this linear rate did occur, however, due to the heat generated from the oxidation reactions and because of general measurement errors. These small deviations were found to have a considerable effect on the calculated oxygen consumption. Consequently, the temperature data were smoothed using a running average.

This running average was determined for each data point by obtaining a linear least squares fit of the adjacent four temperature versus time data points. The adjusted temperature was consequently that temperature obtained from solution of the resultant fitting equation.

6. RESULTS AND DISCUSSION

In this section, the results of the oxidation experiments will be presented and discussed. First, a qualitative description will be made of the effluent gas data for a typical oxidation run. Next will be presented the data matches resulting from the application of the curve fitting algorithm described in Section 5. Finally, the effects of pressure and the different metallic compounds on the oxidation reaction kinetics will be discussed.

6.1. QUALITATIVE OBSERVATIONS-EFFLUENT GAS DATA

Figure 6.1 shows the effluent gas composition versus time response for a typical non-isothermal oxidation run (Run 201). The plotted concentrations of carbon monoxide (asterisks) and carbon dioxide (x's) on the left ordinate are those measured directly by the analyzers. The measured oxygen consumption (open circles), however, had to be adjusted to account for variations in the effluent gas flow rate (Fassihi, 1981). These variations are caused by differences in the number of moles in the reacting and produced gases. The measured temperatures of the combustion cell (closed circles) are plotted against the right ordinate.

Figure 6.1 shows two apparent peaks in the oxygen consumption and carbon oxides production curves. These peaks represent the overlap of the three sequences of oxidation reactions described in Section 2. At low temperatures, oxygen is consumed with little production of carbon oxides. At higher temperatures, the oxygen consumption increases and carbon oxides production becomes significant. Each of these curves reaches a medium temperature maximum, but at different temperatures. The medium temperature peak for carbon oxides production represents the maximum reaction rate for the medium temperature reaction. The medium temperature oxygen peak, however, results from a summation of the oxygen consumption from the two competing lower temperature reactions. At temperatures above 600°K, the amount of oxygen consumption becomes proportional to the produced carbon oxides (i.e., $1/2CO + CO_2$) so the peaks occur along the same temperature axis. These data may therefore be entirely attributed to the high temperature combustion of the heavy coke-like residue deposited at lower temperatures.

Fluctuations from the programmed linear temperature rise are evident from Fig. 6.1, especially near the high temperature peak. These deviations are caused by the heat generated from the combustion of the crude oil.

6.2. REPEATABILITY OF EXPERIMENTS

Run 207 was conducted under conditions nearly identical to those in Run 202 in order to check the reproducibility of the experimental data. Figure 6.2 shows a comparison of the effluent gas data for the two runs in which no significant differences are observed. In this figure, oxygen data from Run 207 are plotted as open circles, carbon monoxide data as asterisks, and carbon dioxide data as open diamonds, while for Run 202, oxygen data are plotted as closed diamonds, carbon monoxide data as closed circles, and carbon dioxide data as closed triangles. Slight deviations in the data may be attributed to small differences in operating pressure, and the normal errors in flow rate control and compositional analysis.

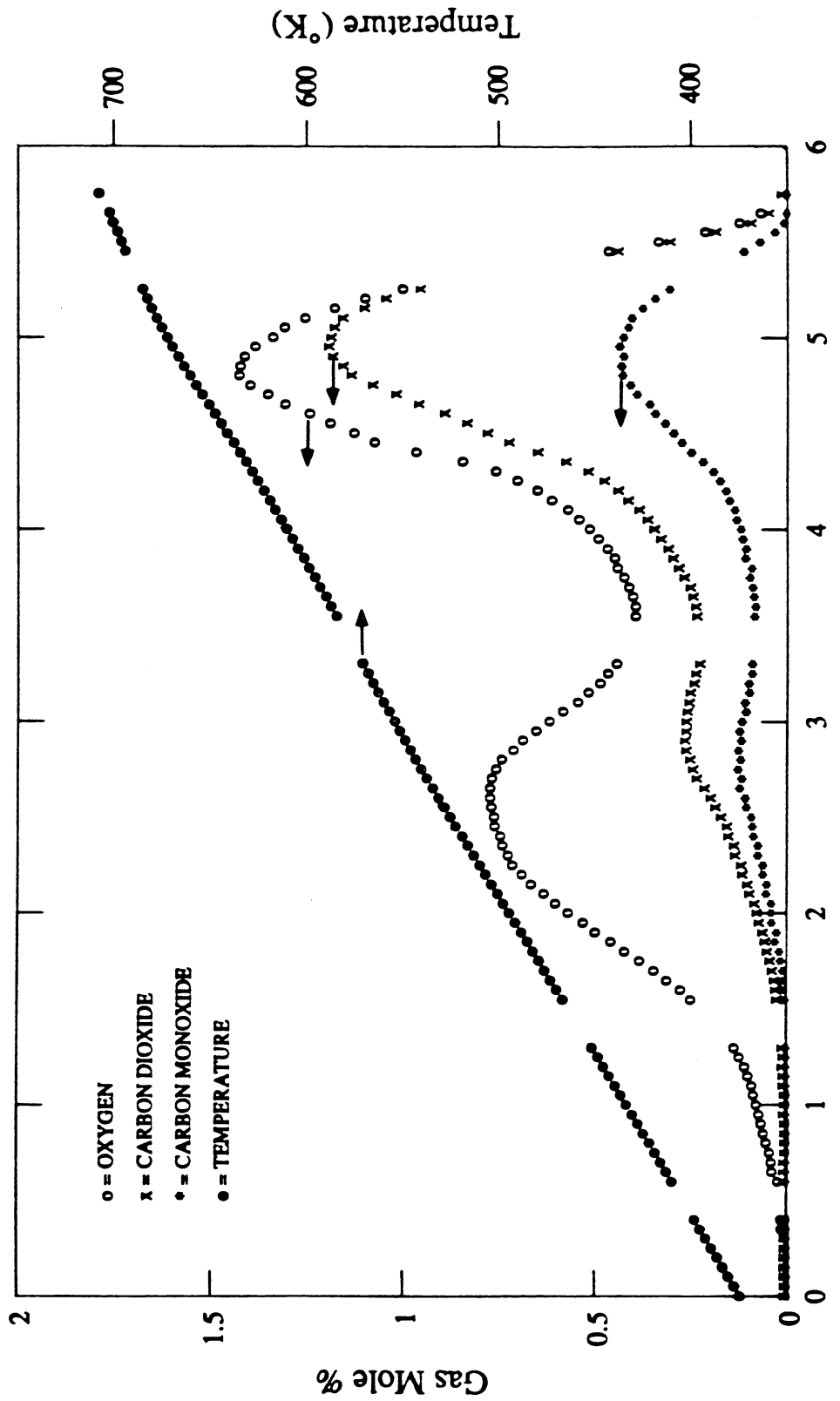

Fig. 6-1. Effluent Gas and Temperature Versus Time, Run 201.

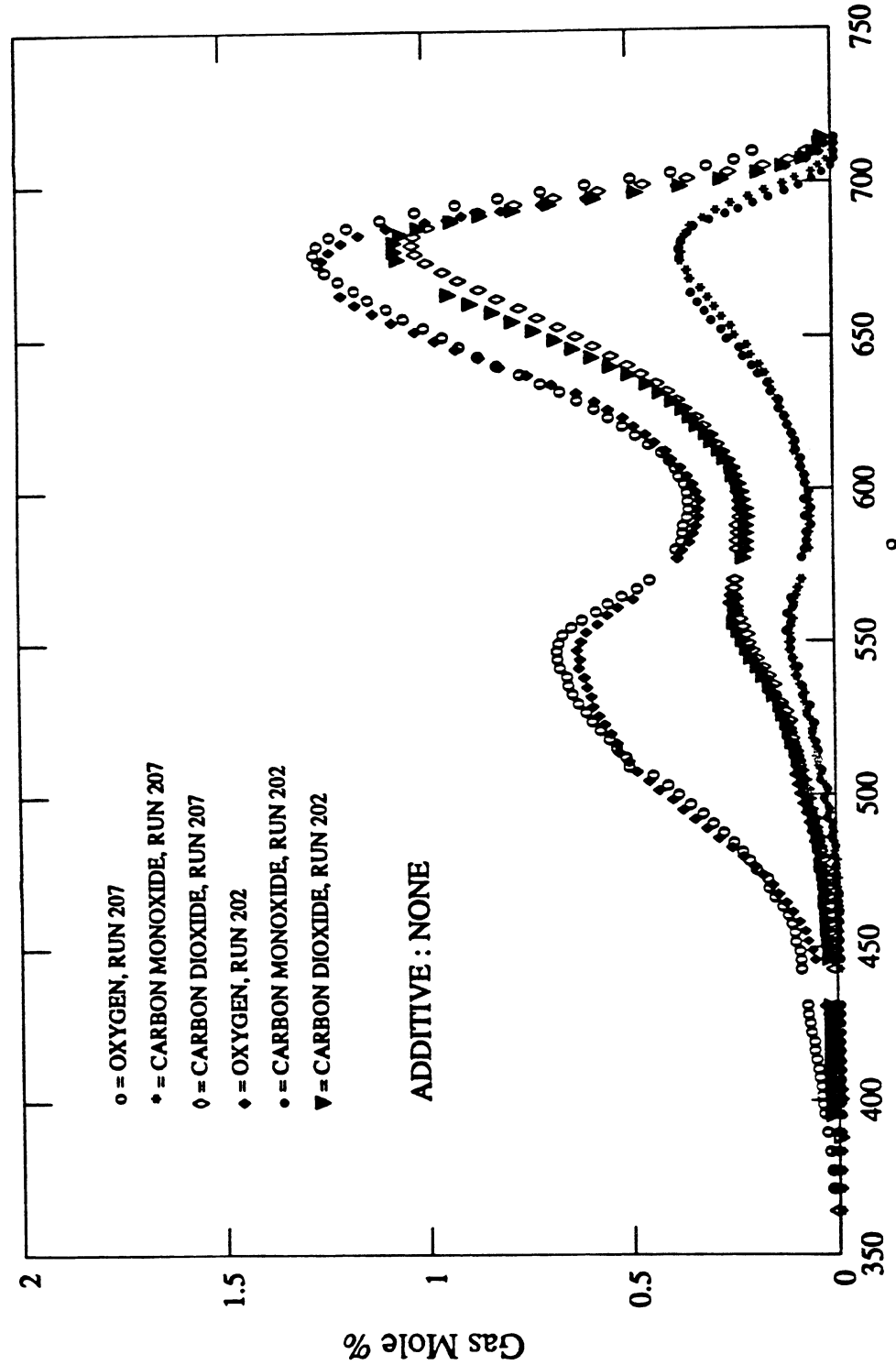

Fig. 6-2. Effluent Gas Data Comparison Between Run 202 (p = 43 psig) and Run 207 (p = 40 psig).

6.3. RESULTS OF EXPERIMENTAL CURVE FITS

Figures 6.3 through 6.18 show the data matches that result from the curve fitting algorithm outlined in Section 5. In each figure, the curve fits for each reaction peak are illustrated as well as the resultant curve fit of the total oxidation curve. In addition, the data point ranges used in each curve fit are highlighted as closed circles.

On the whole, the quality of the curve fits at the temperature range near the individual reaction peaks is good. The accuracy of overall matches of the oxygen consumption data, however, varies from run to run. The largest discrepancies in the data matches are seen in the low temperature peaks and in the valleys between the peaks. In particular, the discrepancies are noticeable in the valleys between the medium and high temperature reactions. This behavior may be attributed to several factors.

As described previously, the analysis of reaction rates in crude oil oxidation cannot be made rigorously because of the complexity and number of reactions taking place. The "reactions" referred to in this report are in fact groups of reactions. The accuracy of the model is therefore dependent on the uniformity of the reactant fuel composition over the temperature range in which the reaction occurs.

As a consequence, data matches are generally more accurate when one category of reaction predominates in the oxygen consumption data (i.e., high temperatures) or when the fuel composition is more uniform over the temperature range of the reaction (narrower reaction peaks). For example, the overall match of the high temperature data is considerably better in Run 211 (Fig. 6.9) than in Run 213 (Fig. 6.10). At lower temperatures, where more than one reaction occurs simultaneously, the data must first be decoupled according to the assumptions described in Section 5. Errors in the high temperature matches are subsequently transmitted into the low temperature data. Hence, the curve fits of these lower temperature data are inherently less accurate.

In general, in all the figures, the oxygen consumption valley between the medium and high temperature reactions is not well matched. The reason can be seen in any of the figures, but Figs. 6.19a and 6.19b (Figs. 5.2b and 5.3b in the previous section) show the problem in a qualitative manner. Curve III of Fig. 6.19a is the carbon oxides production curve, and Curve IV shows the resulting oxygen consumption curve. The upper limit of these curves is at a time slightly less than four hours. The actual oxygen consumption, which is what is left after subtracting Curve I, is shown as a series of circles whose upper limit is greater than four hours (Curve II). This general behavior may be seen in each of Figs. 6.3 to 6.18.

A number of curve fitting methods was tried in an attempt to force the oxygen and carbon oxides curves to terminate at equivalent times, but no method was satisfactory. As a result, none of the summed oxygen consumption curves in Figs. 6.3 to 6.18 matched the experimental data well in the oxygen consumption valley. A study of Fig. 6.19b shows why it is not possible to properly curve fit the data in this temperature range ($1/T \approx 1.70 \times 10^{-3}\ °K^{-1}$). Note that in Fig. 6.19b, the high temperature data clearly exhibit a straight line up to a $1/T$ value of about $1.60 \times 10^{-3}\ °K^{-1}$. The medium temperature data exhibit a straight line starting at a $1/T$ value of about $1.75 \times 10^{-3}\ °K^{-1}$. But in the temperature range between, which corresponds to the valley between the two reactions, none of the data fits either straight line. Thus there is a range of temperatures over which the kinetics model does not fit the data. This behavior was found to be true for all of the runs.

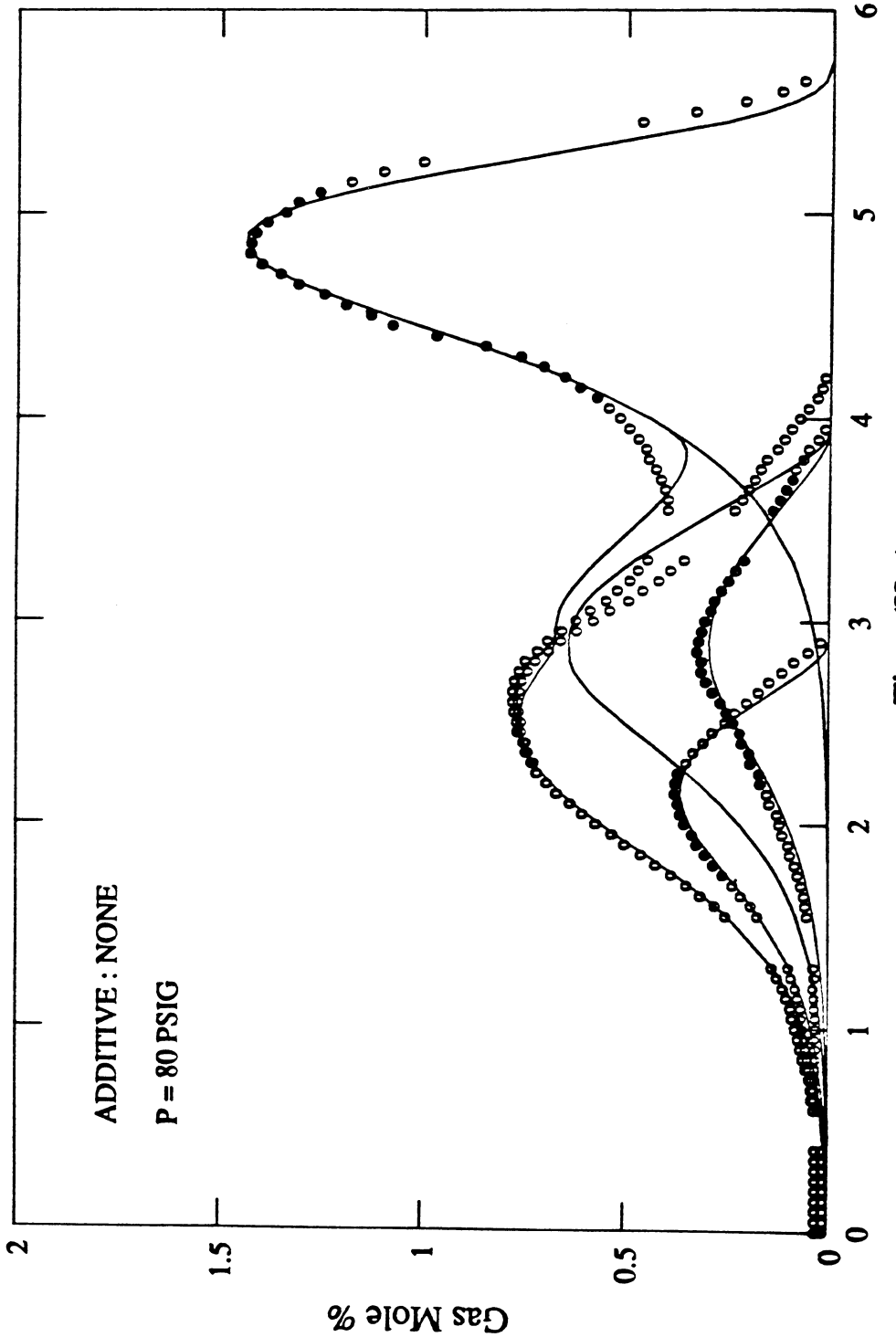

Fig. 6.3. Curve Fit, Run 201, No Additive (p = 80 psig).

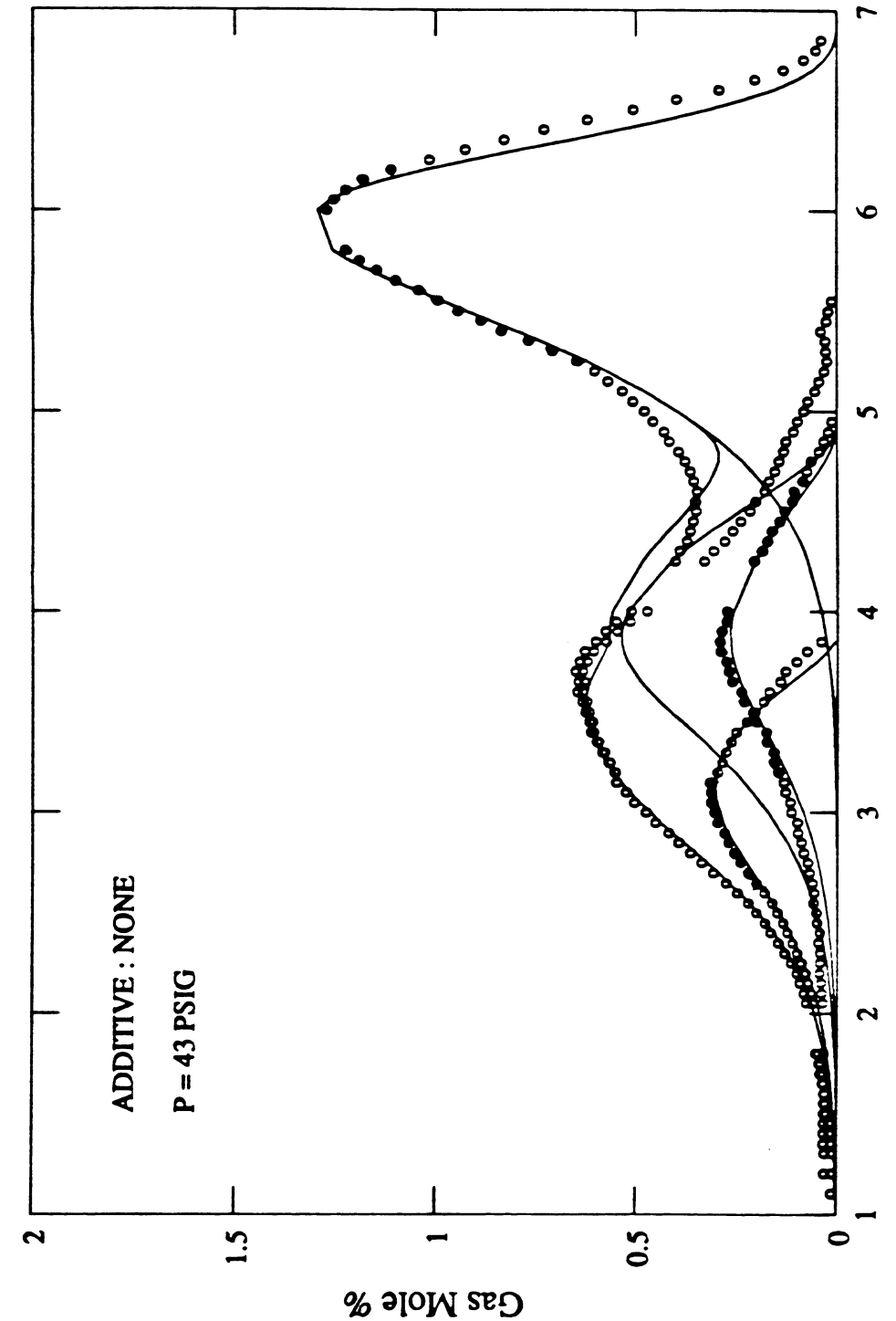

Fig. 6.4. Curve Fit, Run 202, No Additive (p = 43 psig).

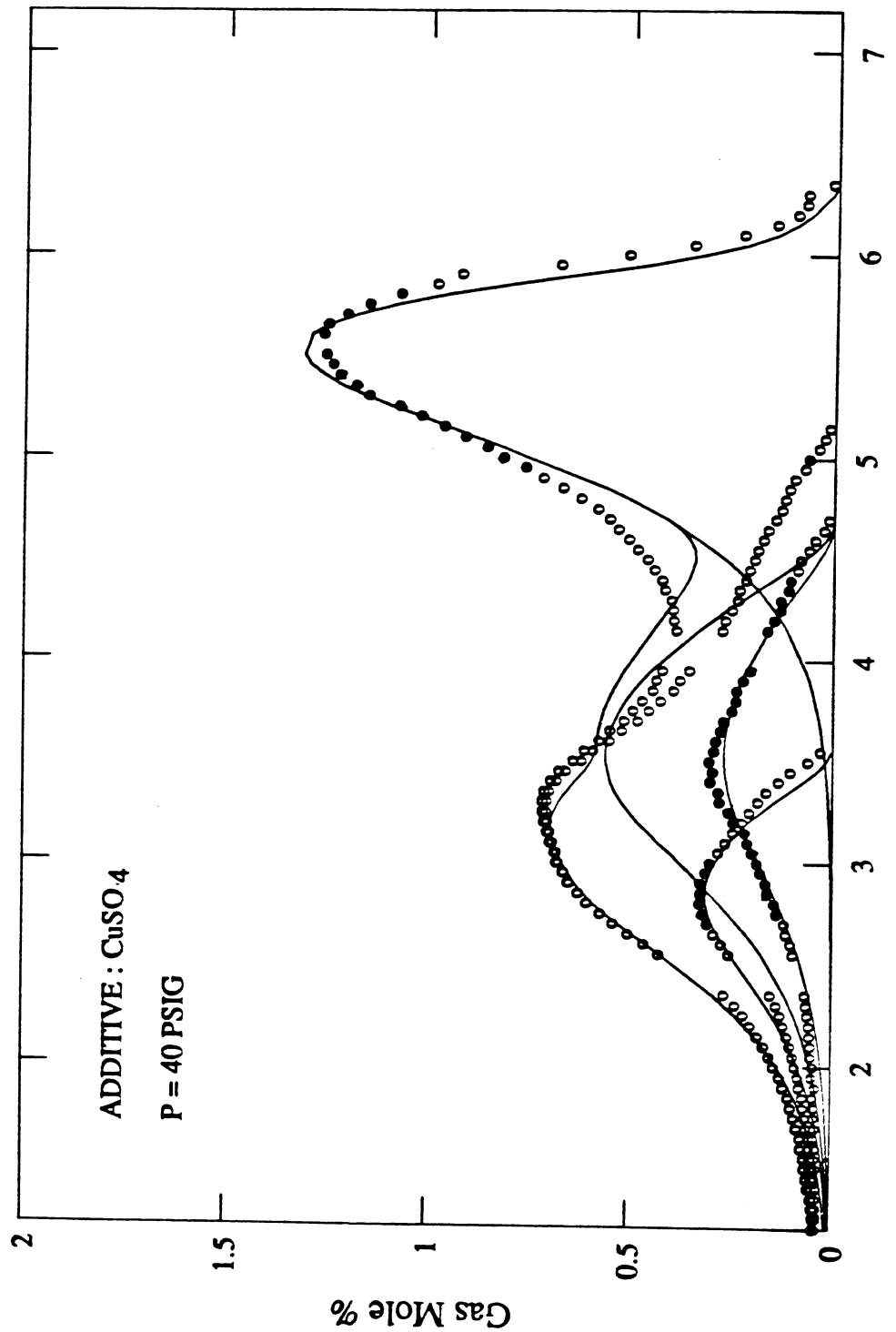

Fig. 6.5. Curve Fit, Run 203, $CuSO_4$ Additive (p = 40 psig).

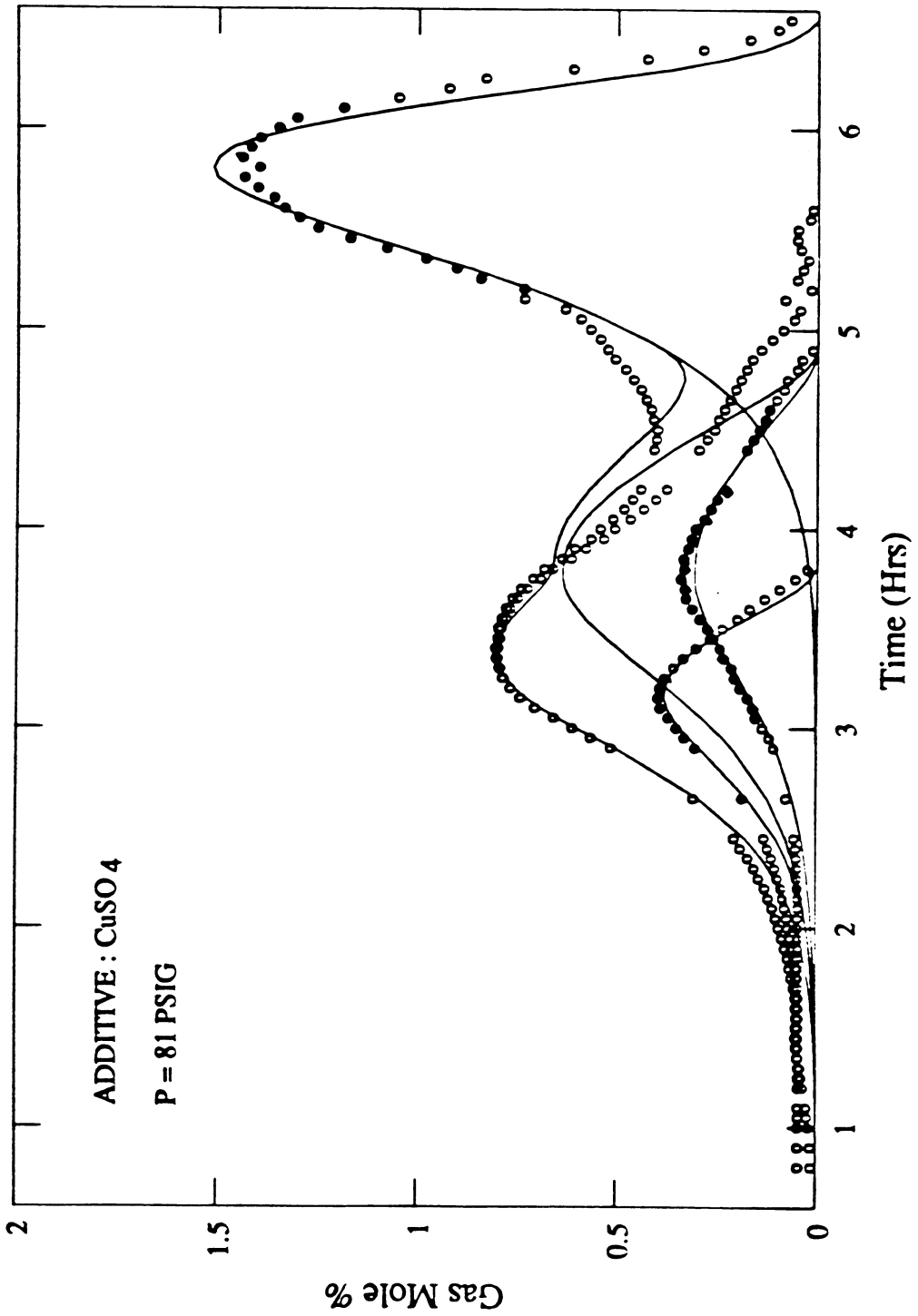

Fig. 6.6. Curve Fit, Run 205, $CuSO_4$ Additive (p = 81 psig).

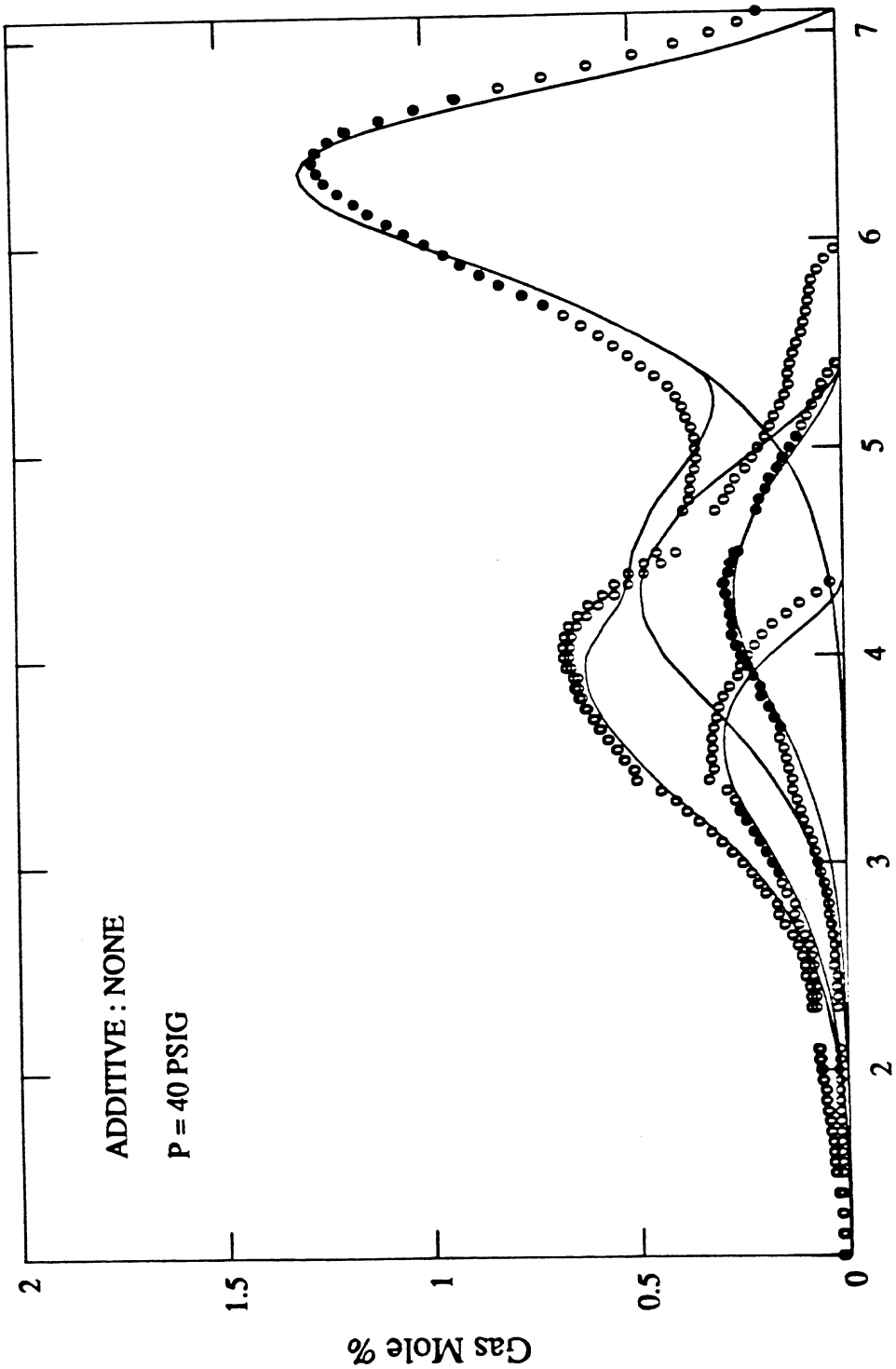

Fig. 6.7. Curve Fit, Run 207, No Additive (p = 40 psig).

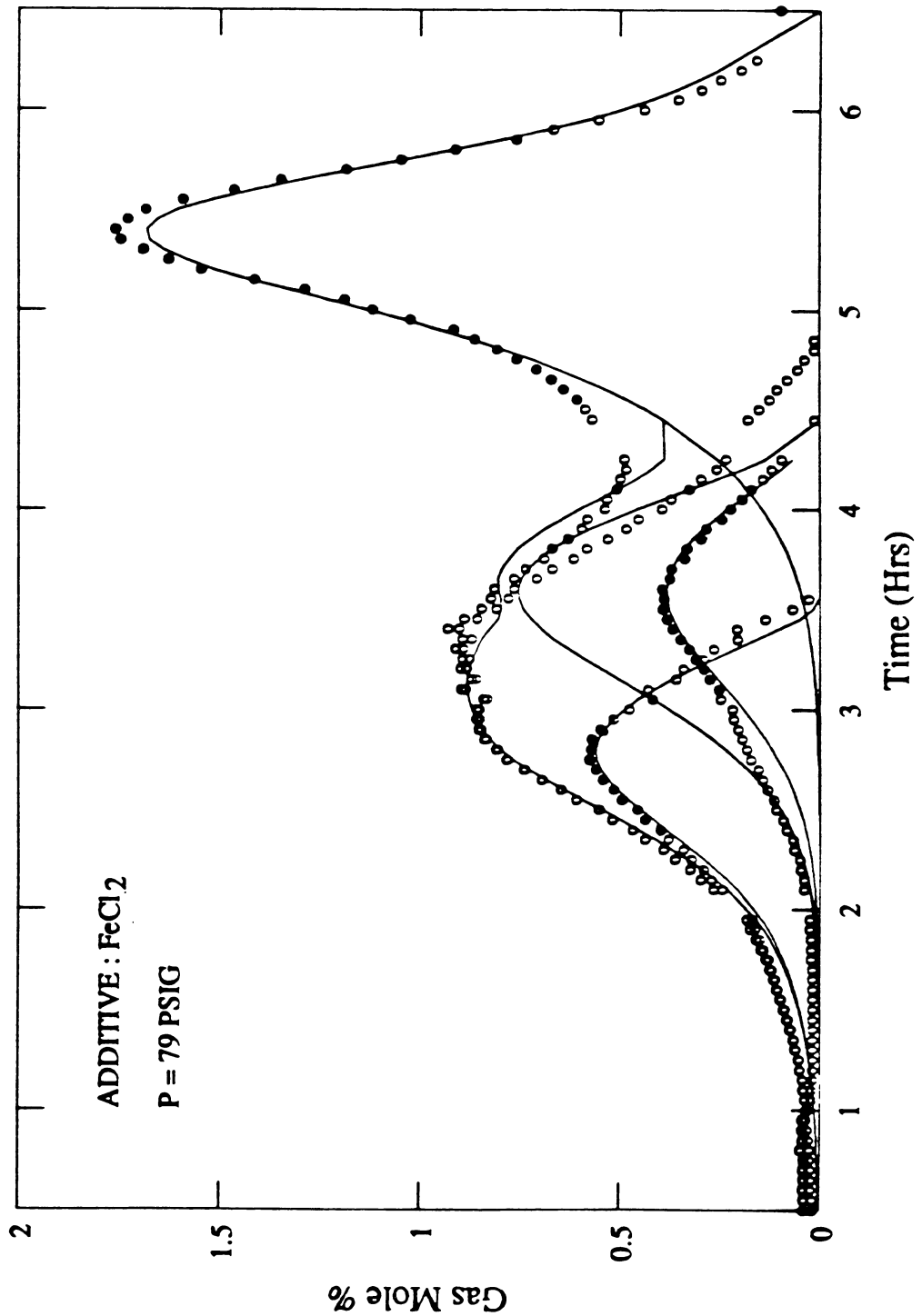

Fig. 6.8. Curve Fit, Run 209, $FeCl_2$ Additive (p = 79 psig).

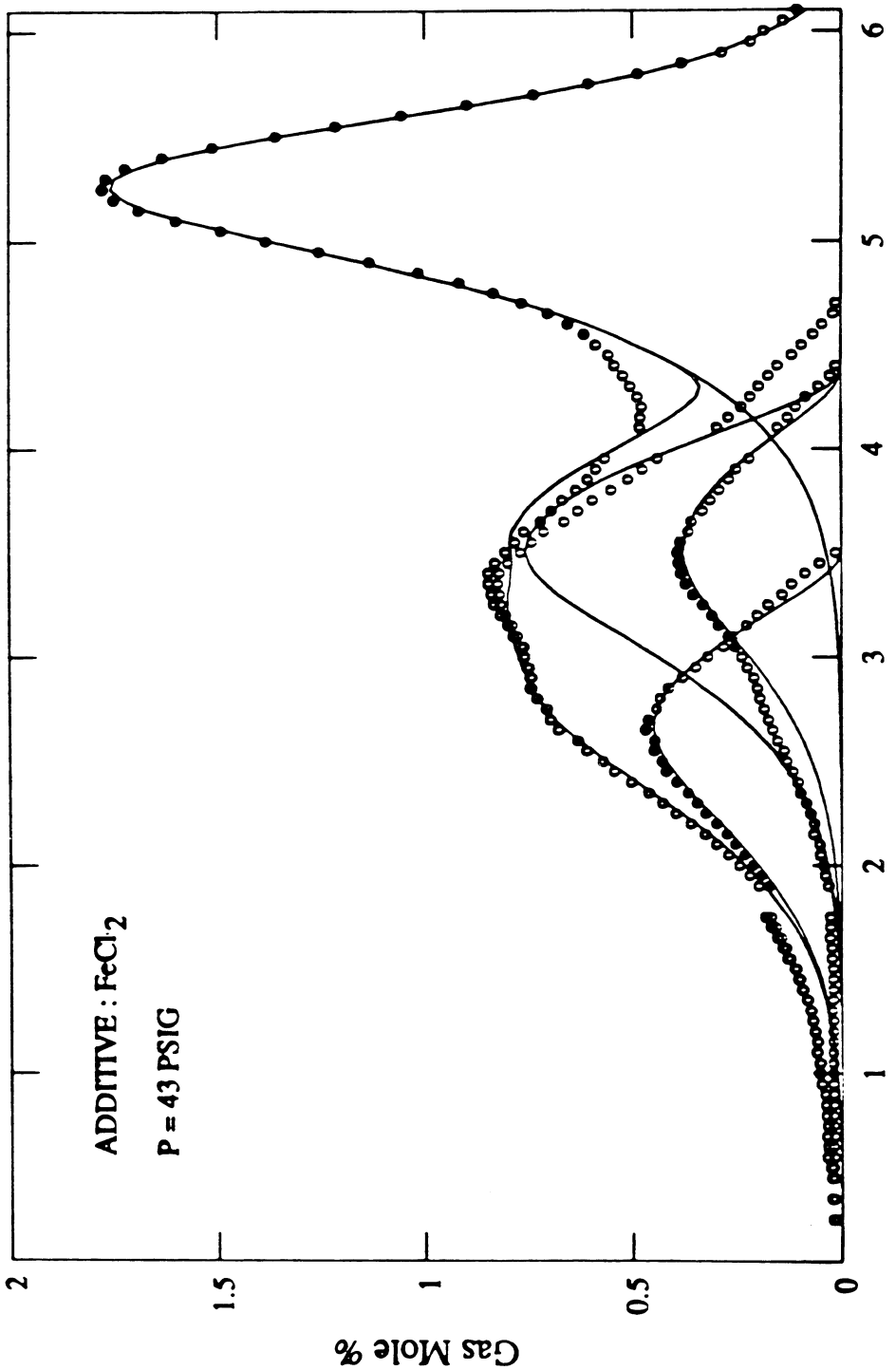

Fig. 6.9. Curve Fit, Run 211, $FeCl_2$ Additive (p = 43 psig).

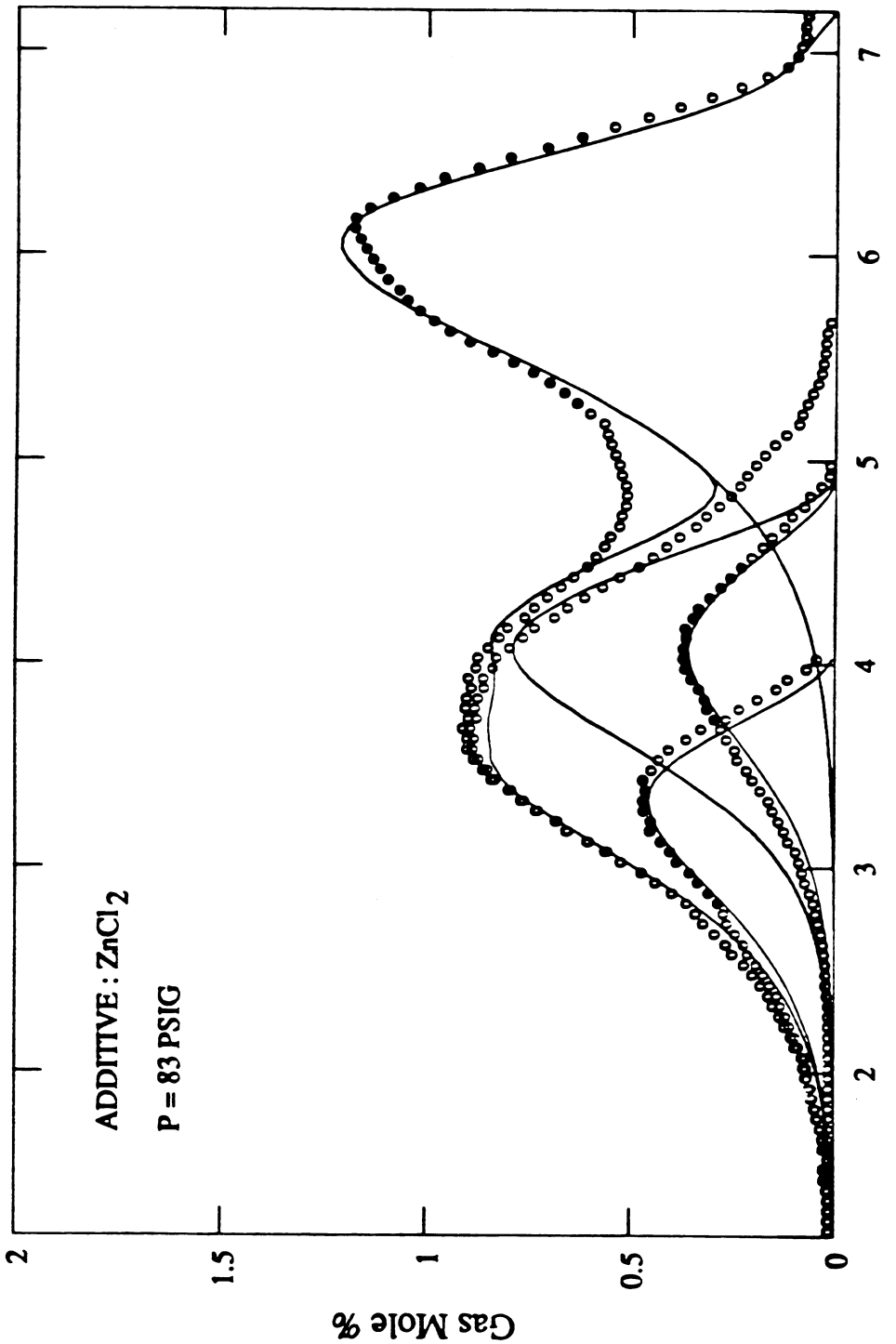

Fig. 6.10. Curve Fit, Run 213, $ZnCl_2$ Additive (p = 83 psig).

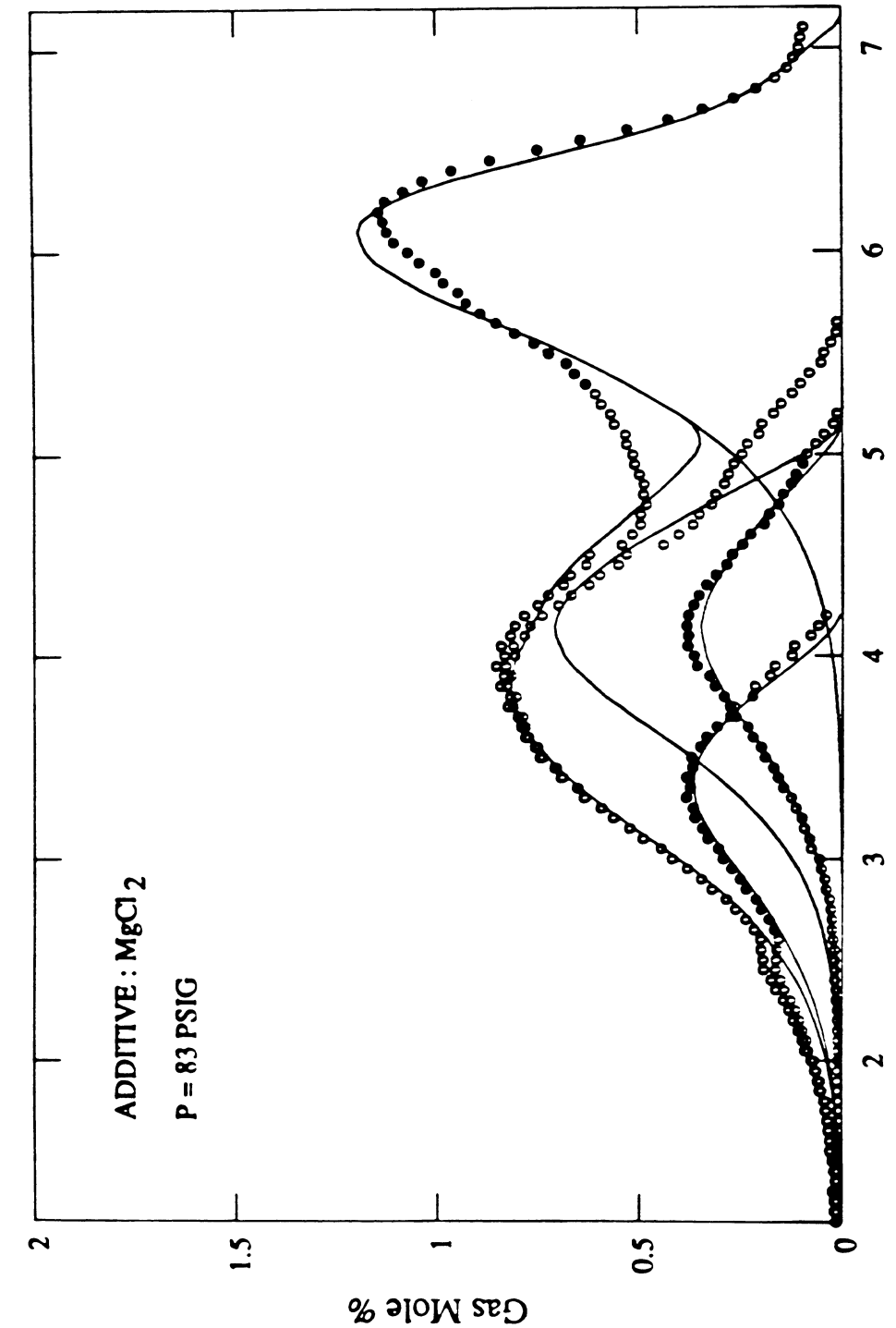

Fig. 6.11. Curve Fit, Run 214, $MgCl_2$ Additive (p = 83 psig).

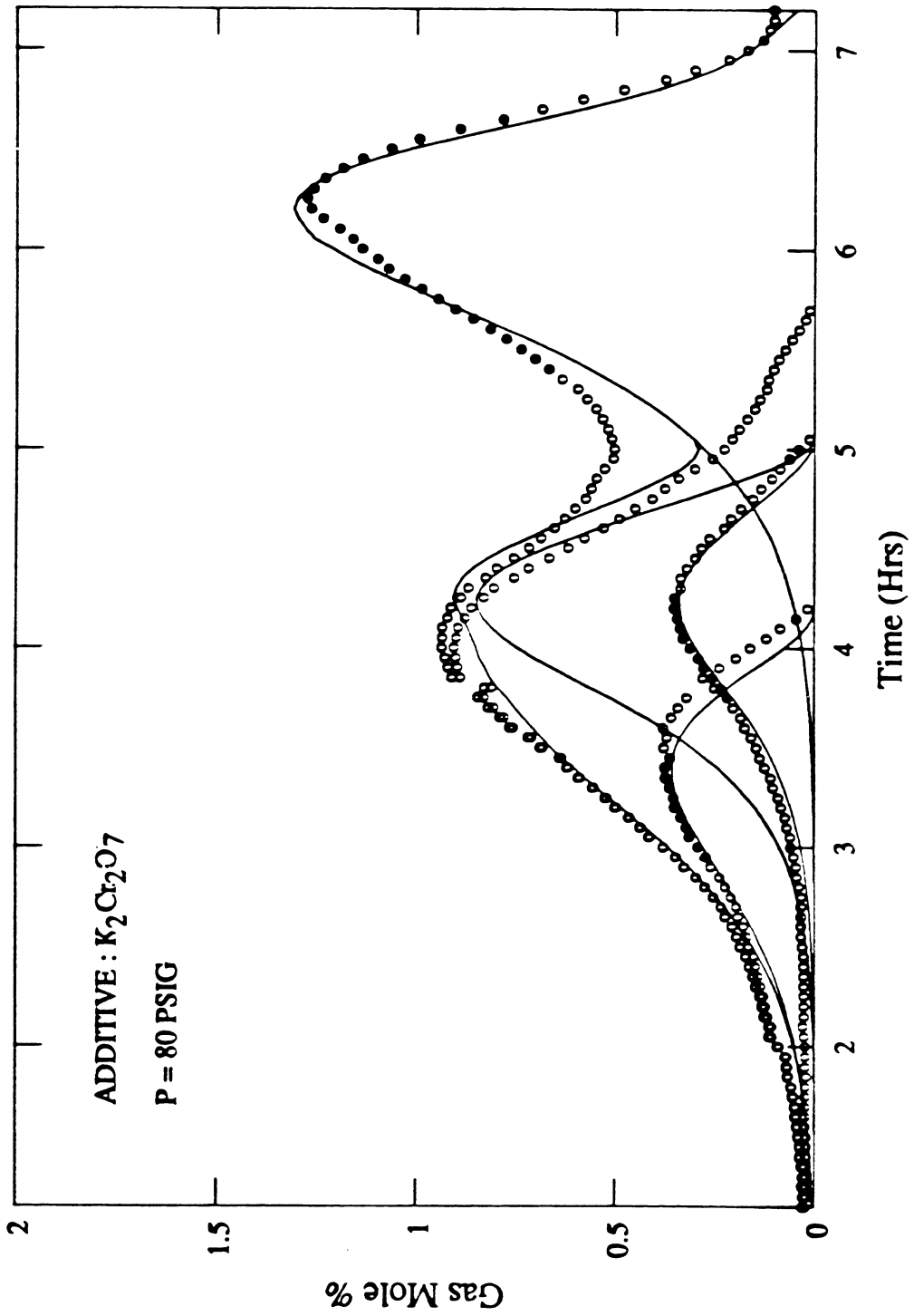

Fig. 6.12. Curve Fit, Run 215, $K_2Cr_2O_7$ Additive (p = 80 psig).

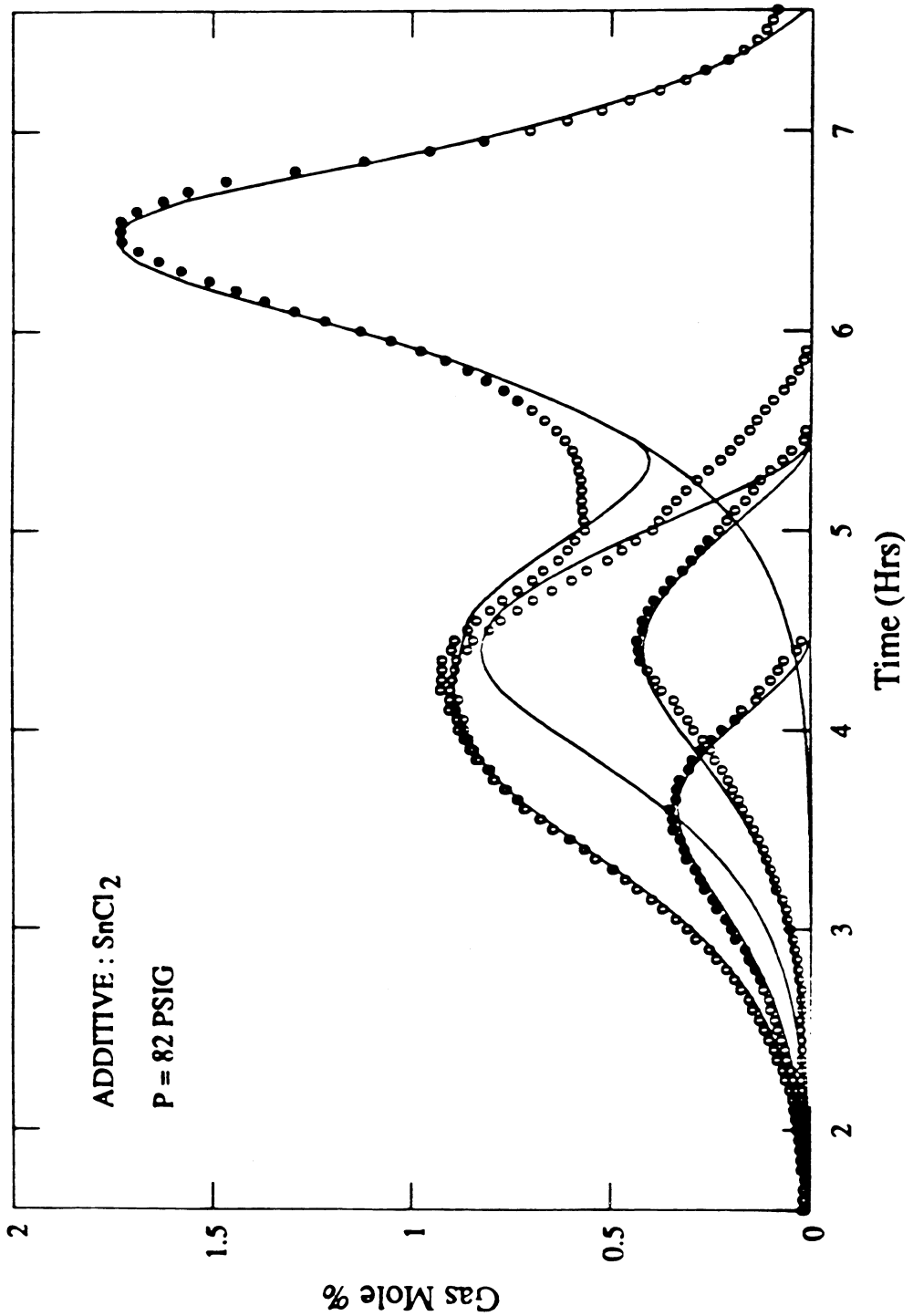

Fig. 6.13. Curve Fit, Run 216, $SnCl_2$ Additive (p = 82 psig).

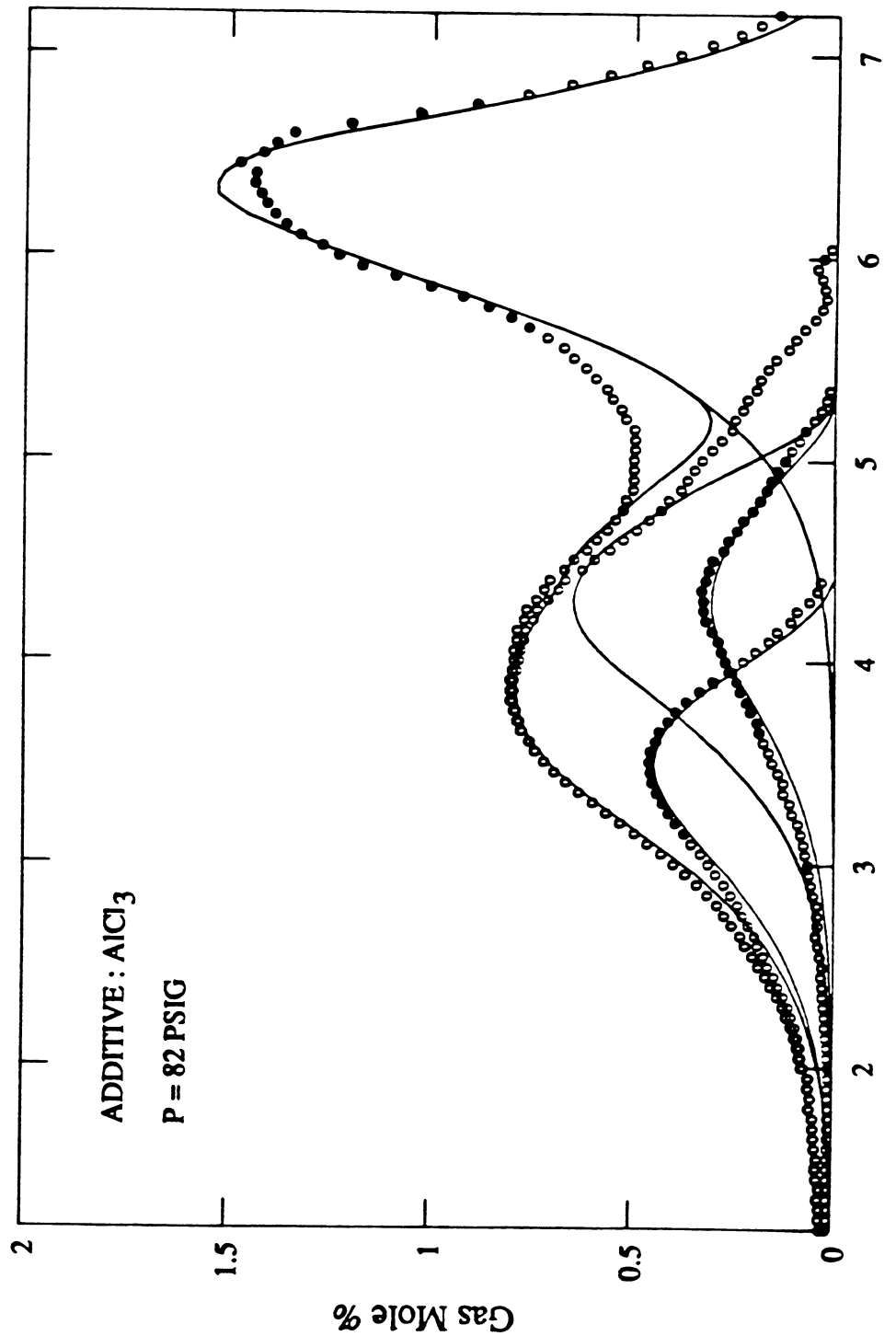

Fig. 6.14. Curve Fit, Run 217, $AlCl_3$ Additive (p = 82 psig).

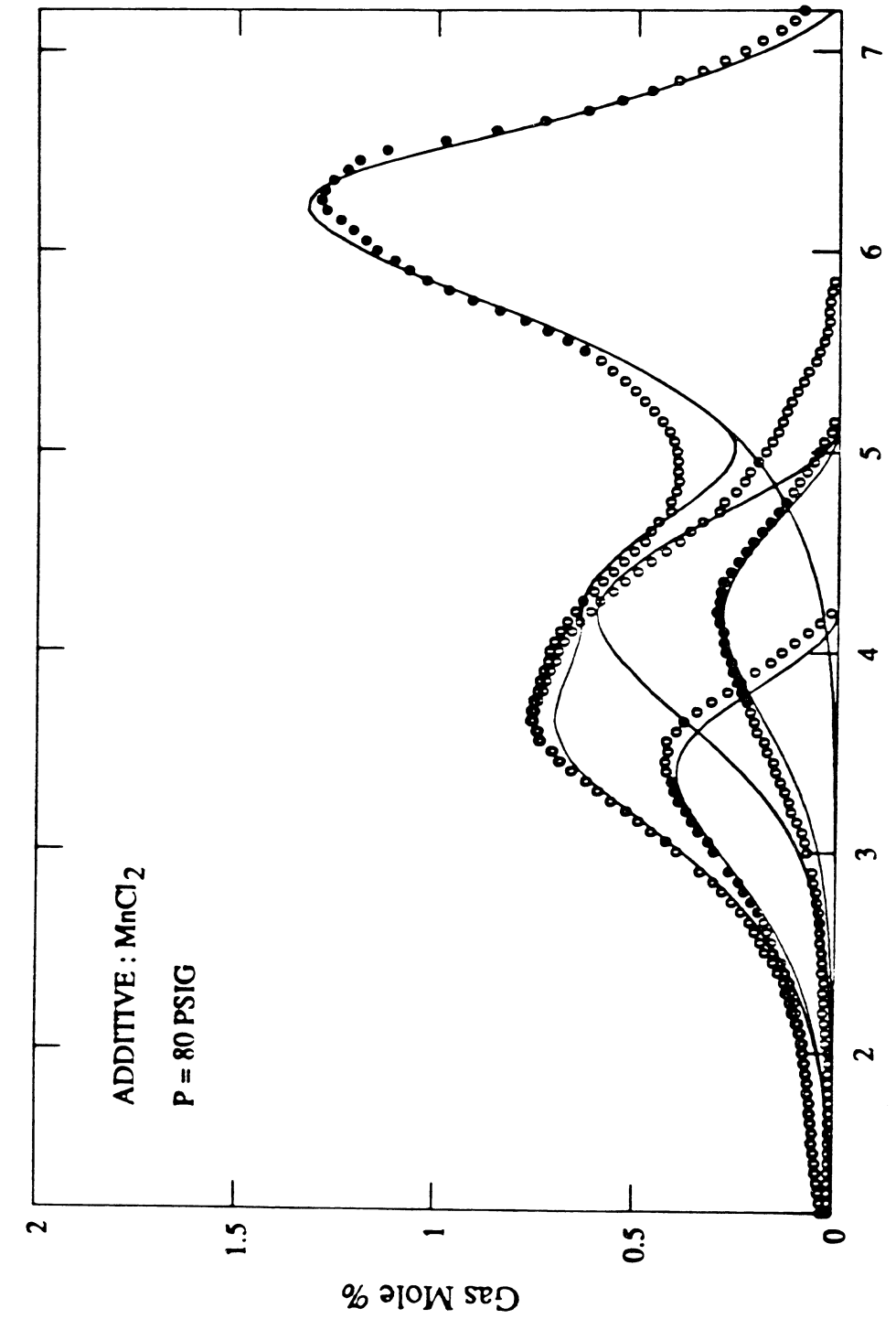

Fig. 6.15. Curve Fit, Run 218, $MnCl_2$ Additive (p = 80 psig).

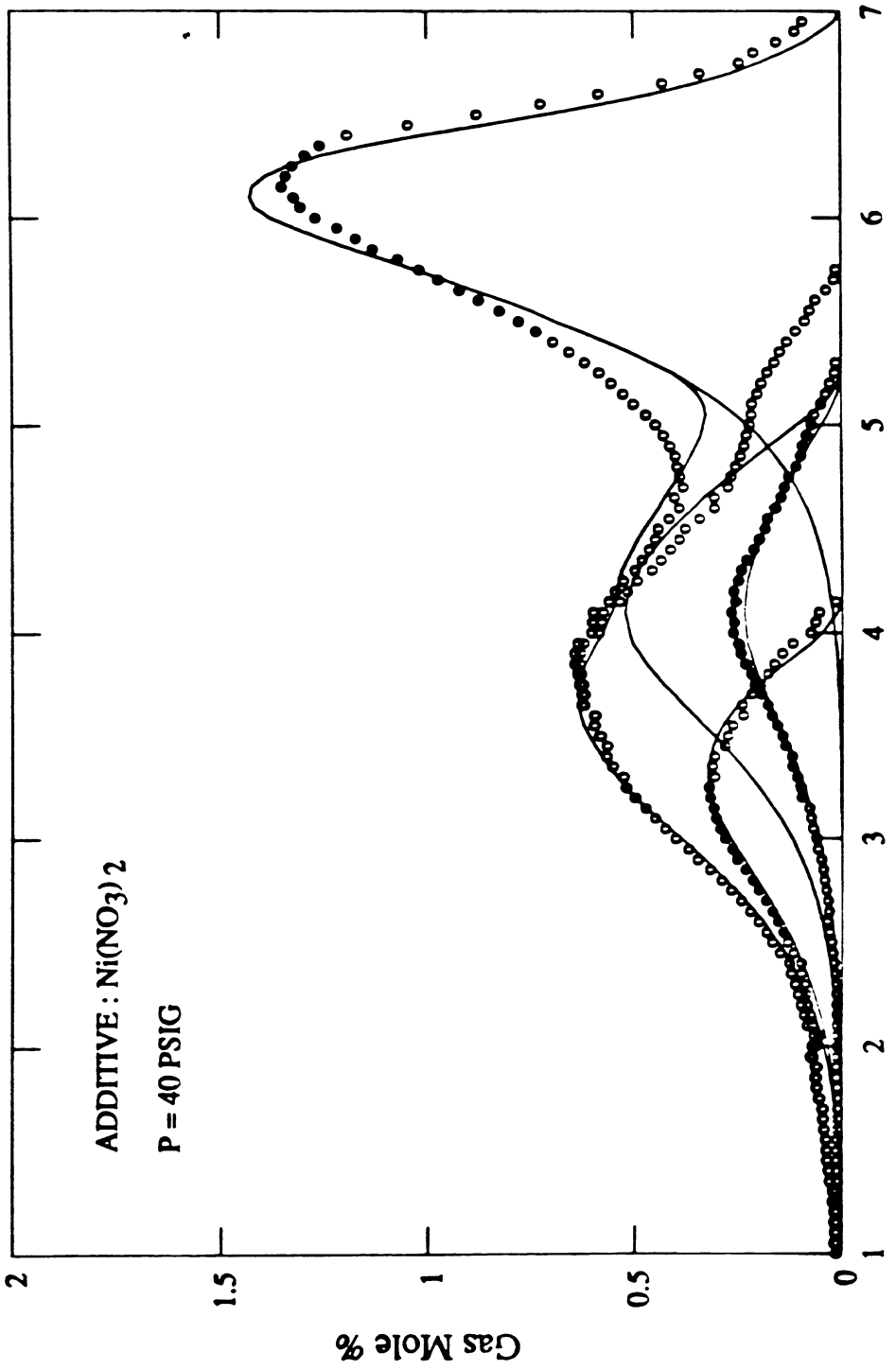

Fig. 6.16. Curve Fit, Run 222, $Ni(NO_3)_2$ Additive (p = 40 psig).

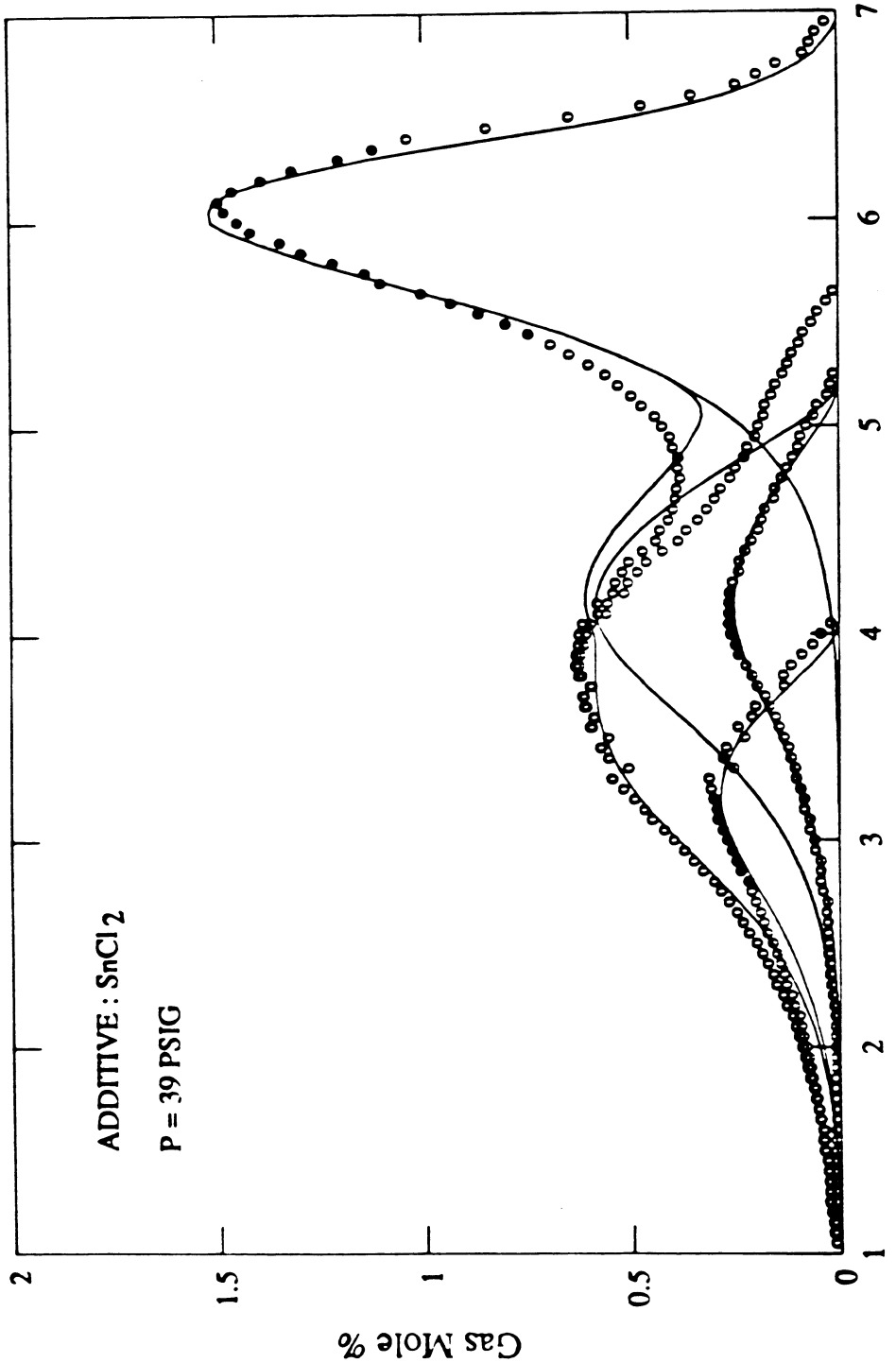

Fig. 6.17. Curve Fit, Run 223, $SnCl_2$ Additive (p = 39 psig).

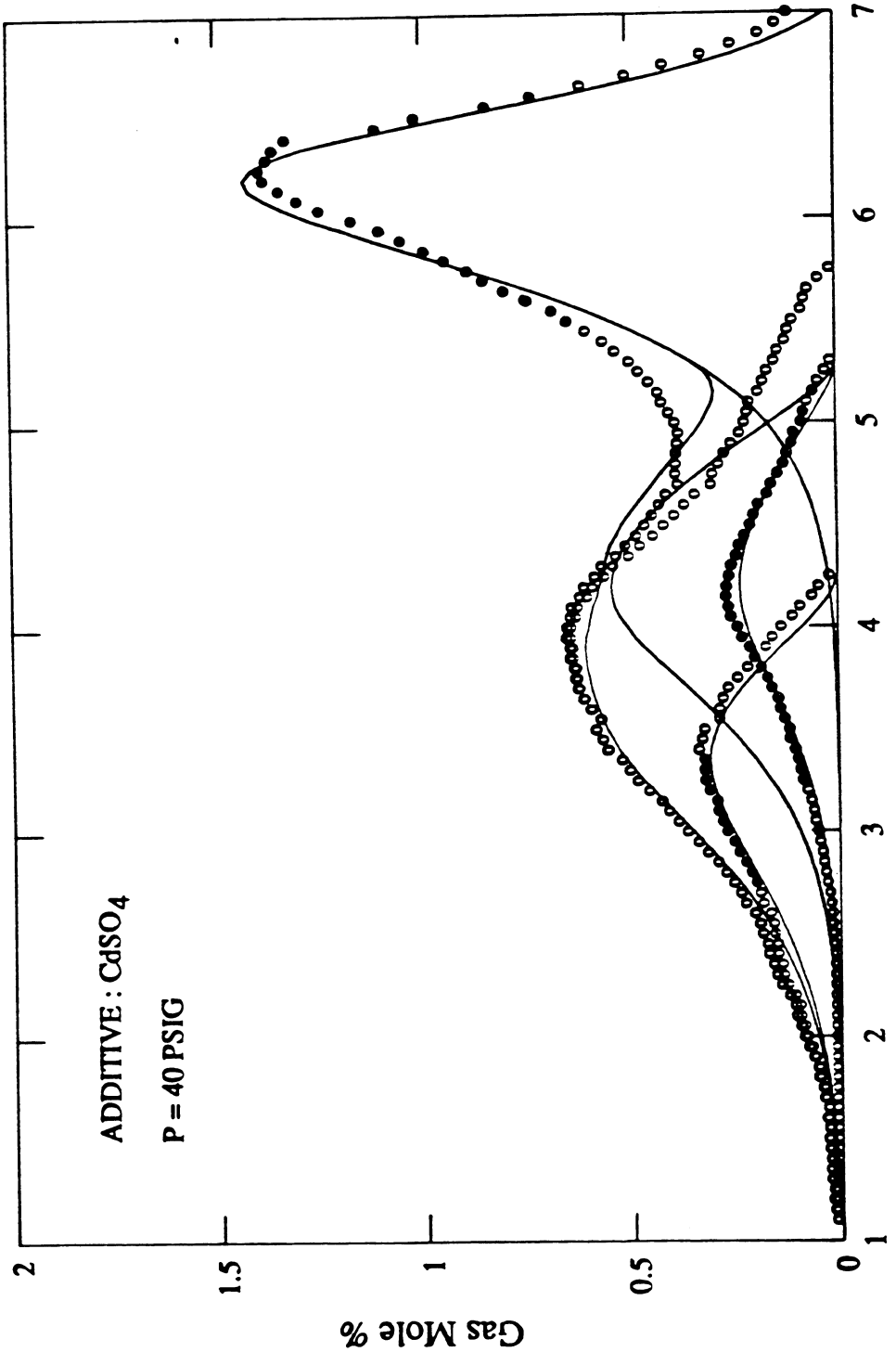

Fig. 6.18. Curve Fit, Run 225, $CdSO_4$ Additive (p = 40 psig).

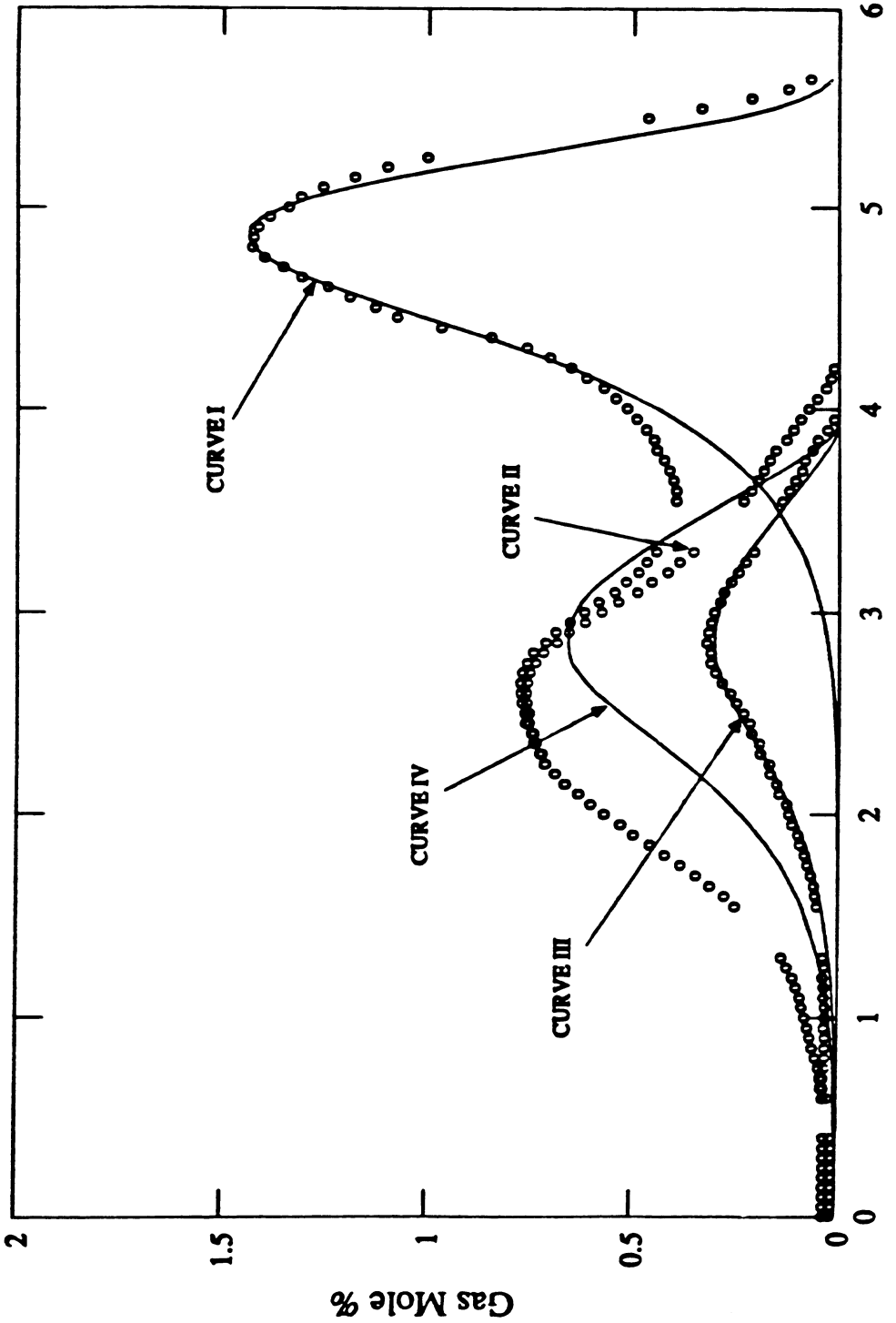

Fig. 6-19a. Decomposition of Medium Temperature Data, Run 201.

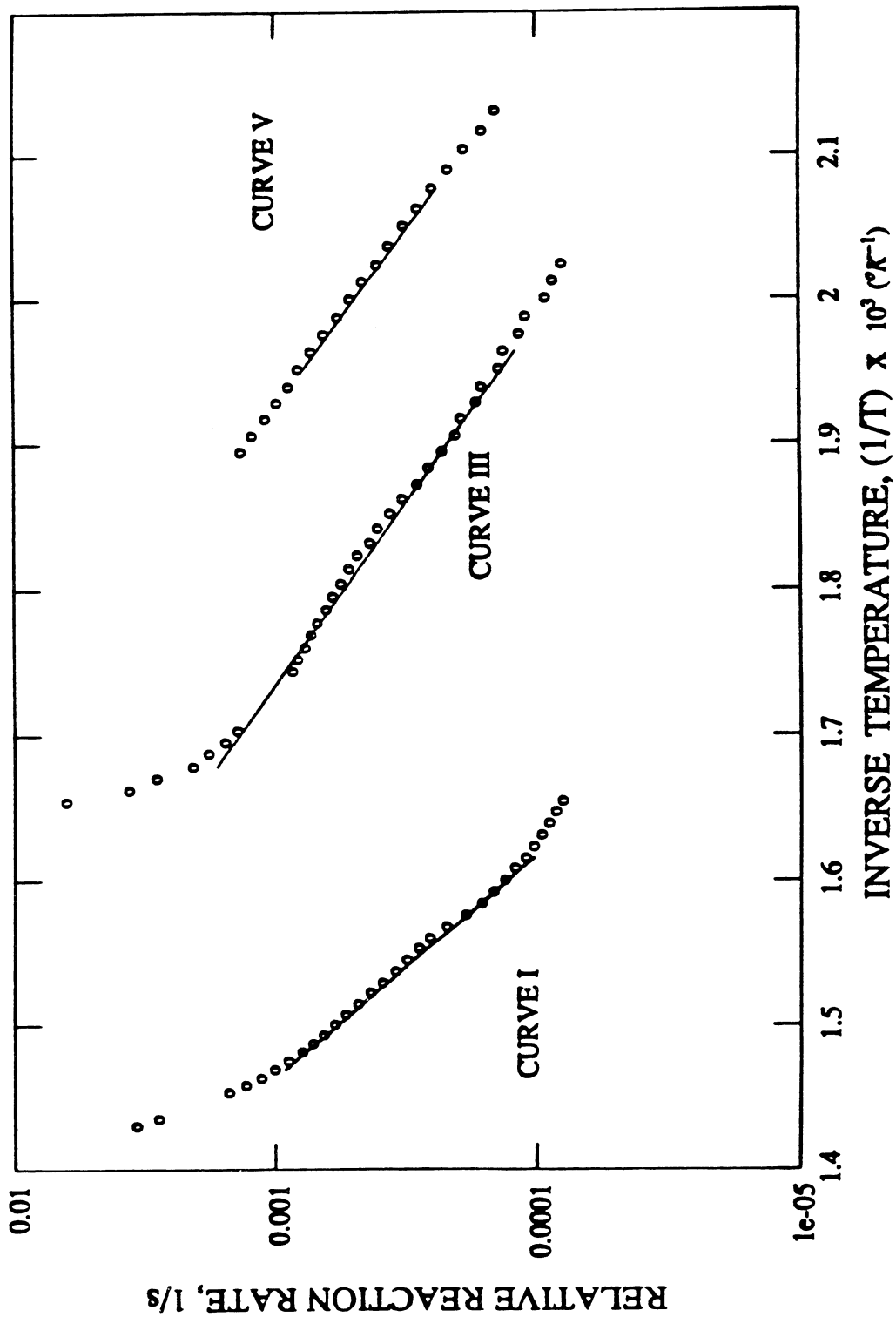

Fig. 6-19b. Arrhenius Graph, Run 201.

It might have been possible to fit the data better by mathematically including an additional reaction between the medium and high temperature peaks; however, such a procedure would have been fraught with even more uncertainty than the present matching system. It would have required a series of additional de-superposition calculations, and thus the results would have been more suspect with no guarantee that the matches would have been any better. Consequently, it was decided to base the comparisons and conclusions on the study of the matches which resulted in Figs. 6.3 to 6.18.

In the remainder of this section, the runs graphed in Figs. 6.3 to 6.18 will be compared with each other, as appropriate, to assess the effects of individual variables on the kinetic behavior.

6.4. PRESSURE EFFECTS

In this section, the effect of differing pressures upon the oxidation reaction kinetics will be examined by comparing effluent gas data and Arrhenius graphs from runs conducted at different pressures. All other operating conditions in these comparisons are nearly identical.

In the effluent gas comparisons, oxygen data for the high pressure runs are always graphed as open circles, carbon monoxide data as asterisks, and carbon dioxide data as open diamonds, while for the low pressure runs, oxygen data are plotted as closed diamonds, carbon monoxide data as closed circles, and carbon dioxide data as closed triangles. In the Arrhenius graphs, high pressure data are always shown as closed circles while the low pressure data are shown as open circles.

Figure 6.20a demonstrates the effect of pressure on the produced gases from runs without additive. Effluent gas data from Run 201 (p = 80 psig), Fig. 6.3, are compared data from Run 202 (p = 43 psig), Fig. 6.4, using the temperature scale for comparison. The clear observation is that at higher pressure, there is an increase in oxygen consumption and carbon oxides production.

The hydrocarbon production rate (HPR) resulting from low temperature distillation was given by Abu-Khamsin (1985) to be:

$$HPR = m_o \, \delta \, exp(\lambda(\tau - T)^2) \tag{6.1}$$

where:

m_o = mass of oil present

τ = constant controlling distillation peak temperature

λ = constant controlling distillation peak spread

δ = constant controlling distillation peak magnitude

Abu-Khamsin showed that as pressure increases, τ increases, λ becomes more negative, and δ decreases. Hence, higher pressures cause the distillation curve to broaden and decrease in magnitude. This suppression of low temperature distillation has the effect of increasing low temperature oxidation (as seen in Fig. 6.20a), since more fuel is available.

In addition, Fig. 6.20a shows increased oxidation at high temperatures. This behavior may be attributed to the effect of higher pressure on low temperature distillation and oxidation. That is, high pressures lead to the formation of more fuel for high temperature combustion.

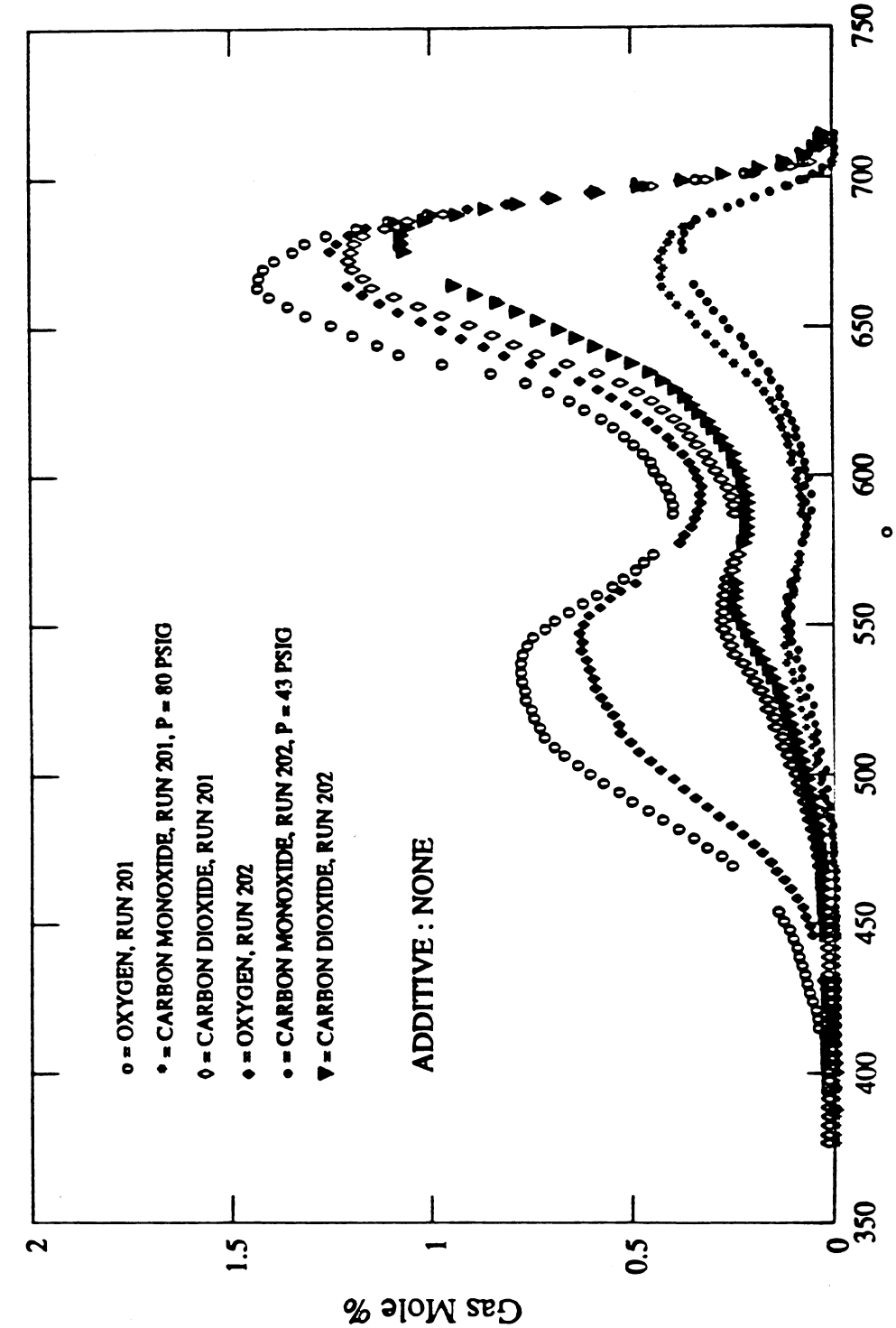

Fig. 6-20a. Effect of Pressure on Effluent Gas Composition: Run 201 (p = 80 psig) and Run 202 (p = 43 psig).

Figure 6.20b shows the effect of pressure on the Arrhenius graphs used to obtain the previously presented curve fits (Figs. 6.3 and 6.4) of these experimental data. In this figure, the straight line sections representing each reaction are plotted for Runs 201 and 202. The lines on the graphs represent the temperature ranges over which the reaction rate parameters were evaluated. As expected, a change in pressure has no effect on the activation energies of the reactions (slopes); however, an increase in pressure produces increased pre-exponential constants ($A_r P_{O_2}^n / \alpha$) for all three reactions. The end result is higher oxidation reaction rates for the high pressure run, which is apparent from the comparison of effluent gas data (Fig. 6.20a).

Comparisons in Table 6.1 of the kinetic parameters from the three runs without additive (Runs 201, 202 and 207), shown in Figs. 6.3, 6.4, and 6.7, show that the calculated activation energies are similar, but not in complete agreement. Again, this discrepancy appears to be an artifact of the data analysis procedure by which the temperature ranges for each reaction are selected. These small variations in calculated activation energies in turn lead to the evaluation of incorrect pre-exponential constants. For example, the calculated pre-exponential constants for the high temperature reaction are greater in Runs 202 and 207, whereas from the graphs of the data it appears that the opposite should be true.

Fassihi (1981) addressed this problem by calculating average activation energies for each reaction from several runs at different pressures. The pre-exponential constants were then re-evaluated using these average activation energies. This procedure requires that many runs would need to be made at different pressures to evaluate the effect of each metal, which was not done for this study due to a lack of time. It therefore appears that the most enlightening diagnostic tool for evaluating the effect of the metals is the visual comparison of effluent gas data in combination with the Arrhenius graphs. This procedure was followed henceforth.

Figure 6.21a shows the effect of differing operating pressures on the effluent gas data for two runs containing copper sulfate additive. In this figure, data from Run 203 (p = 40 psig), Fig. 6.5, is compared with data from Run 205 (p = 81 psig), Fig. 6.6. Qualitatively, the comparison shows that increased pressure has the same relative effect on the reaction rates in the case with $CuSO_4$ added as the case without additive (Fig. 6.20a). That is, increased pressure resulted in increased oxygen consumption and carbon oxides production over the entire temperature range. Figure 6.21b compares the reaction rates of these two runs, as illustrated by their Arrhenius graphs. As was the case without additive, increased pressure caused no appreciable changes in the activation energies (slopes) of any of the reactions. However, higher reaction rates did occur as a result of increased pre-exponential constants (intercepts) in all three reactions.

Note that while the line through the low temperature data for Run 205 appears to indicate a larger activation energy, the actual data points align in a slope nearly equivalent to that of Run 203. This misleading behavior is an artifact of the curve fitting algorithm which occurred in several of the following comparisons. As a consequence, the slopes referred to from this point on are those indicated by the trend in the data points which is not always the same as the trend indicated by the line.

Figure 6.22a shows a comparison of the effluent gas data from Run 209 (p = 43 psig), Fig. 6.8, and Run 211 (p = 79 psig), Fig. 6.9, while Fig. 6.22b compares the Arrhenius graphs for these two runs. These figures illustrate the effect of differing pressure on reaction rates for runs containing ferrous chloride additive. The behavior is qualitatively similar to that shown in the previous comparisons (Figs. 6.20a and 6.21a). The run made at higher pressure (Run 209) showed greater oxygen consumption and carbon oxides production over most of the temperature range. The comparison of Arrhenius graphs for these runs showed that higher pressure resulted in larger reaction rates for the two lower temperature reactions (as a result of larger

TABLE 6-1
CALCULATED KINETIC PARAMETERS

RUN	ADDITIVE	PRESSURE (psig)	LOW TEMPERATURE E/R ($^{\circ}K \times 10^{-3}$)	LOW TEMPERATURE $A_r P_{O_2}^m/\alpha$ (1/s)	MEDIUM TEMPERATURE E/R ($^{\circ}K \times 10^{-3}$)	MEDIUM TEMPERATURE $A_r P_{O_2}^m/\alpha$ (1/s)	HIGH TEMPERATURE E/R ($^{\circ}K \times 10^{-3}$)	HIGH TEMPERATURE $A_r P_{O_2}^m/\alpha$ (1/s)
201	NONE	80	9.45	7.92×10^4	9.26	9.44×10^3	15.0	3.36×10^6
202	NONE	43	9.24	4.16×10^4	9.97	2.91×10^4	15.6	7.26×10^6
207	NONE	40	8.62	7.91×10^3	9.89	2.10×10^4	15.7	7.70×10^6
209	$FeCl_2$	79	8.00	6.02×10^3	10.8	2.60×10^5	14.6	3.02×10^6
211	$FeCl_2$	43	8.65	1.84×10^4	11.3	4.35×10^5	16.5	5.33×10^7
216	$SnCl_2$	82	8.66	2.31×10^4	8.68	4.40×10^3	14.1	1.18×10^6
223	$SnCl_2$	39	8.77	1.92×10^4	9.59	1.39×10^4	17.1	8.47×10^7
203	$CuSO_4$	40	9.62	6.78×10^4	8.87	3.13×10^3	17.0	6.41×10^7
205	$CuSO_4$	81	11.5	3.35×10^6	9.09	5.98×10^3	16.9	6.09×10^7
213	$ZnCl_2$	83	9.19	5.14×10^4	11.2	4.63×10^5	13.1	1.99×10^5
214	$MgCl_2$	83	8.52	1.08×10^4	9.96	3.24×10^4	14.5	1.63×10^6
215	$K_2Cr_2O_7$	80	7.73	3.05×10^3	11.3	5.85×10^5	13.1	2.49×10^5
217	$AlCl_3$	82	8.49	1.27×10^4	9.85	3.27×10^5	15.2	5.62×10^6
218	$MnCl_2$	80	8.59	1.45×10^4	10.6	1.47×10^5	14.6	2.37×10^6
222	$Ni(NO_3)_2$	40	9.16	3.32×10^4	9.70	1.52×10^4	16.8	4.47×10^7
225	$CdSO_4$	40	8.00	3.35×10^3	9.91	2.22×10^4	16.9	5.56×10^7

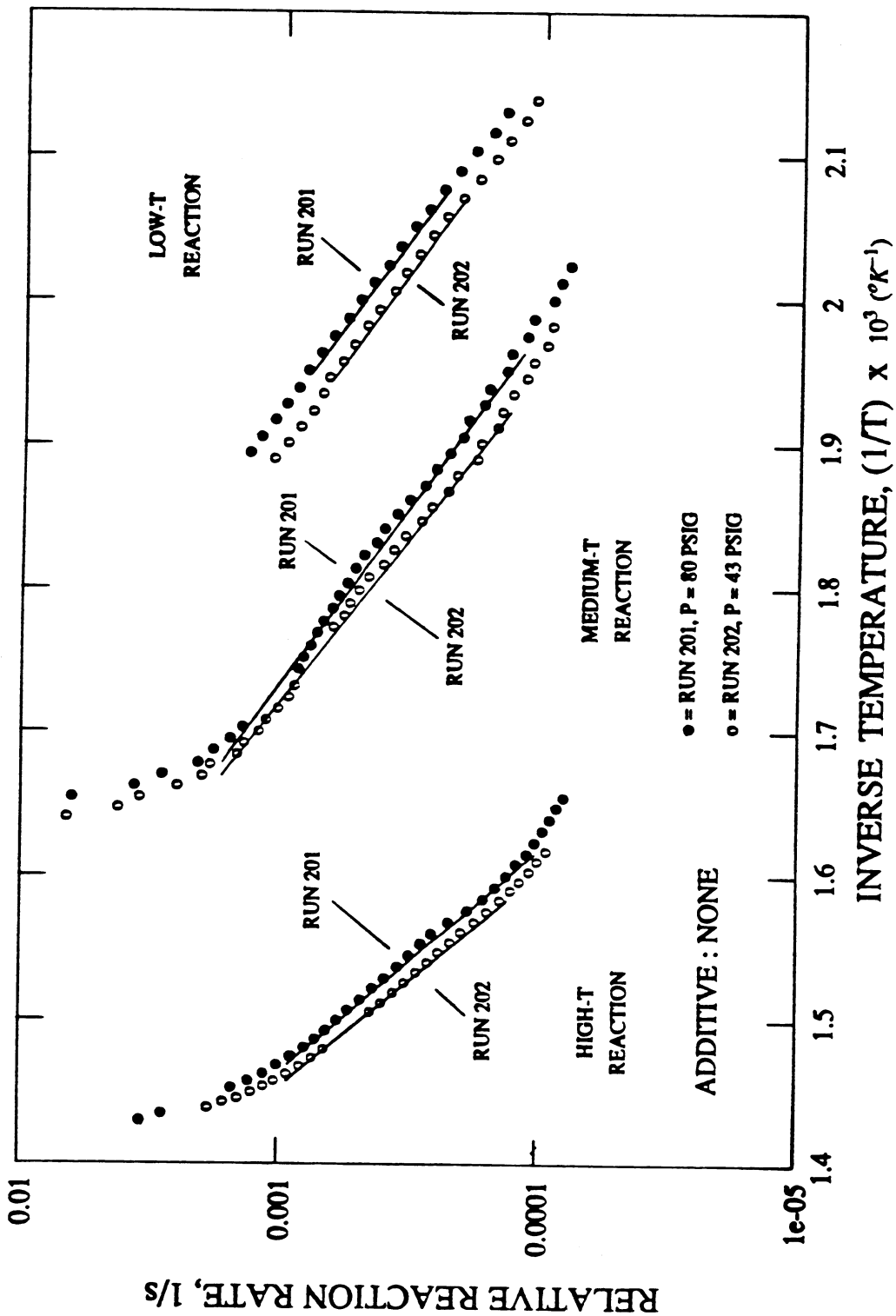

Fig. 6-20b. Effect of Pressure on Arrhenius Graphs: Run 201 (p = 80 psig) and Run 202 (p = 43 psig).

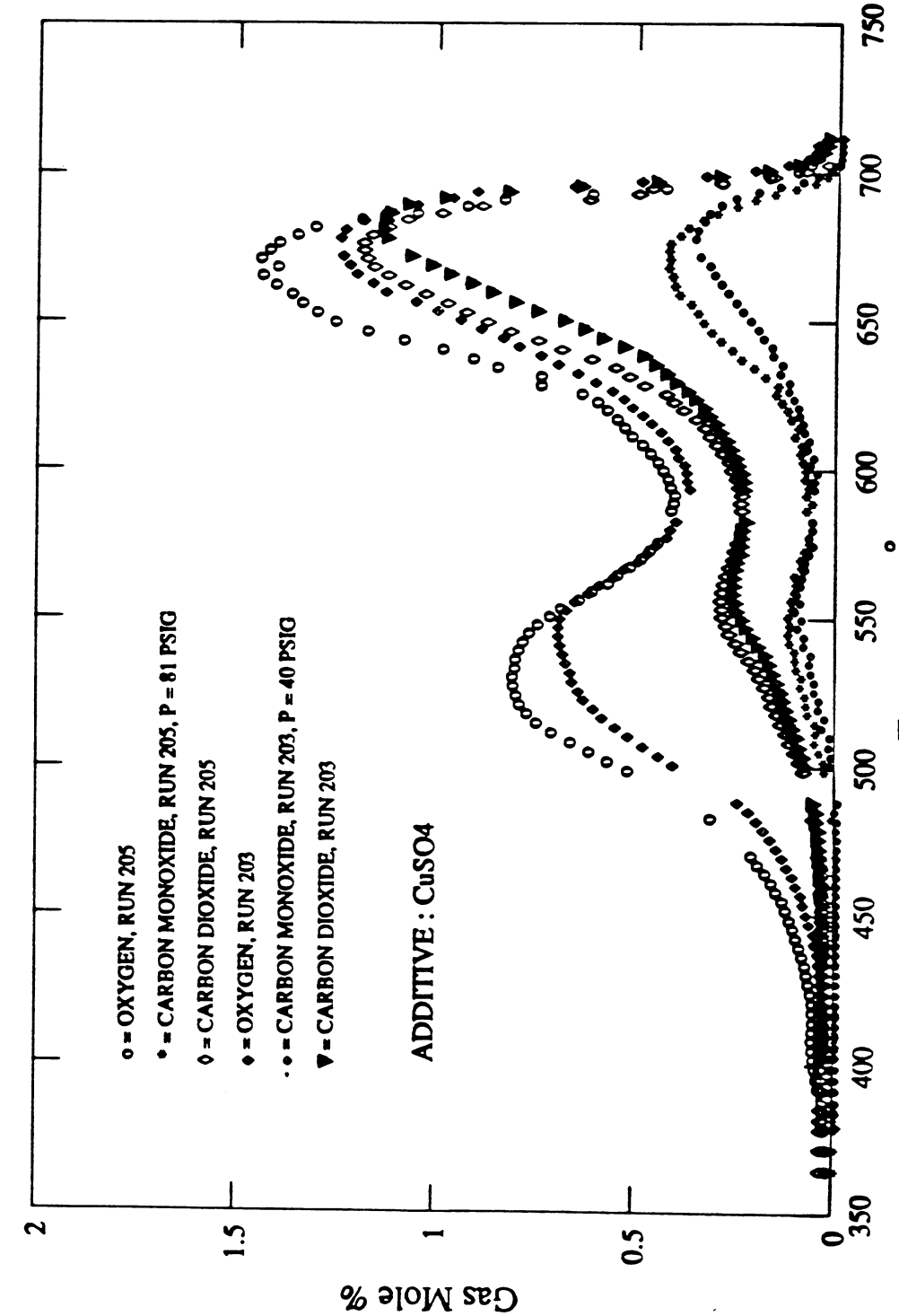

Fig. 6-21a. Effect of Pressure on Effluent Gas Composition with $CuSO_4$ Additive: Run 203 (p = 40 psig) and Run 205 (p = 81 psig).

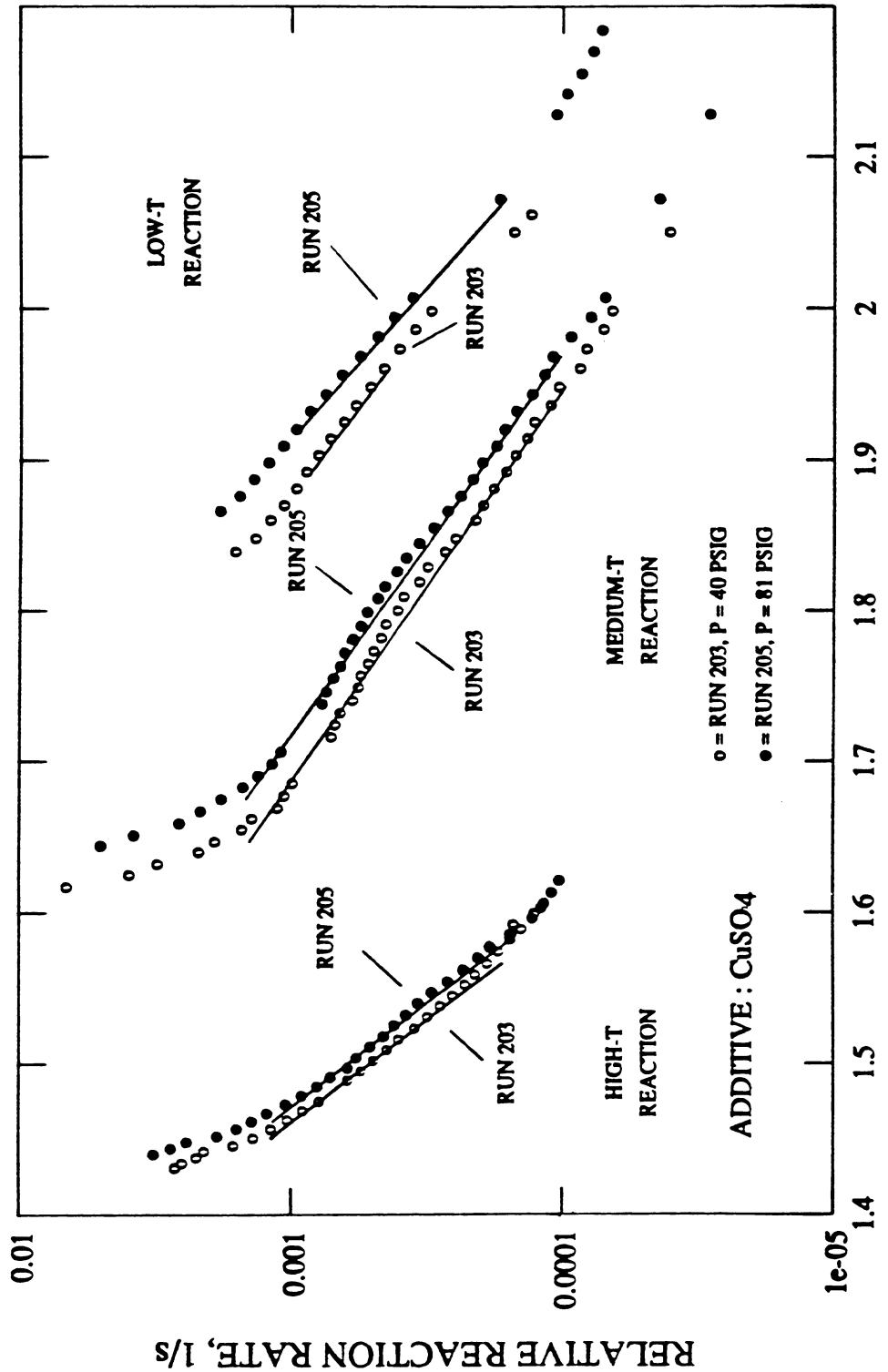

Fig. 6-21b. Effect of Pressure on Arrhenius Graphs with $CuSO_4$ Additive: Run 203 (p = 40 psig) and Run 205 (p = 81 psig).

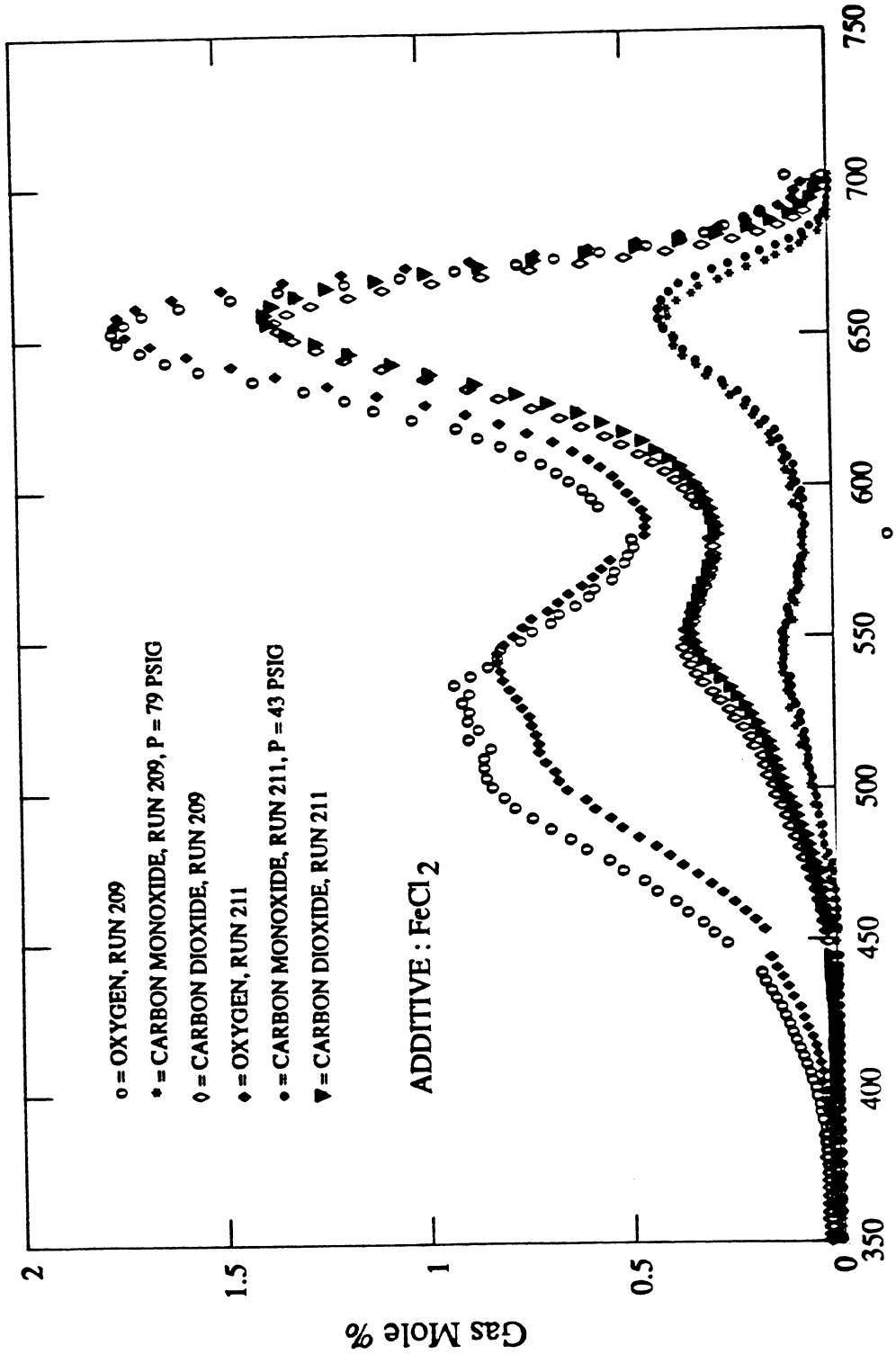

Fig. 6-22a. Effect of Pressure on Effluent Gas Composition with $FeCl_2$ Additive: Run 209 (p = 79 psig) and Run 211 (p = 43 psig).

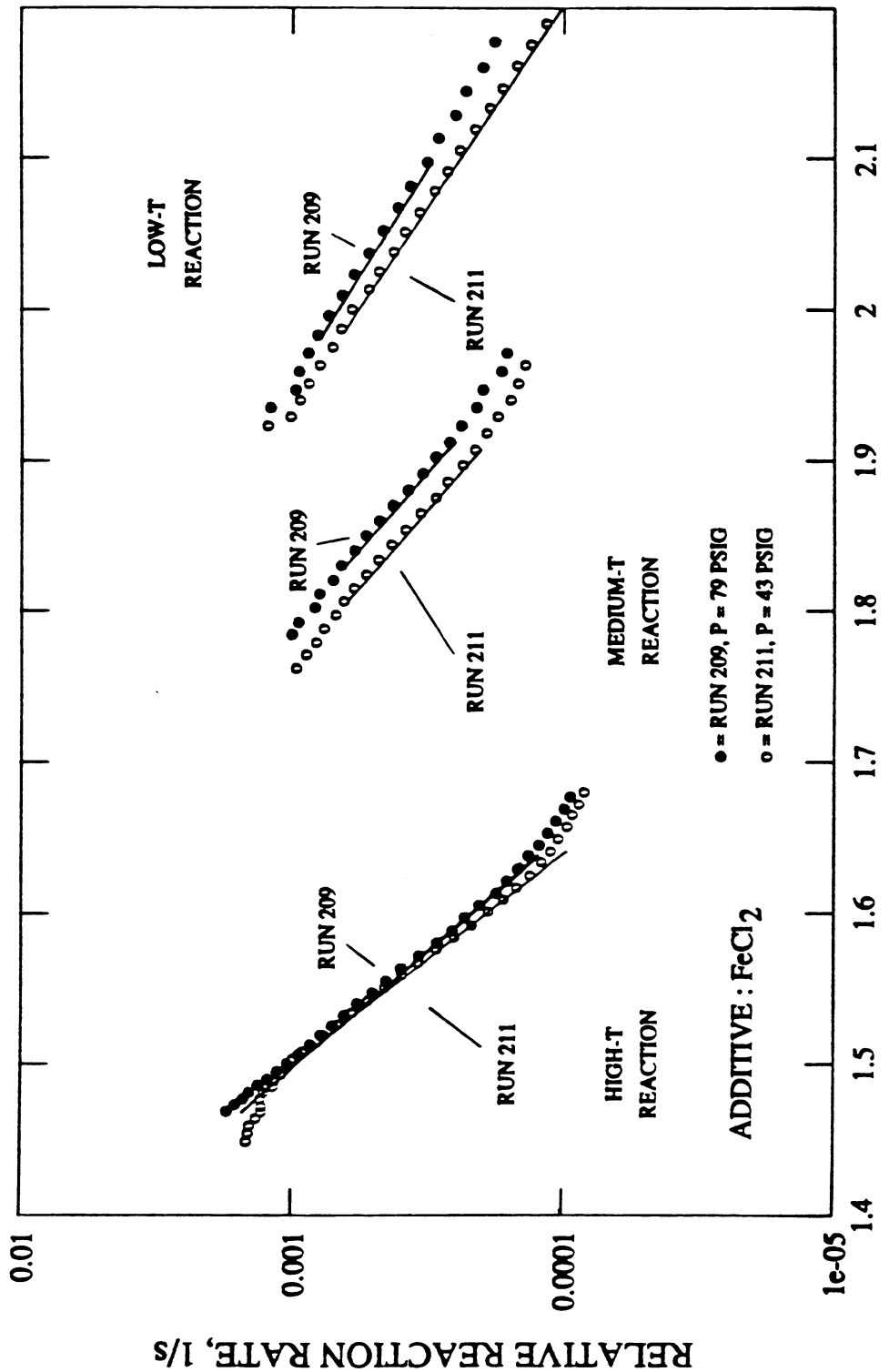

Fig. 6-22b. Effect of Pressure on Arrhenius Graphs with $FeCl_2$ Additive: Run 209 (p = 79 psig) and Run 211 (p = 43 psig).

pre-exponential constants). The activation energies for all three reactions were again unaffected by the differing pressures.

The effect of pressure on the effluent gas data for two runs containing stannous chloride additive is illustrated in Fig. 6.23a, where data from Run 216 (p = 82 psig), Fig. 6.13, is compared with data from Run 223 (p = 39 psig), Fig. 6.17. Again the run made at higher pressure showed greater oxygen reactivity than the run at lower pressure, but to a larger extent than the other pressure comparisons (Figs. 6.20a, 6.21a, and 6.22a). The comparison of Arrhenius graphs for these two runs (Fig. 6.23b) shows higher reactivity for all three reactions in the case of higher pressure. In the lower temperature reactions, this behavior was again the result of increased pre-exponential constants rather than changes in the activation energies. The increase in reaction rates was larger in this case than in the other pressure comparisons (Figs. 6.20b, 6.21b, and 6.22b), which explains the greater reactivity seen at lower temperatures (below 600°K) in the effluent gas comparison (Fig. 6.23a). A lower activation energy, however, is apparent for the high temperature reaction in the high preassure run. This behavior is contrary to the expected result and is contrary to the other comparisons. As a result, these data are somewhat suspect and should probably be re-run, for there is no theoretical reason to expect this behavior.

6.5. THE EFFECT OF METALLIC ADDITIVES

In this section, the effect of different metallic additives on the oxidation reaction kinetics of the Huntington Beach crude oil will be examined by directly comparing effluent gas data and Arrhenius graphs from runs containing metallic additives to runs without an additive. Again, all other operating conditions were as nearly equivalent as possible in these comparisons.

In the first eight comparisons, data from runs containing metallic additives are compared with data from Run 201 (no additive, p = 80 psig), Fig. 6.3. The last two comparisons, for nickel and cadmium additives, were made at lower pressure. Data from these runs are therefore compared with data from Run 202 (no additive, p = 43 psig), Fig 6.4.

In order to standardize the comparisons, the data are plotted in the following manner. In the effluent gas comparisons, oxygen data from the runs with additive are plotted as open circles, carbon monoxide data as asterisks, and carbon dioxide data as open diamonds, while in the runs without additive, oxygen data are plotted as closed diamonds, carbon monoxide data as closed circles, and carbon dioxide data as closed triangles. In the Arrhenius graph comparisons, the runs with additive are plotted as open circles while the runs without additive are shown as closed circles.

The effect on the effluent gas data of addition of ferrous chloride is shown in Fig. 6.24a. In this figure, effluent gas composition data versus temperature from Run 201 with no additive are compared with data from Run 209 ($FeCl_2$ added), Fig. 6.8. The presence of this metallic salt caused significant changes in the rates of oxidation of the oil. Oxygen consumption and carbon oxides production began at lower temperatures and increased in magnitude. This increase in low temperature oxidation caused increased fuel deposition which, in turn, resulted in increased high temperature combustion, hence a greater oxygen requirement. In addition, high temperature combustion peaked at lower temperature and occurred over a narrower temperature range.

Figure 6.24b compares data from the same runs on Arrhenius graphs. This figure illustrates the effect of iron chloride on the rates of reactions compared to the rates when no

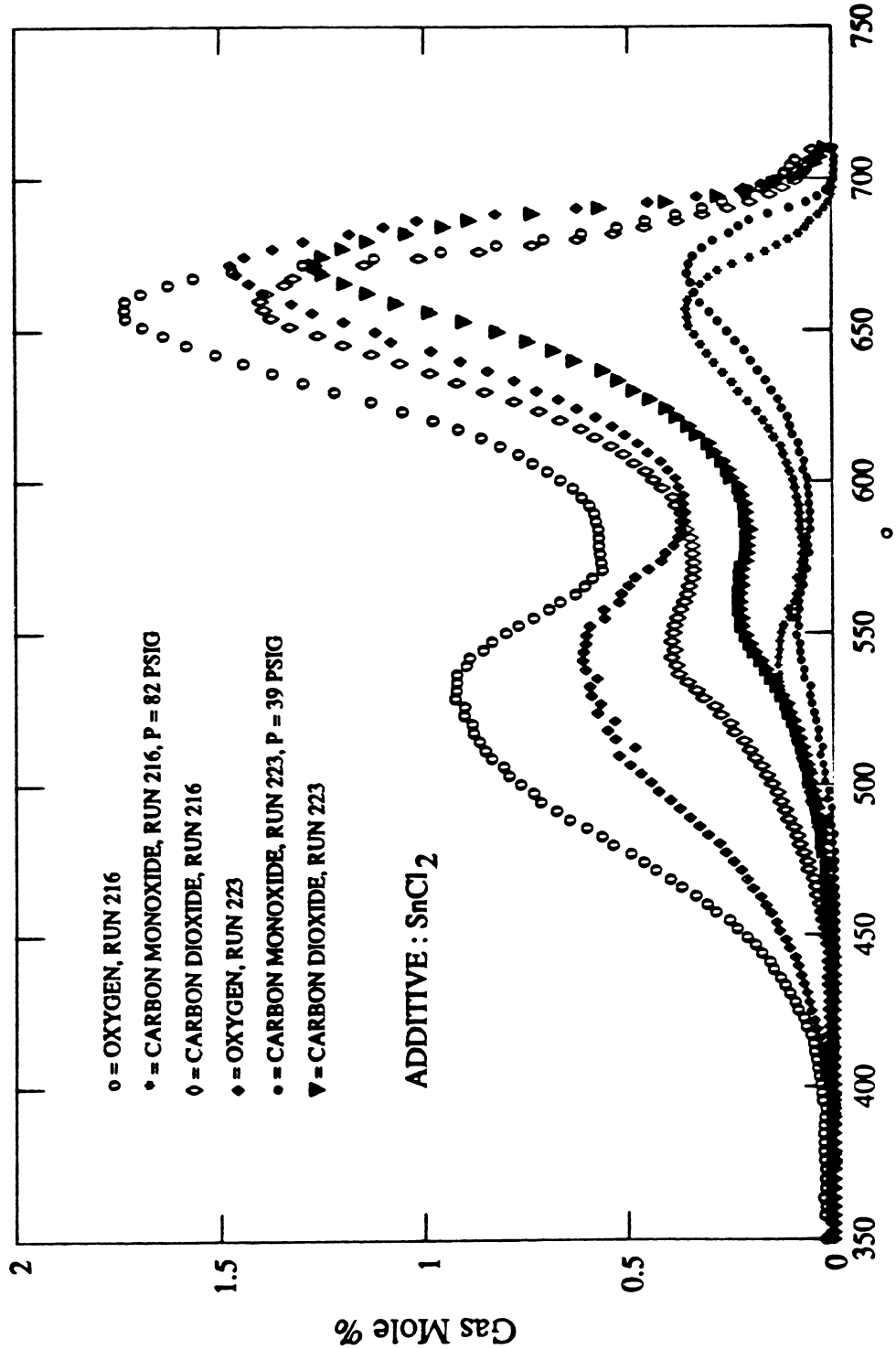

Fig. 6-23a. Effect of Pressure on Effluent Gas Composition with $SnCl_2$ Additive: Run 216 (p = 82 psig) and Run 223 (p = 39 psig).

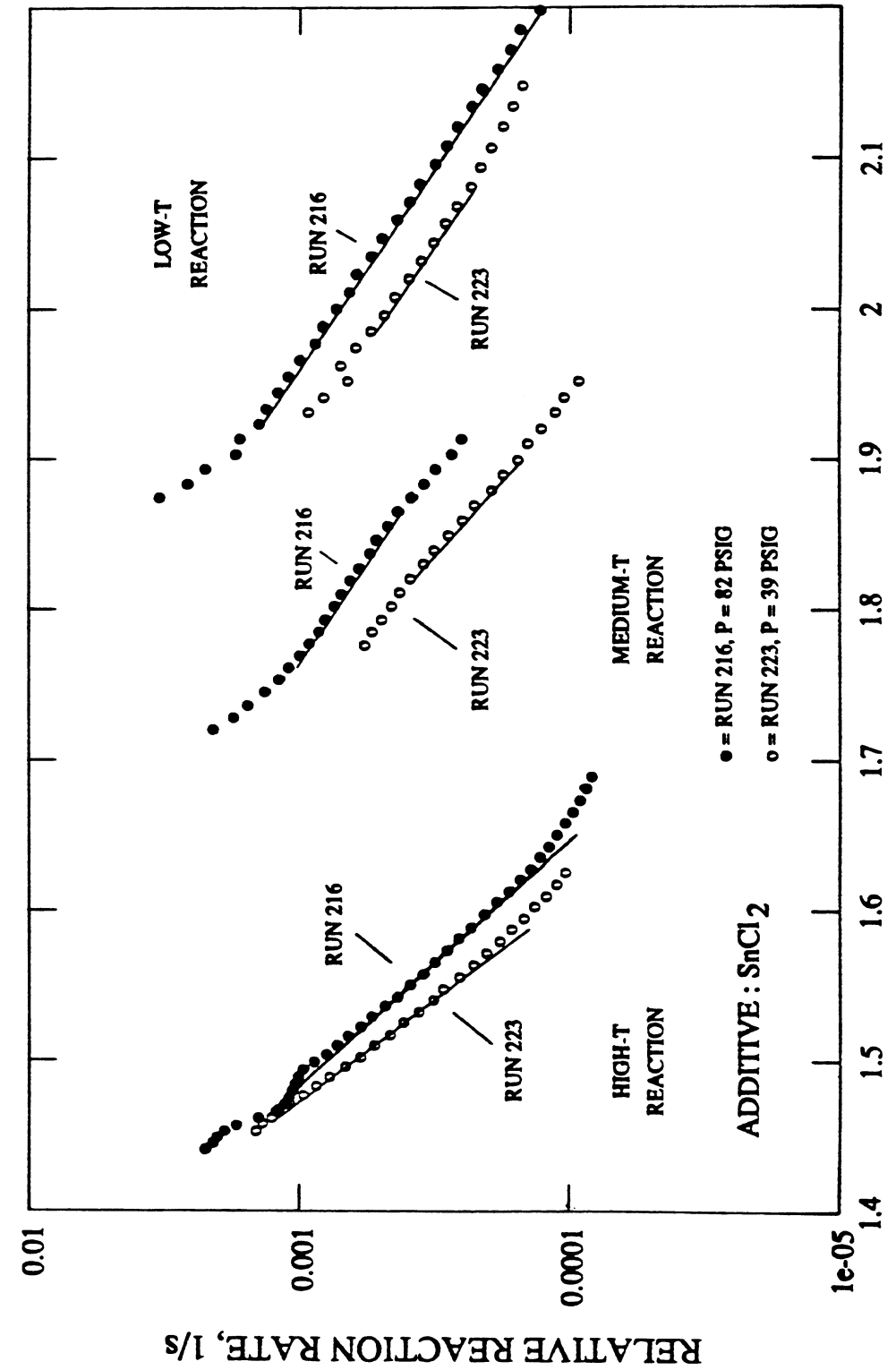

Fig. 6-23b. Effect of Pressure on Arrhenius Graphs with $SnCl_2$ Additive: Run 216 (p = 82 psig) and Run 223 (p = 39 psig).

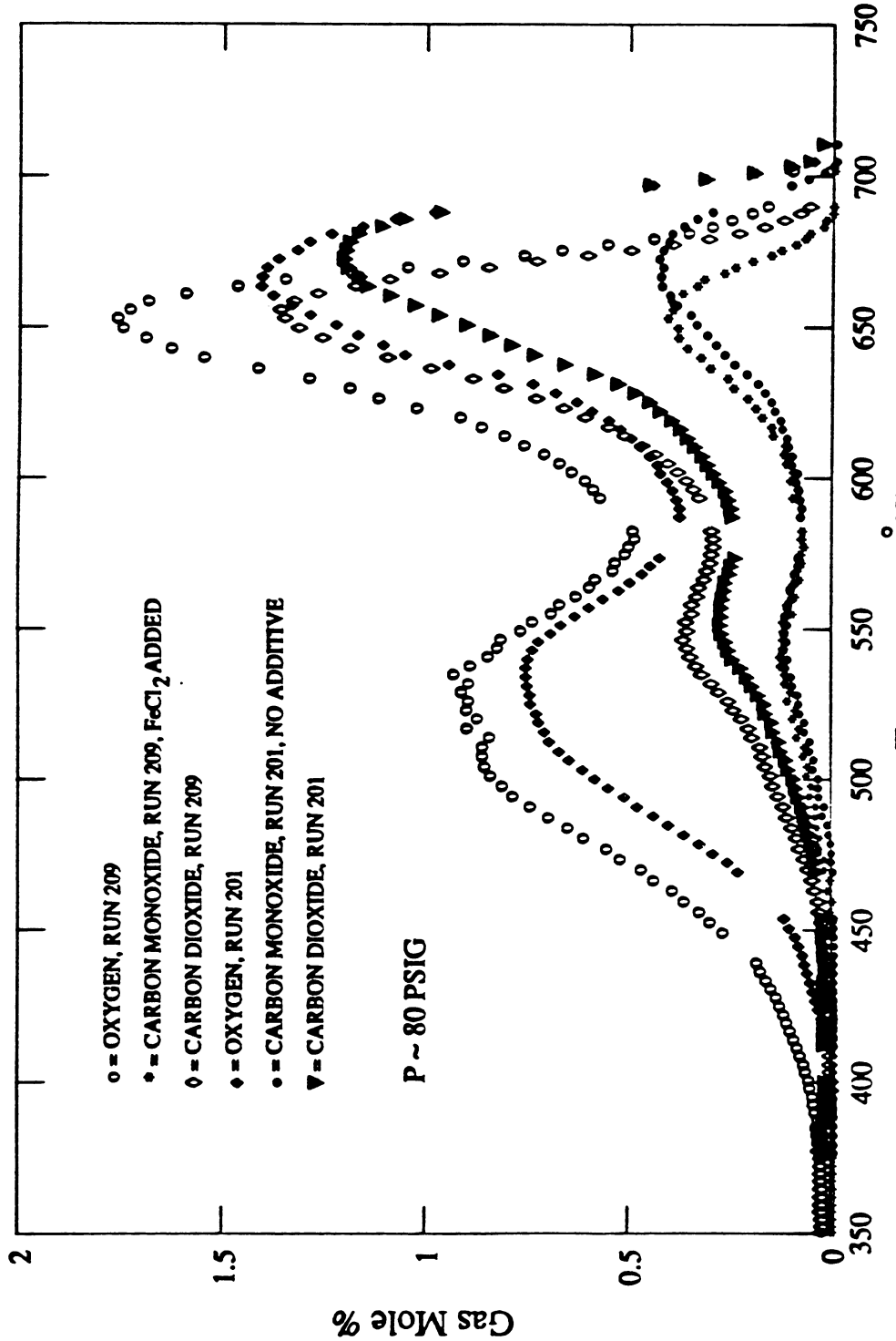

Fig. 6-24a. Effect of $FeCl_2$ Additive on Effluent Gas Composition: Run 201 (No Additive) and Run 209 ($FeCl_2$ Added).

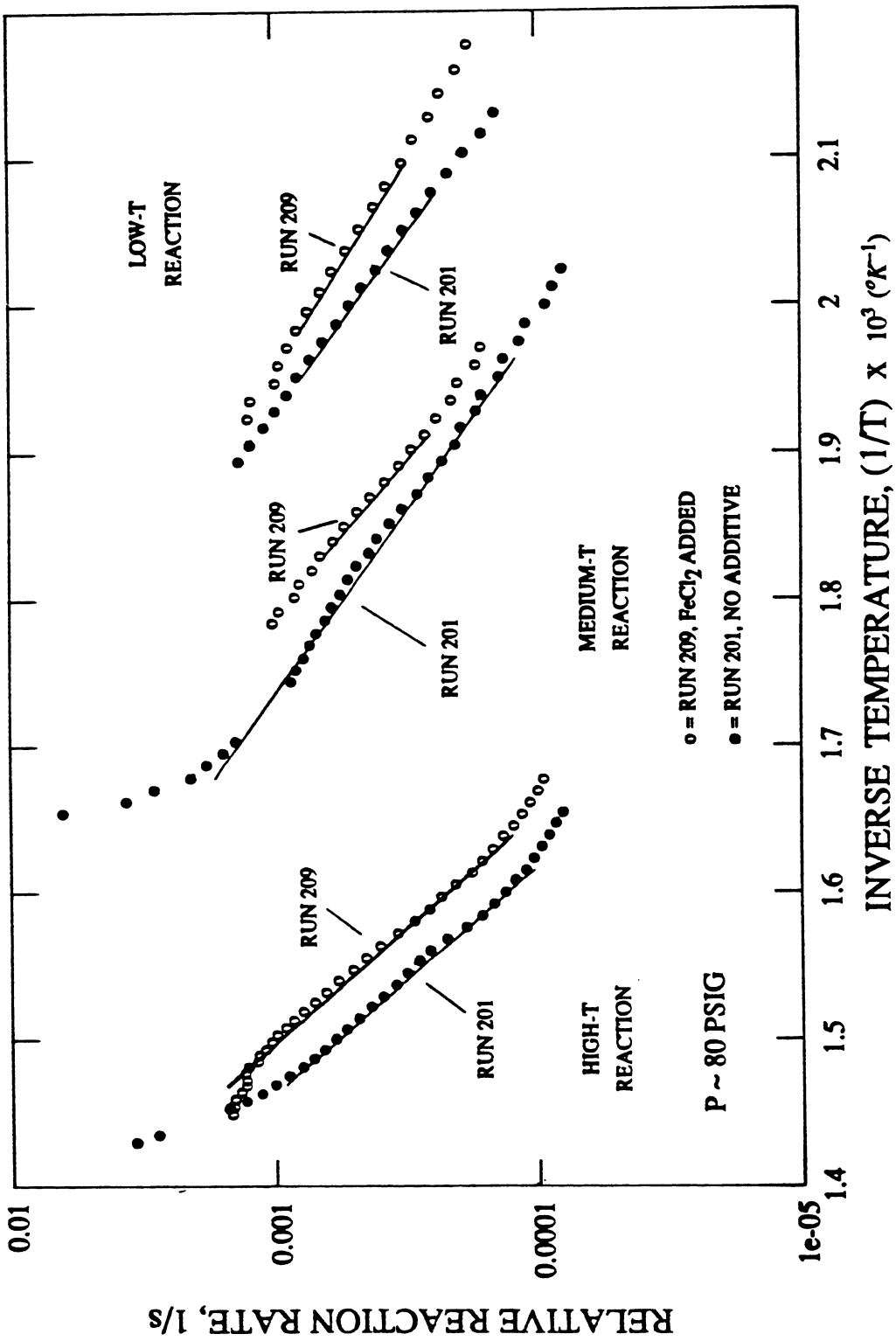

Fig. 6-24b. Effect of $FeCl_2$ Additive on Arrhenius Graphs:
Run 201 (No Additive) and Run 209 ($FeCl_2$ Added).

metallic additive was present. From comparison of the slopes of these graphs, it is apparent that addition of these compounds resulted in a lower activation energy (slope) for the low temperature reaction; hence, increased low temperature oxidation and fuel deposition. A higher activation energy is apparent at medium temperatures, which resulted in a higher, narrower medium temperature oxidation peak (Fig. 6.8). No significant change occurred in the activation energy of the high temperature reaction; however, the increased fuel deposition at low temperature led to higher reaction rates in the high temperature reaction as reflected in the larger pre-exponential constant (intercept) in Fig. 6.24b.

Figure 6.25a shows a comparison of effluent gas data from Run 201 with data from Run 216 ($SnCl_2$ added), Fig. 6.13. The induced effect of stannous chloride was qualitatively similar to that of ferrous chloride (Fig. 6.24a). Oxygen reactivity was increased over the entire temperature range and the axis of the high temperature peak shifted to a lower temperature. The comparison of Arrhenius graphs for these two runs (Fig. 6.25b) shows that stannous chloride induced the same relative effects on the reaction rates as the ferrous chloride additive, as suggested by the effluent gas comparisons (Figs. 6.24a and 6.25a). That is, greater reaction rates resulted from a somewhat lower activation energy in the low temperature reaction and increased pre-exponential constants in the medium and high temperature reactions.

Figure 6.26a shows a comparison of the effluent gas data from Run 213 ($ZnCl_2$ added), Fig. 6.10, with Run 201. Increased oxygen consumption and carbon oxides production is apparent at low temperatures (below 600°K), as was the case with the iron and tin additives (Figs. 6.24a and 6.25a). Unlike the iron and tin additives, however, the introduction of the zinc compound resulted in high temperature combustion curves that were smaller in magnitude and which occurred over a broader temperature range.

An explanation for this behavior may be found by examining the effect of addition of $ZnCl_2$ on the rates of the reactions, as illustrated in the comparison of the Arrhenius graphs for these two runs (Fig. 6.26b). No significant change is seen in the activation energy of the low temperature reaction due to the addition of $ZnCl_2$, but greater reaction rates resulted from an increase in the pre-exponential constant. A larger activation energy is apparent in the medium temperature reaction, which again resulted in a higher, narrower medium temperature oxidation peak (Fig. 6.10). The addition of $ZnCl_2$ caused a smaller activation energy, however, in the high temperature reaction. The net result was that the increased amount of fuel deposited at lower temperatures was allowed to burn over a wider temperature range, hence, the broad high temperature peak seen in Fig. 6.26a.

Figure 6.27a shows a comparison of effluent gas data from Run 214 ($MgCl_2$ added), Fig. 6.11, and Run 201. Figure 6.27b compares reaction rates from the same two runs on Arrhenius graphs. The effluent gas comparisons show that the magnesium chloride exerted an effect qualitatively similar to that of zinc chloride on the Huntington Beach crude. That is, in general, low temperature oxidation and fuel deposition were increased. Again this behavior resulted from an increase in reaction rates caused by a larger pre-exponential constant in the low temperature reaction (Fig. 6.27b). The effluent gas data (Fig. 6.27a) appear to indicate a greater reactivity in the medium temperature range (between 510 and 580°K); however, this outcome was not reflected by any change in the Arrhenius graph at medium temperatures (Fig. 6.27b), as was the run with zinc (Fig. 6.26b). Thus, while the oxygen consumption curves for the zinc and magnesium runs exhibit similar behavior in the medium temperature range, the Arrhenius graphs do not. This result is contrary to logic and cannot be explained. As with zinc chloride, magnesium chloride induced a smaller activation energy (slope) in the high temperature reaction (Fig. 6.27b), thus causing the broad high temperature curves seen in Fig. 6.27a. Note that the shift in the oxygen consumption curve in Fig. 6.27a at a temperature around 450°K was caused by a re-calibration of the oxygen analyzer. Since the results here are somewhat inconsistent and contrary to logical expectations, they may be wrong due to calibration drift on the gas analyzers. It would be well to repeat this run to check its validity.

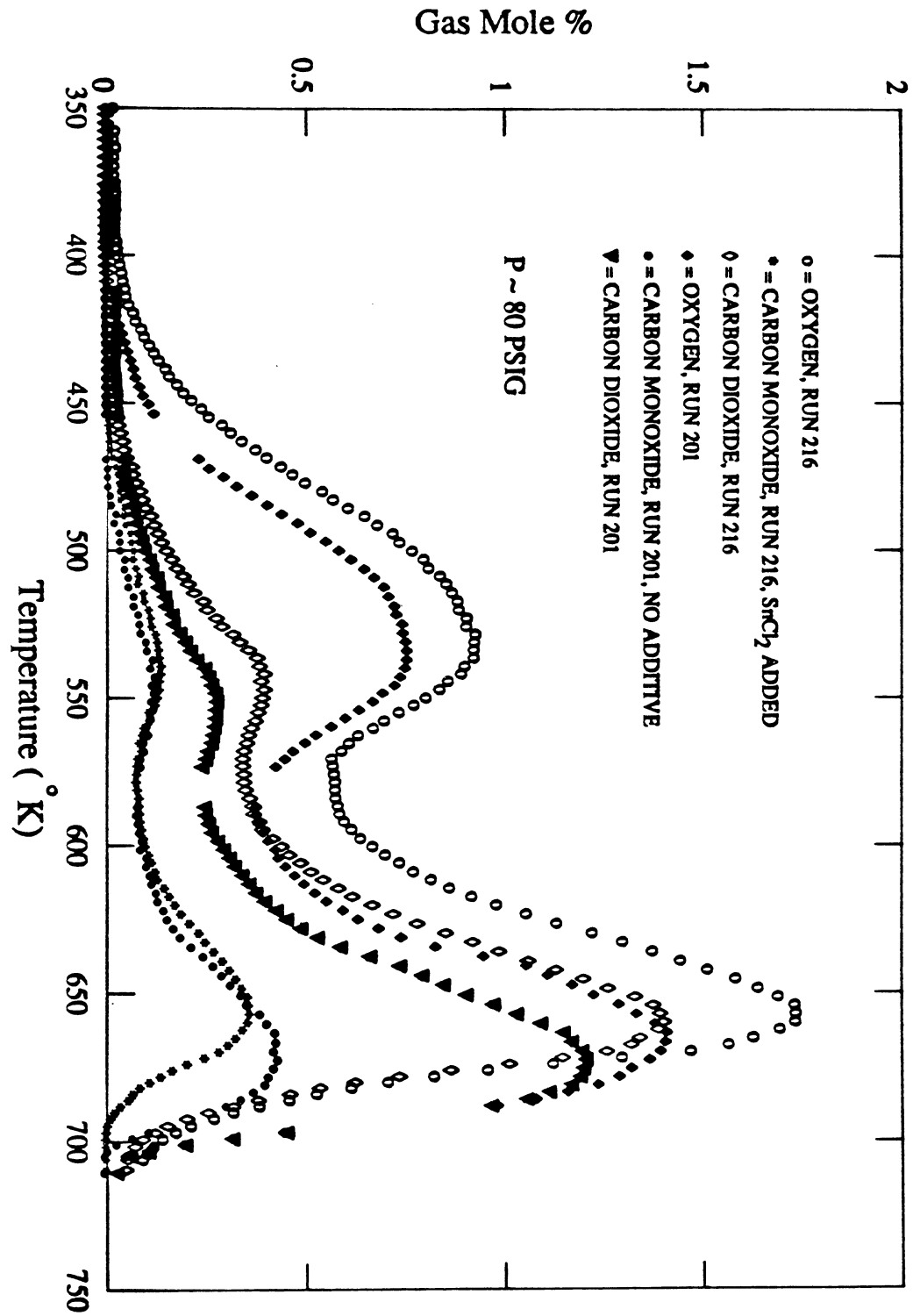

Fig. 6-25a. Effect of $SnCl_2$ Additive on Effluent Gas Composition: Run 201 (No Additive) and Run 216 ($SnCl_2$ Added).

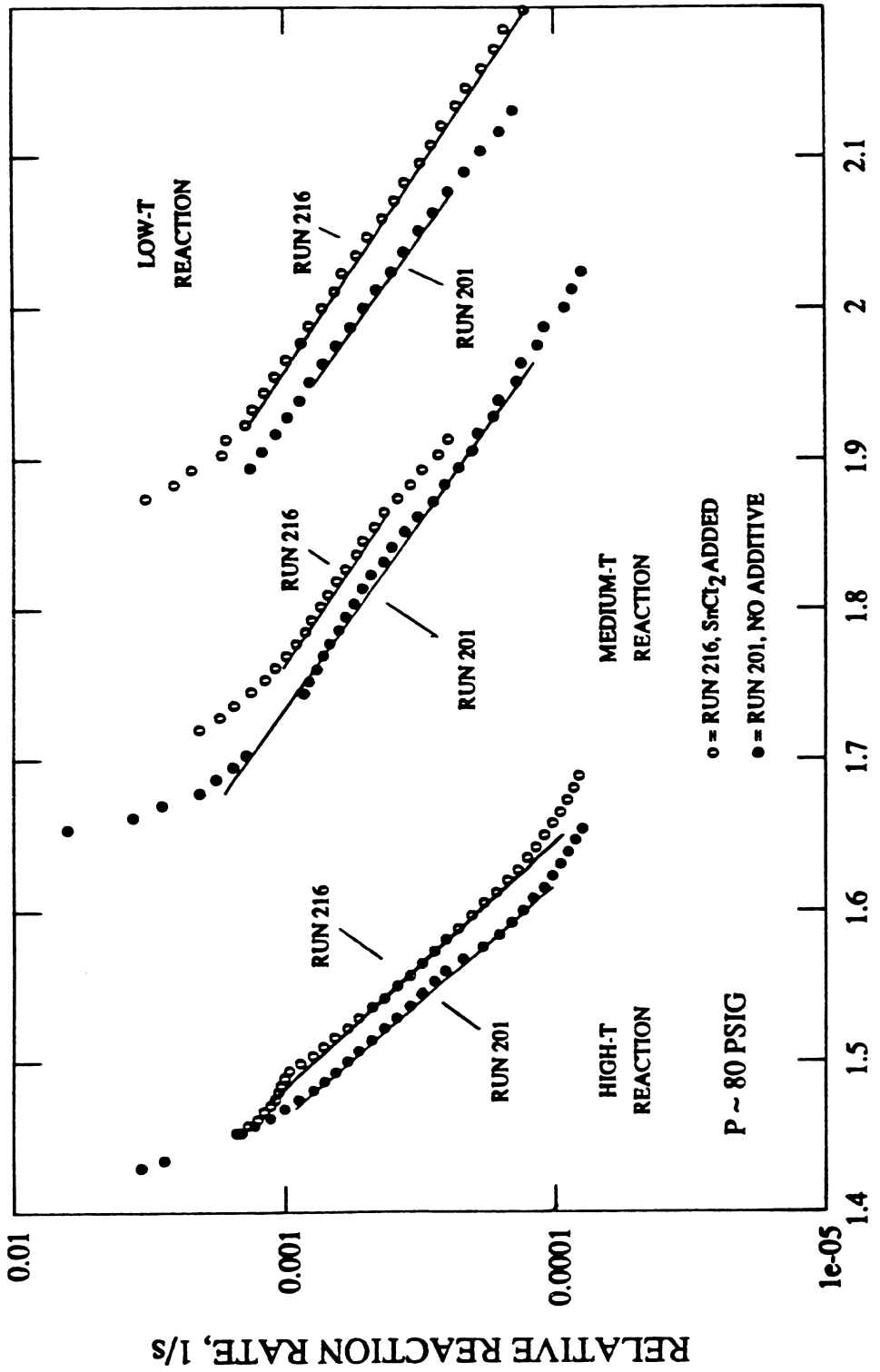

Fig. 6-25b. Effect of $SnCl_2$ Additive on Arrhenius Graphs: Run 201 (No Additive) and Run 216 $SnCl_2$ Added).

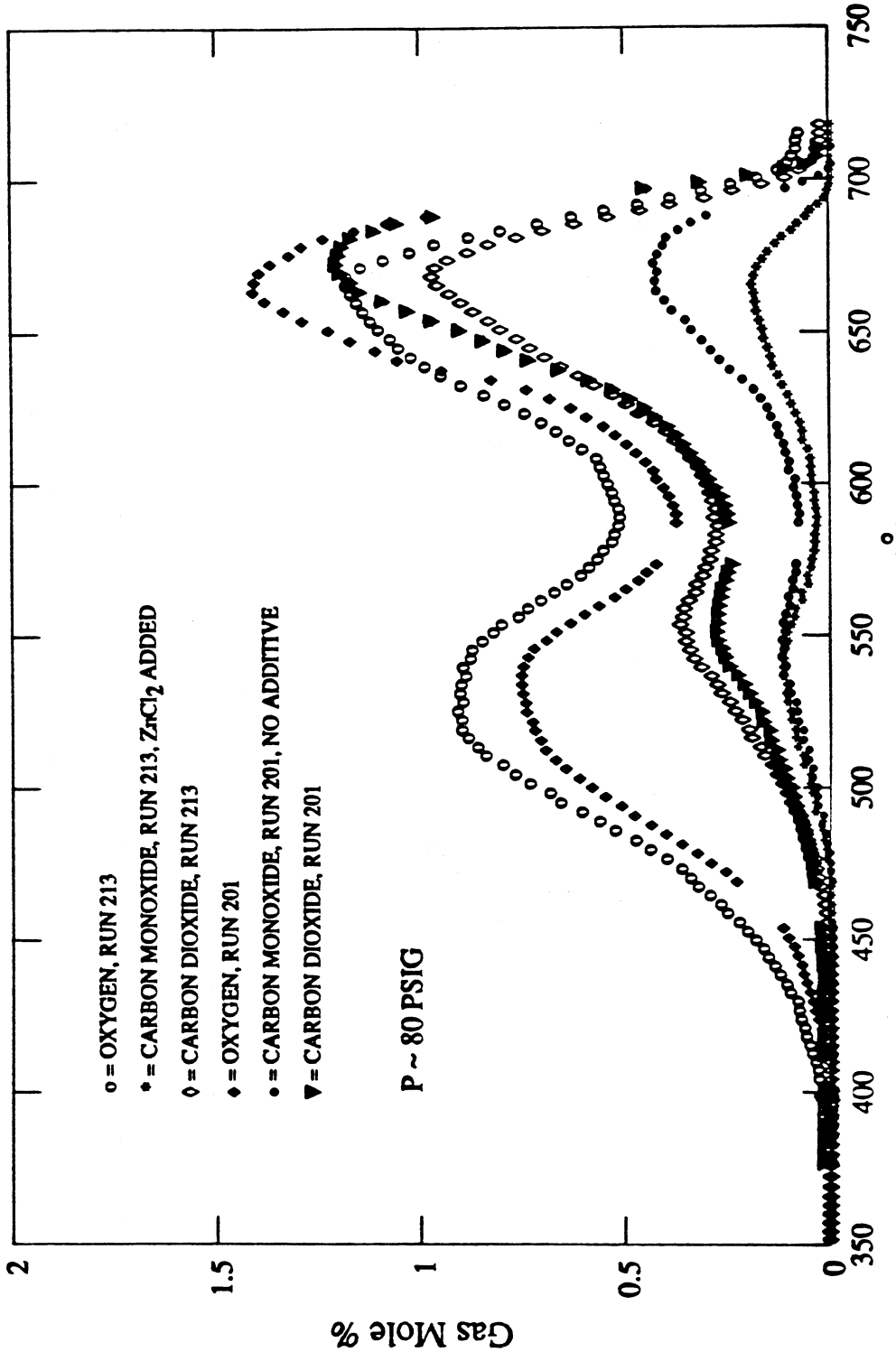

Fig. 6-26a. Effect of $ZnCl_2$ Additive on Effluent Gas Composition: Run 201 (No Additive) and Run 213 ($ZnCl_2$ Added).

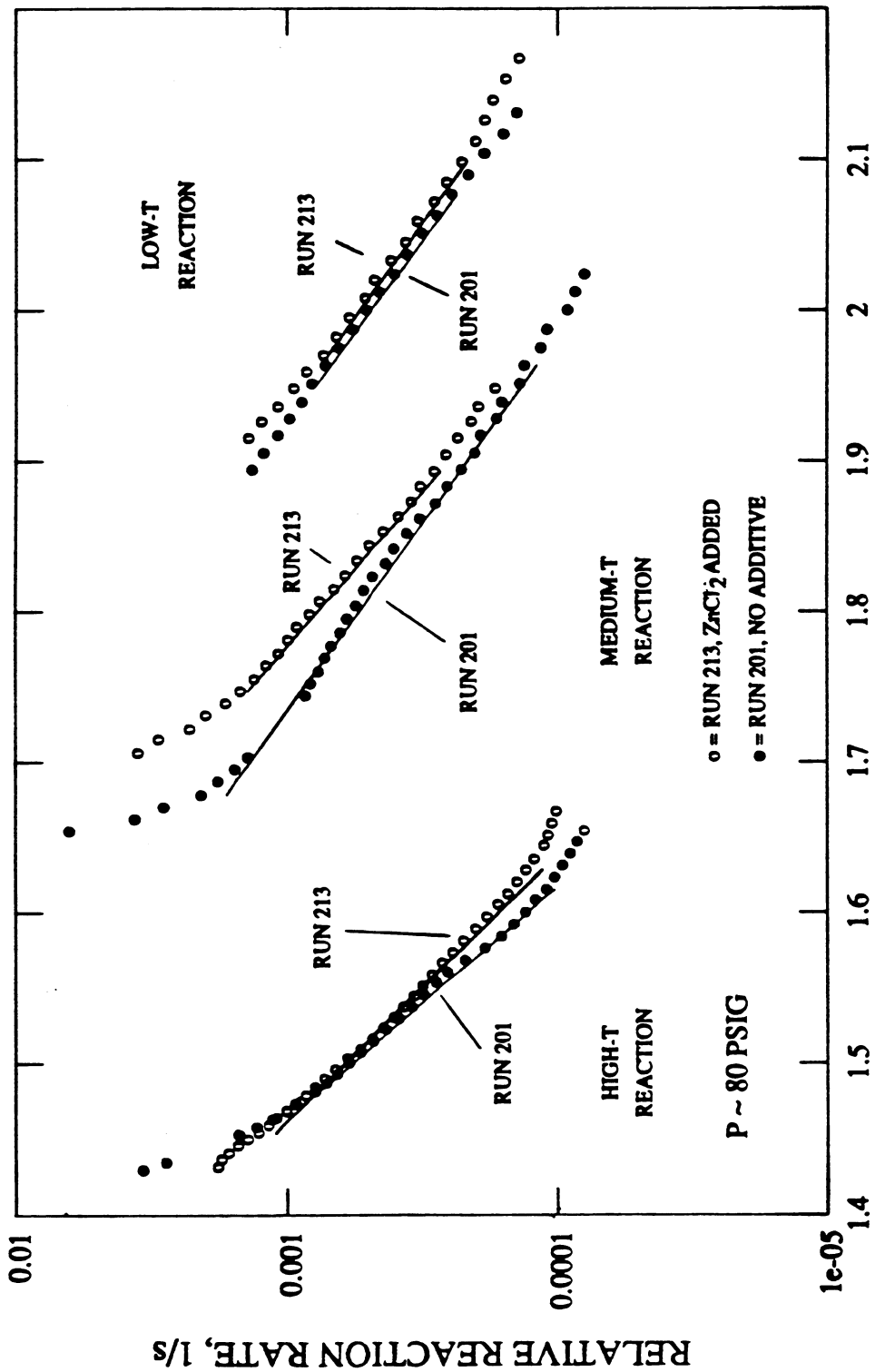

Fig. 6-26b. Effect of $ZnCl_2$ Additive on Arrhenius Graphs:
Run 201 (No Additive) and Run 213 ($ZnCl_2$ Added).

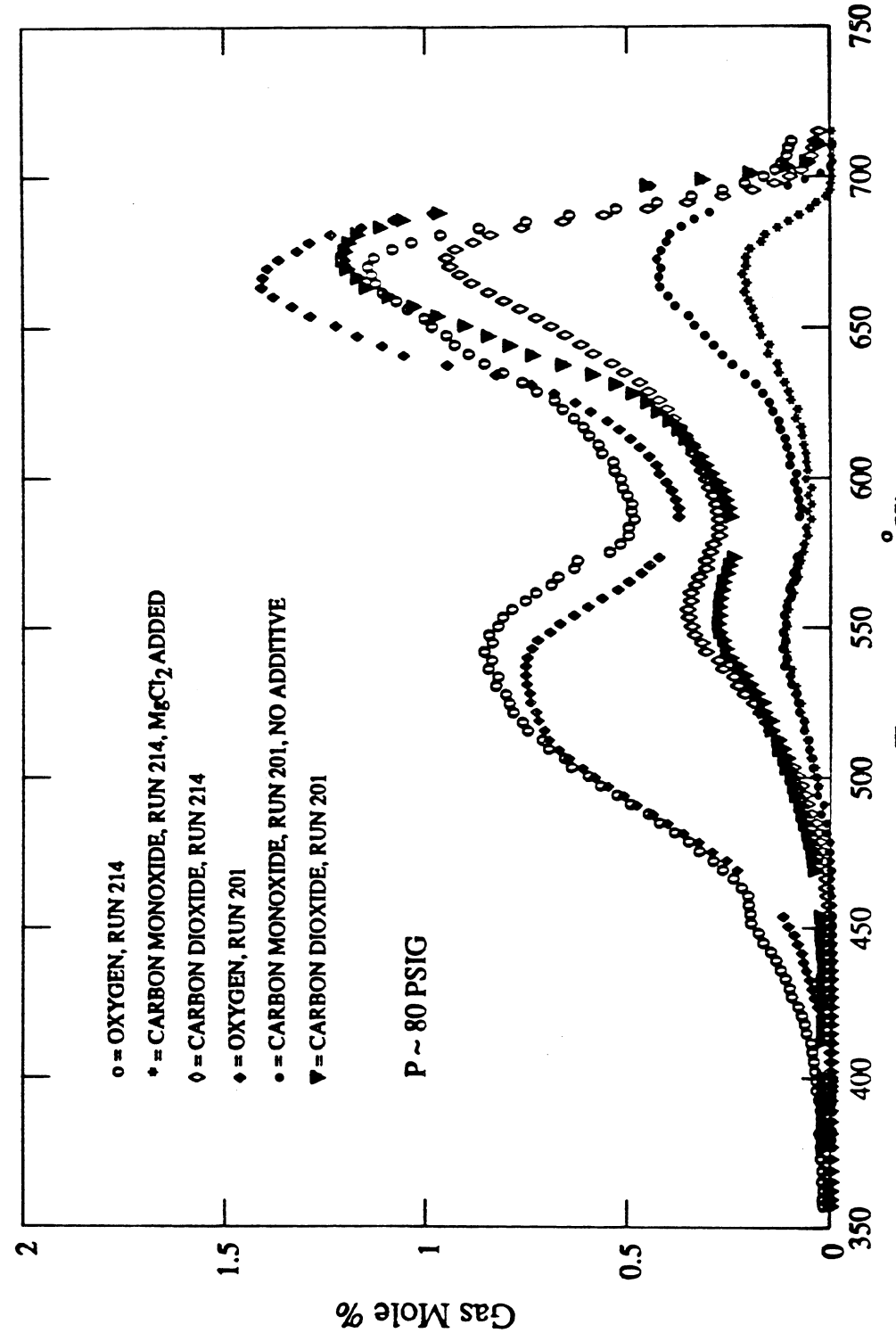

Fig. 6-27a. Effect of $MgCl_2$ Additive on Effluent Gas Composition: Run 201 (No Additive) and Run 214 ($MgCl_2$ Added).

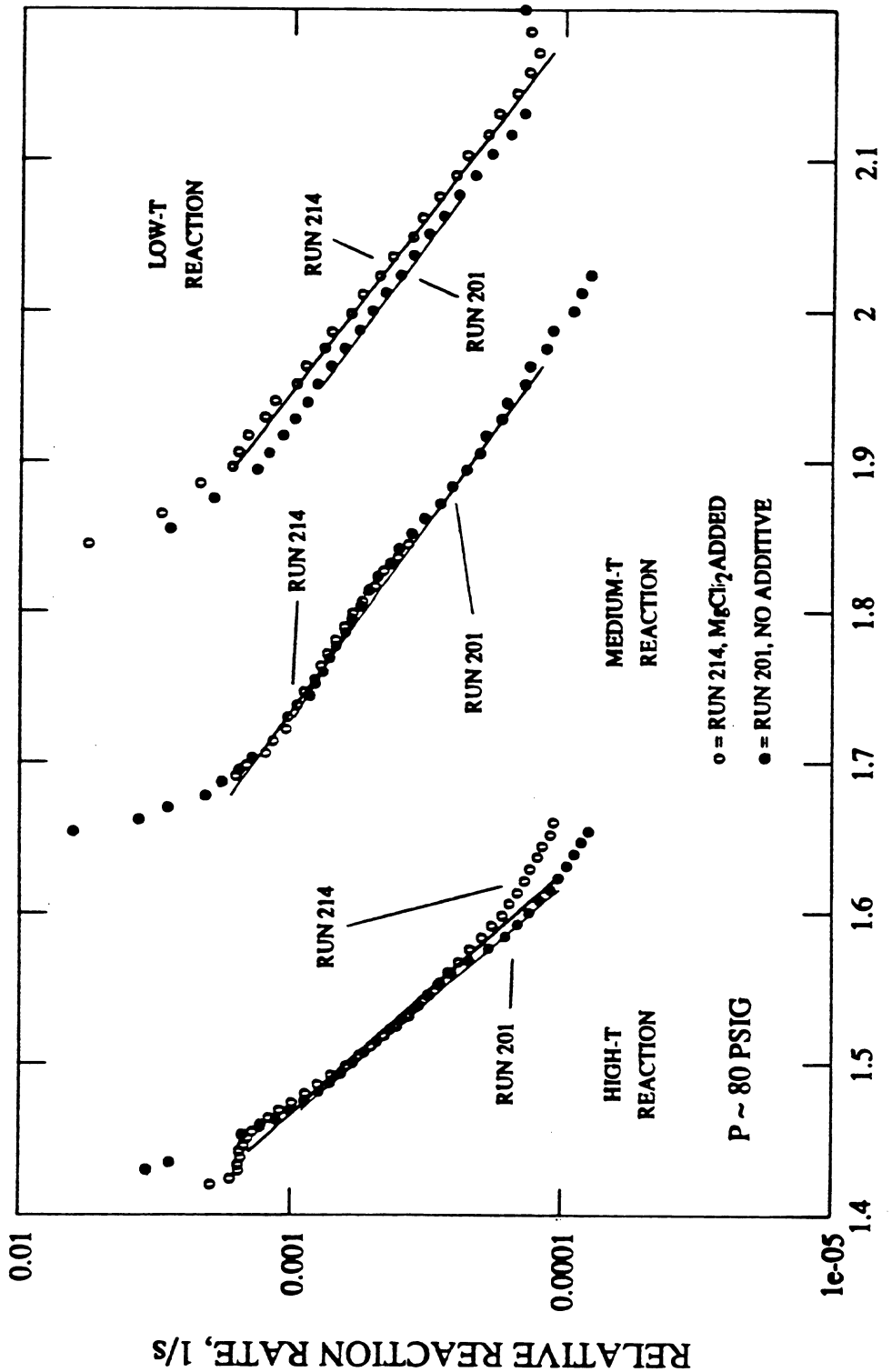

Fig. 6-27b. Effect of $MgCl_2$ Additive on Arrhenius Graphs: Run 201 (No Additive) and Run 214 ($MgCl_2$ Added).

Figure 6.28a shows the comparison of effluent gas data between Run 215 (K_2.*nr*%+1Cr_2O_7 added), Fig. 6.12, and Run 201. Figure 6.28a shows that chromium also induced an effect similar to that of the zinc compound. At lower temperatures (below 570°K) there was an increase in oxygen consumption and carbon oxides production, whereas high temperature combustion decreased in magnitude and occurred over a wider temperature range.

Again, these effects were evident as changes in the reaction rates as seen in the comparison of Arrhenius graphs (Fig. 6.28b). In the low temperature reaction, addition of $K_2Cr_2O_7$ resulted in a lower activation energy which caused increased fuel deposition. A larger activation energy in the medium temperature reaction brought about the higher, narrower medium temperature reaction peak visible in Figs. 6.12 and 6.28a. And, the lower activation energy of the high temperature reaction produced the broad high temperature peak in Fig. 6.28a by permitting the additional fuel deposited at lower temperatures to burn over a larger temperature range.

The effects of the addition of aluminum chloride on the effluent gas versus temperature data are shown in Fig. 6.29a, where data from Run 217 ($AlCl_{,nr}$%+13 added), Fig. 6.14, are plotted against data from Run 201. The effects were qualitatively similar to those induced by the iron and tin additives (Figs. 6.24a and 6.25a), but to a lesser degree. At temperatures below 570°K, oxygen consumption increased, but carbon oxides production appeared to be unaffected. At higher temperatures, oxygen consumption was again greater with the aluminum additive, and the axis of the peak appeared to shift to a slightly lower temperature. The carbon dioxide curve at high temperature mimicked the behavior of the oxygen curve; however, carbon monoxide production decreased, perhaps indicating a more efficient burn.

The comparison of Arrhenius graphs for Runs 201 and 217 (Fig. 6.29b) shows a lower activation energy (slope) for the low temperature reaction, thus yielding the increased oxygen reactivity seen below 540°K in Fig. 6.29a. The activation energies of the medium and high temperature reactions appeared unchanged. Increased fuel depostion at lower temperatures, however, led to increased reaction rates, as reflected in the larger pre-exponential constants of the higher temperature reactions. Thus, the effects induced by aluminum chloride on the reaction rates were similar to those caused by the iron and tin additives, but were considerably less pronounced.

The effect of adding manganese chloride to the reaction mixture is illustrated in Fig. 6.30a by comparing effluent gas data from Run 218 ($MnCl_2$ added), Fig. 6.15, to that from Run 201. No apparent change is visible in the carbon oxides curves below 600°K, but a slight increase in oxygen consumption occurred. Above 600°K, however, all three gas curves were affected. The curves were broader, smaller in magnitude, and were shifted to a lower temperature. A comparison of the Arrhenius graphs for these runs (Fig. 6.30b) shows higher reaction rates for each reaction as a result of adding manganese chloride. In the low temperature reaction, the activation energy decreased slightly, resulting in the increased oxygen comsumption below 525°K (Fig. 6.30a). A higher activation energy is apparent in the medium temeprature reaction as a result of addition of manganese chloride; however, this change was not reflected by a significant change in the effluent gas curve at medium temperatures. This behavior is contrary to the effects caused by other metals (iron, tin, zinc, and chromium) at medium temperatures and cannot be logically explained. A somewhat lower activation energy in the high temperature reaction caused the broader high temperature curves above 600°K.

Effluent gas data from Run 203 ($CuSO_4$ added), Fig. 6.6, is compared with data from Run 201 in Fig. 6.31a. Only slight changes are apparent in the reaction rates of the crude oil. The comparison of Arrhenius graphs for these runs (Fig. 6.31b) shows lower reaction rates for the low temperature reaction with a larger activation energy. This apparently led to the slightly

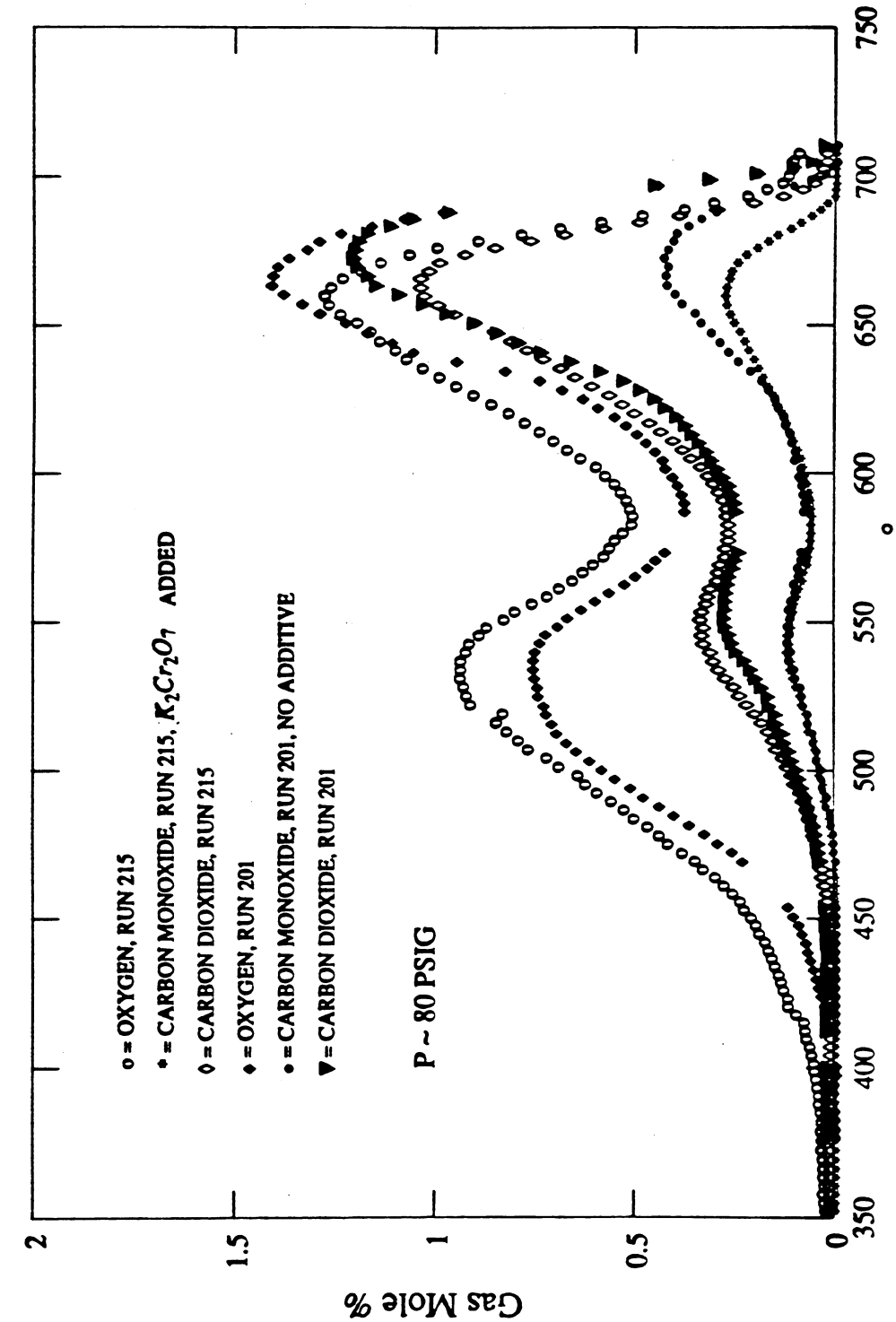

Fig. 6-28a. Effect of $K_2Cr_2O_7$ Additive on Effluent Gas Composition: Run 201 (No Additive) and Run 215 ($K_2Cr_2O_7$ Added).

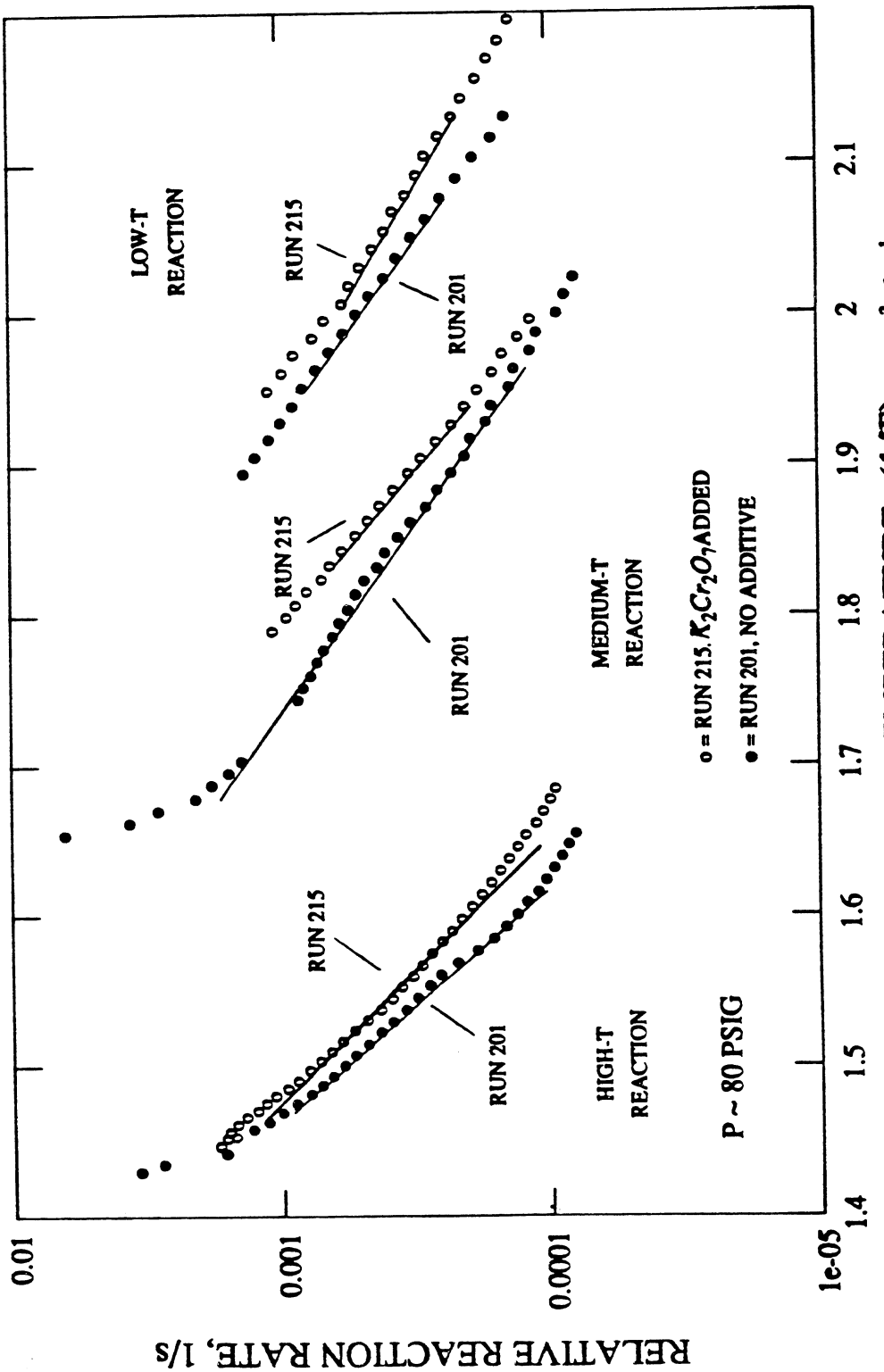

Fig. 6-28b. Effect of $K_2Cr_2O_7$ Additive on Arrhenius Graphs: Run 201 (No Additive) and Run 215 ($K_2Cr_2O_7$ Added).

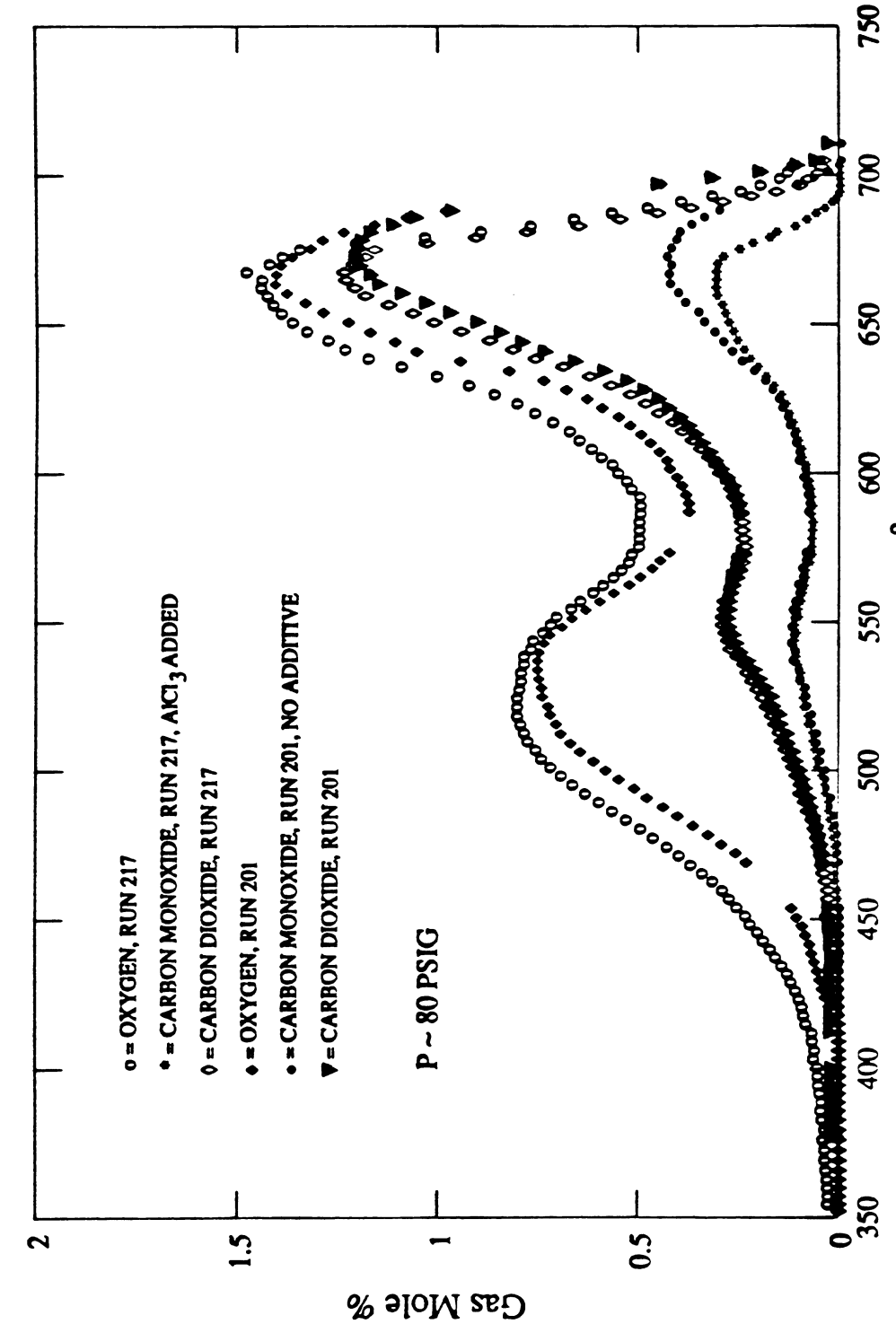

Fig. 6-29a. Effect of $AlCl_3$ Additive on Effluent Gas Composition: Run 201 (No Additive), Run 217 ($AlCl_3$ Added).

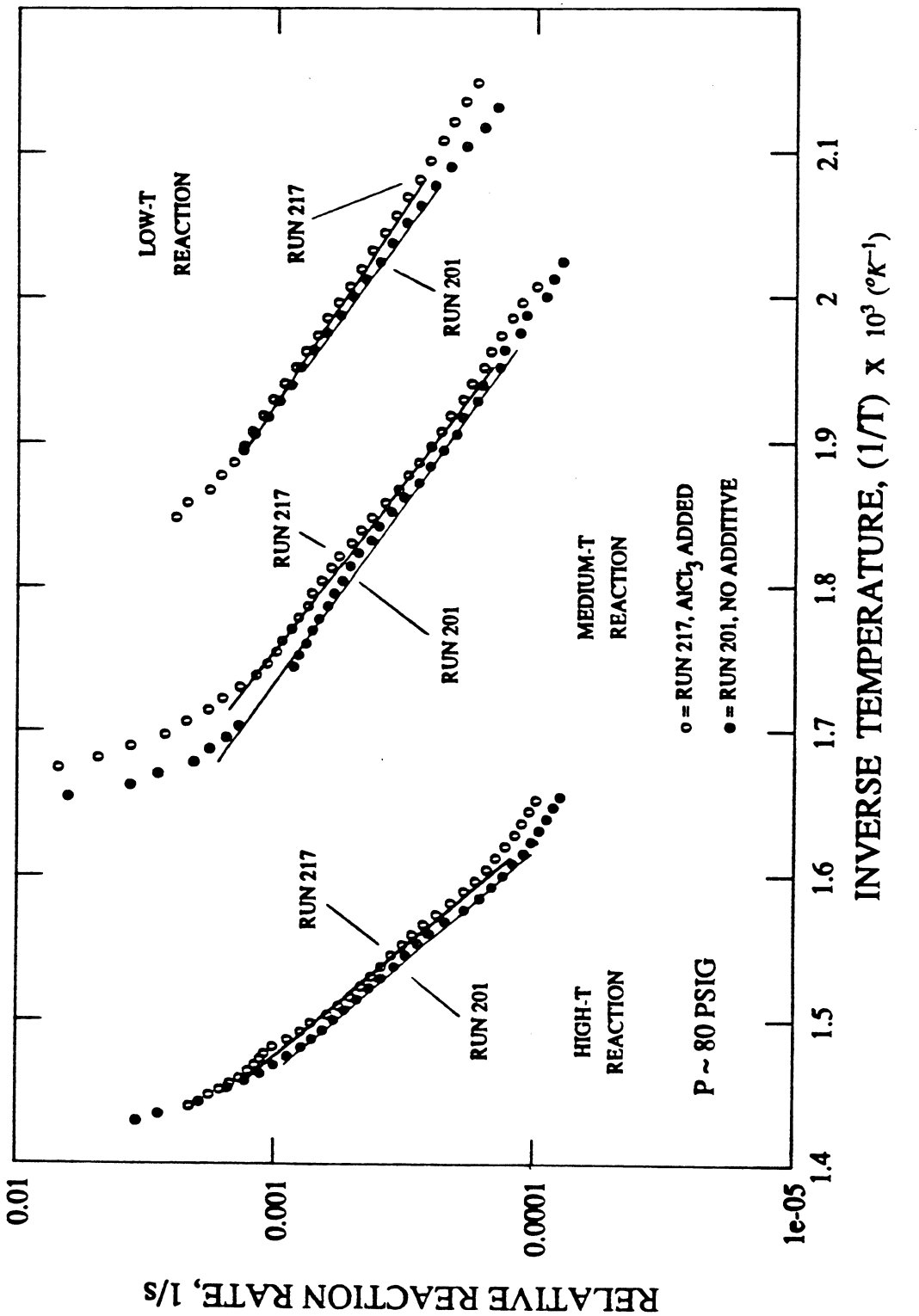

Fig. 6-29b. Effect of $AlCl_3$ Additive on Arrhenius Graphs: Run 201 (No Additive) and Run 217 ($AlCl_3$ Added).

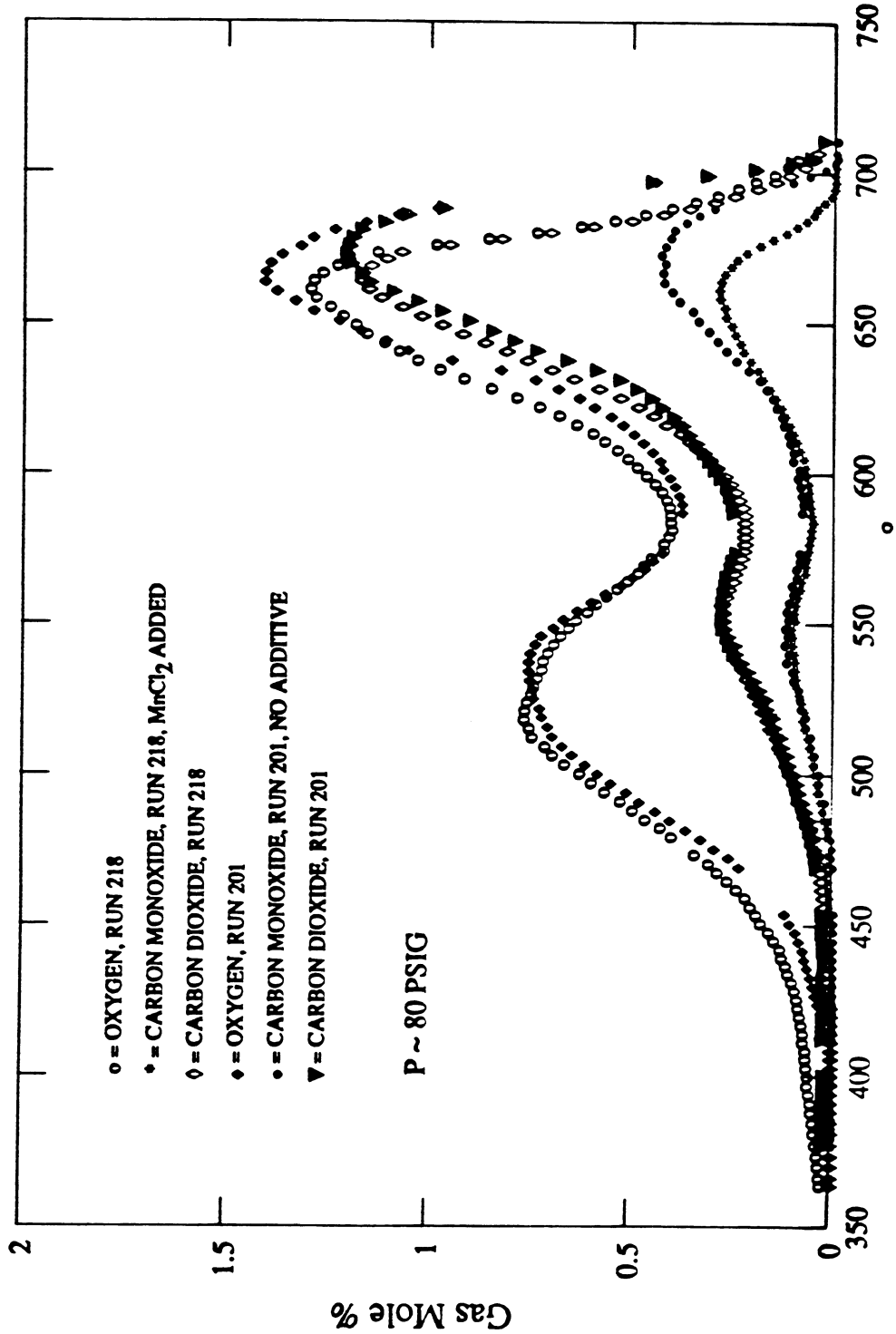

Fig. 6-30a. Effect of $MnCl_2$ Additive on Effluent Gas Composition: Run 201 (No Additive), Run 218 ($MnCl_2$ Added).

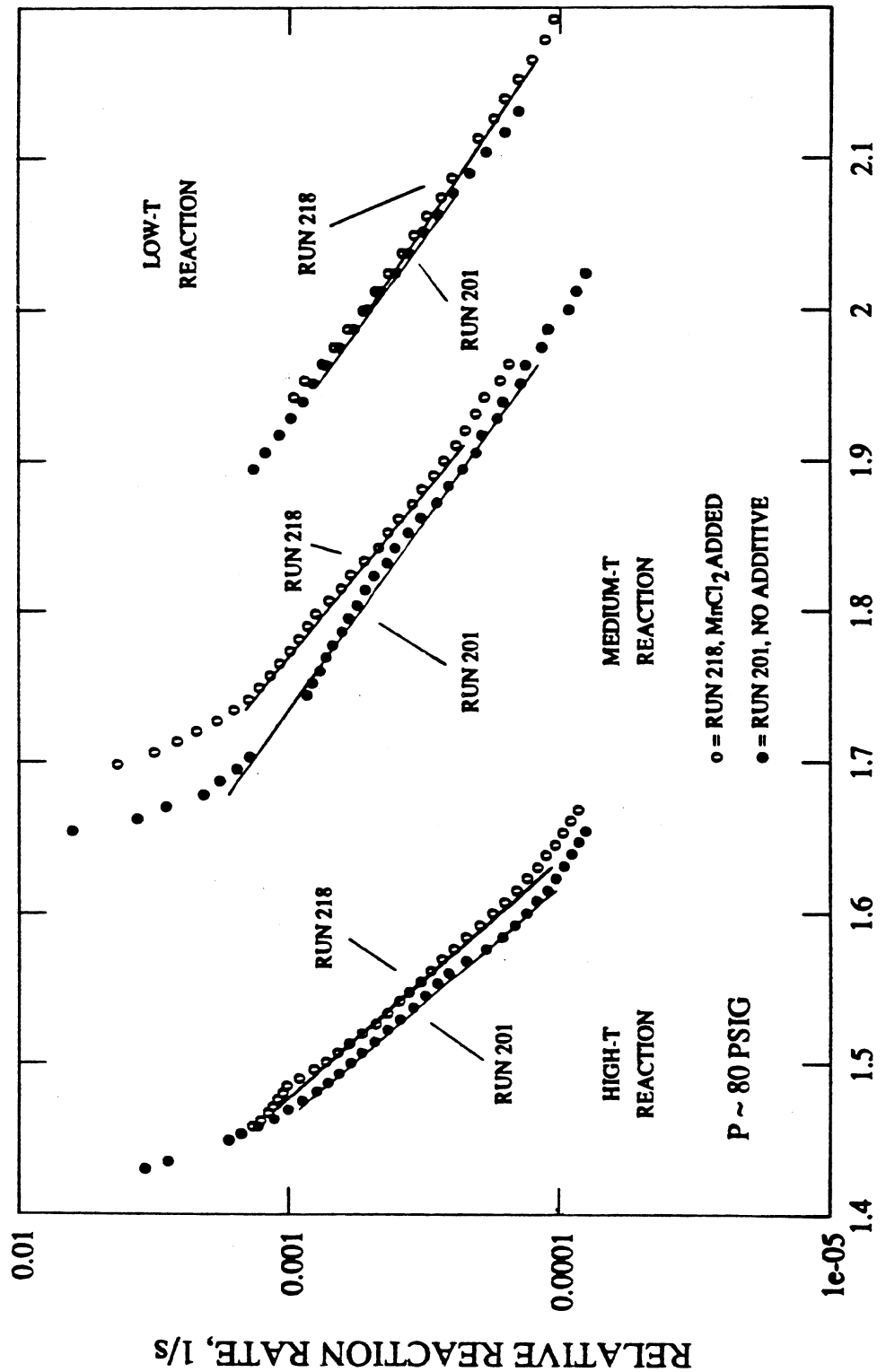

Fig. 6-30b. Effect of $MnCl_2$ Additive on Arrhenius Graphs:
Run 201 (No Additive) and Run 218 ($MnCl_2$ Added).

reduced low temperature oxidation below 500°K. No change was induced in the activation energy of the medium temperature reaction, but a smaller pre-exponential constant resulted in slightly reduced reaction rates. Reaction rates for the high temperature reaction were generally unaffected (Fig. 6.31b).

Figures 6.32a and 6.32b show that addition of nickel nitrate also had little effect on the reaction rates of the crude oil. In these figures, data from Run 222 ($Ni(NO_3)_2$ added), Fig. 6.16, are compared with data from Run 202. Slightly lower reaction rates in the low and medium temperature reactions were caused by smaller pre-exponential constants (Fig. 6.32b), but these effects were not reflected as corresponding changes in the effluent gas data (Fig. 6.32a). The sharper high temperature combustion peak in the $Ni(NO_3)_2$ curve appears to be the result of a slightly greater activation energy in the high temperature reaction.

Likewise, addition of cadmium sulfate induced only small changes in the effluent gas curves (Fig. 6.33a) and Arrhenius graphs (Fig. 6.33b). Here data from Run 225 ($CdSO_4$ added), Fig. 6.15, are compared with data from Run 202. A slightly lower activation energy in the low temperature reaction (Fig. 6.33b) caused the increased oxygen consumption witnessed in the effluent gas comparison (Fig. 6.33a). And again, the sharper high temperature reaction peak appeared to be caused by a slightly larger activation energy in the high temperature reaction (Fig. 6.33b).

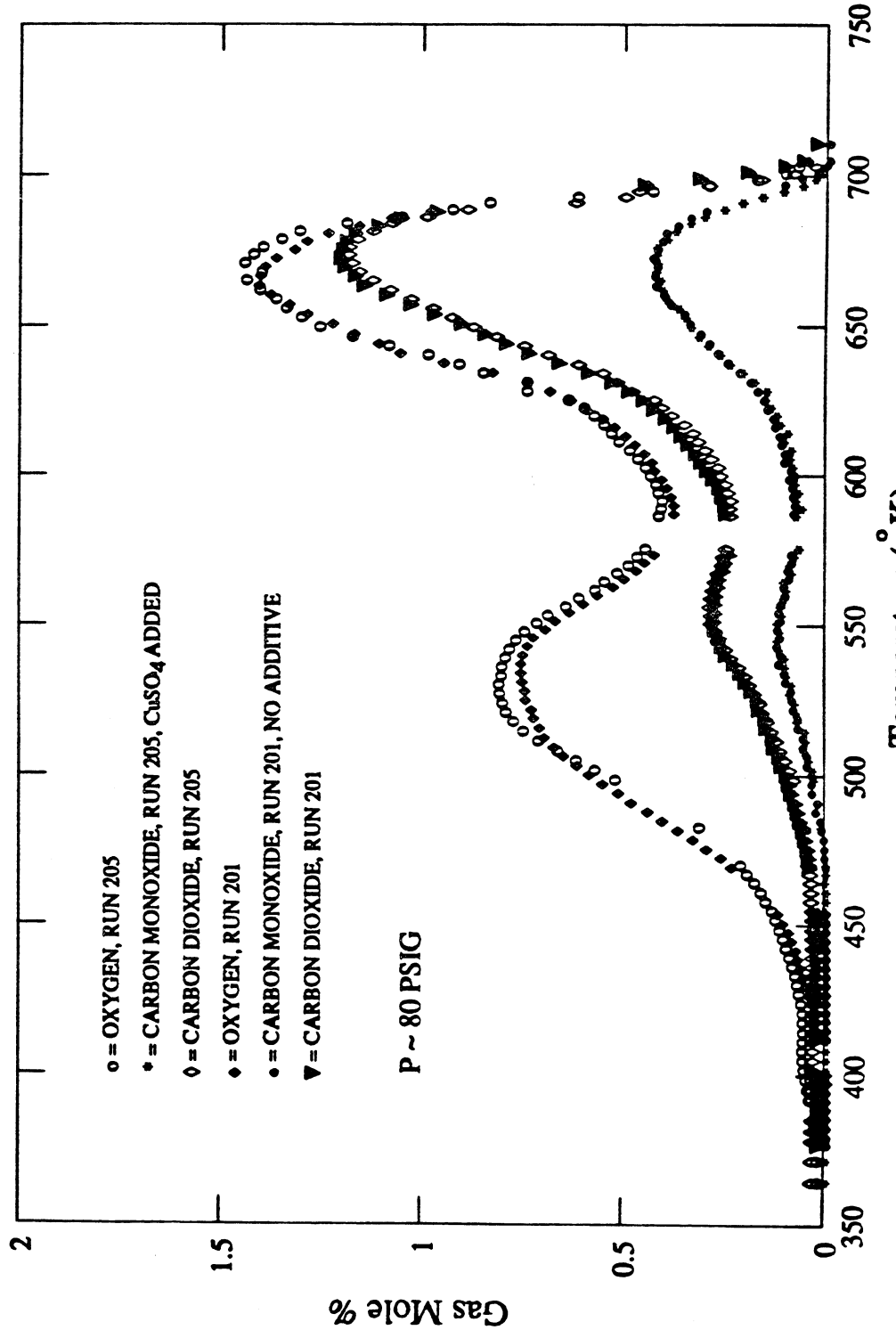

Fig. 6-31a. Effect of $CuSO_4$ Additive on Effluent Gas Composition: Run 201 (No Additive), Run 205 ($CuSO_4$ Added).

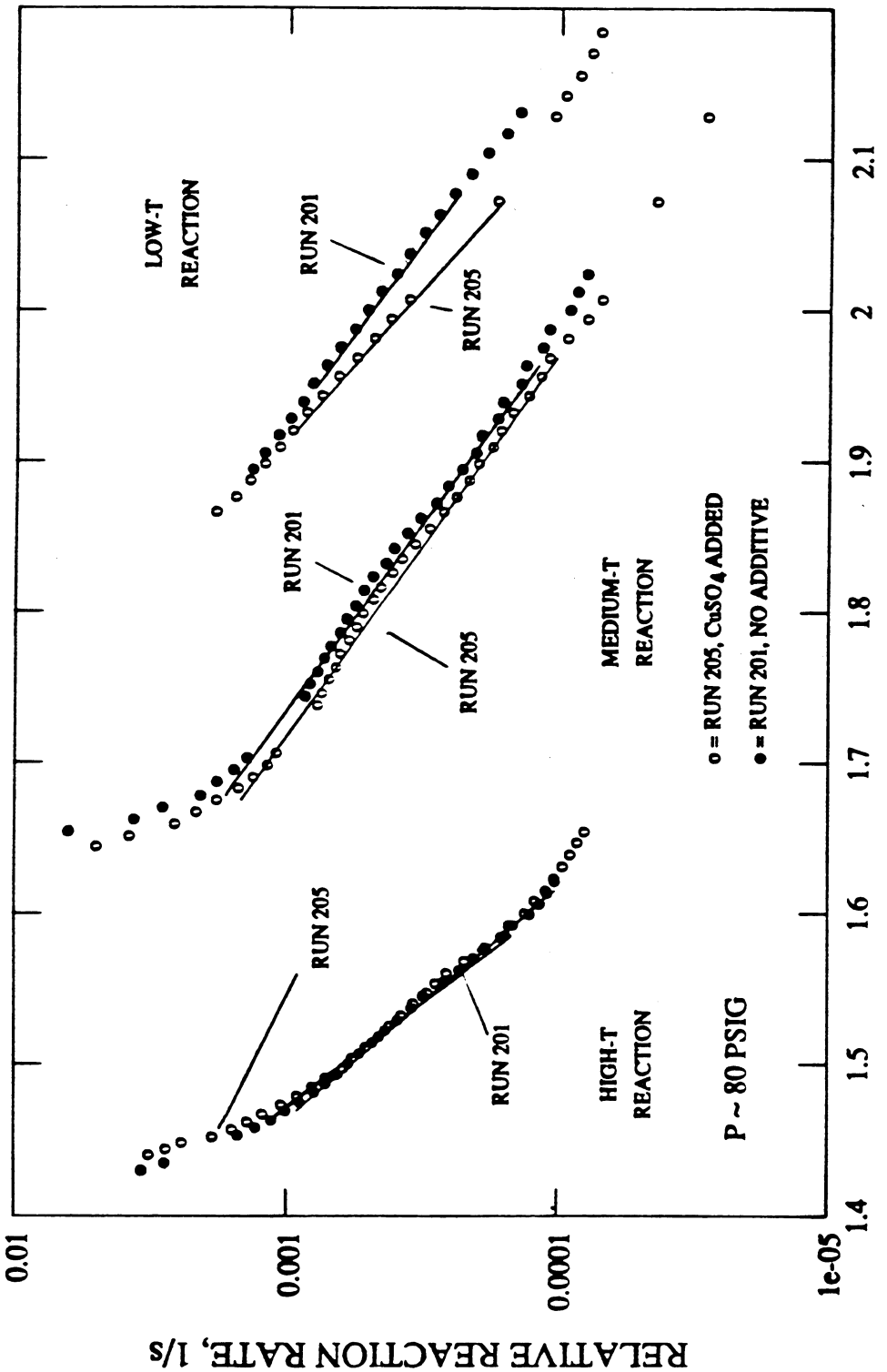

Fig. 6-31b. Effect of $CuSO_4$ Additive on Arrhenius Graphs: Run 201 (No Additive) and Run 205 ($CuSO_4$ Added).

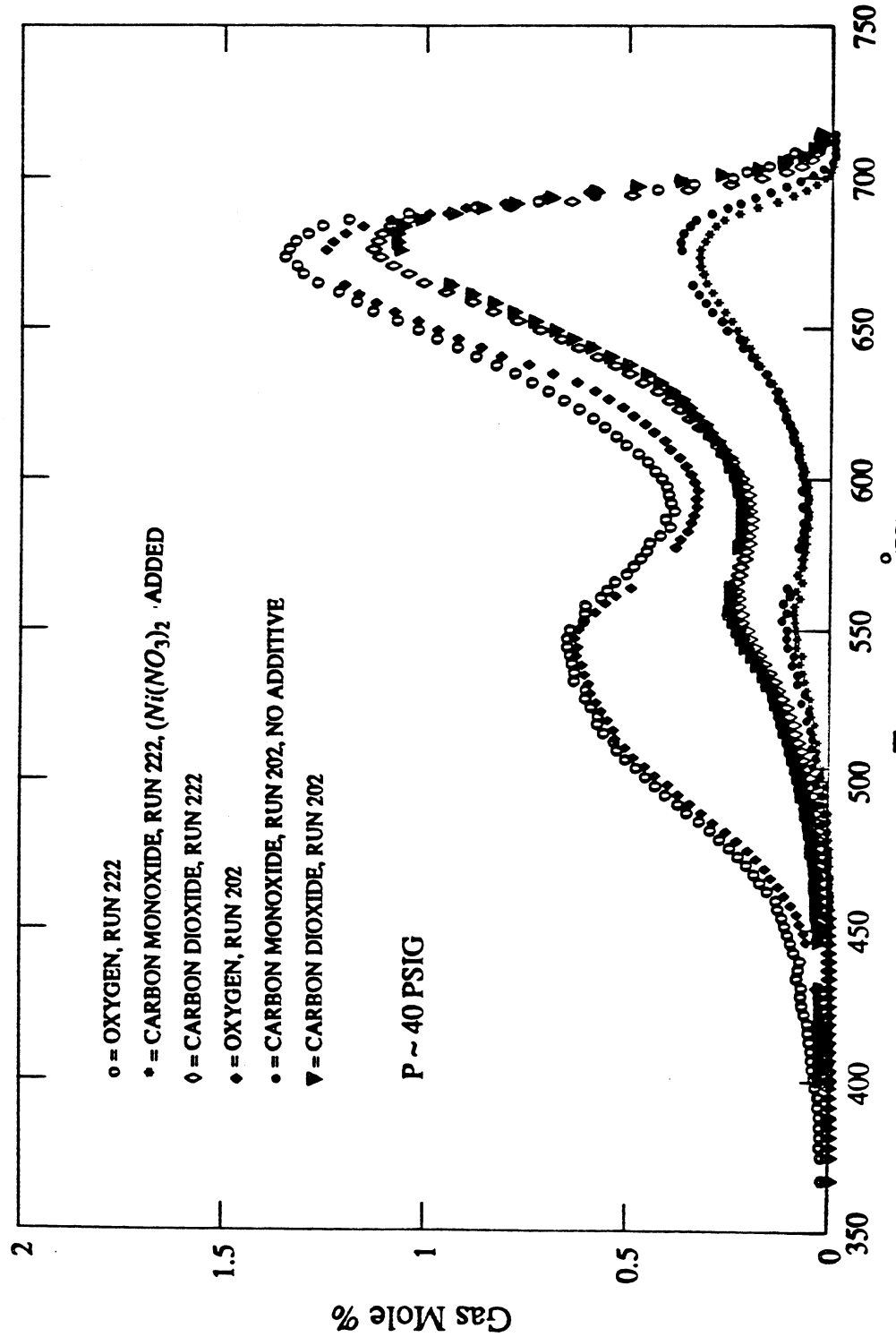

Fig. 6-32a. Effect of $Ni(NO_3)_2$ Additive on Effluent Gas Composition: Run 202 (No Additive), Run 222 ($Ni(NO_3)_2$ Added).

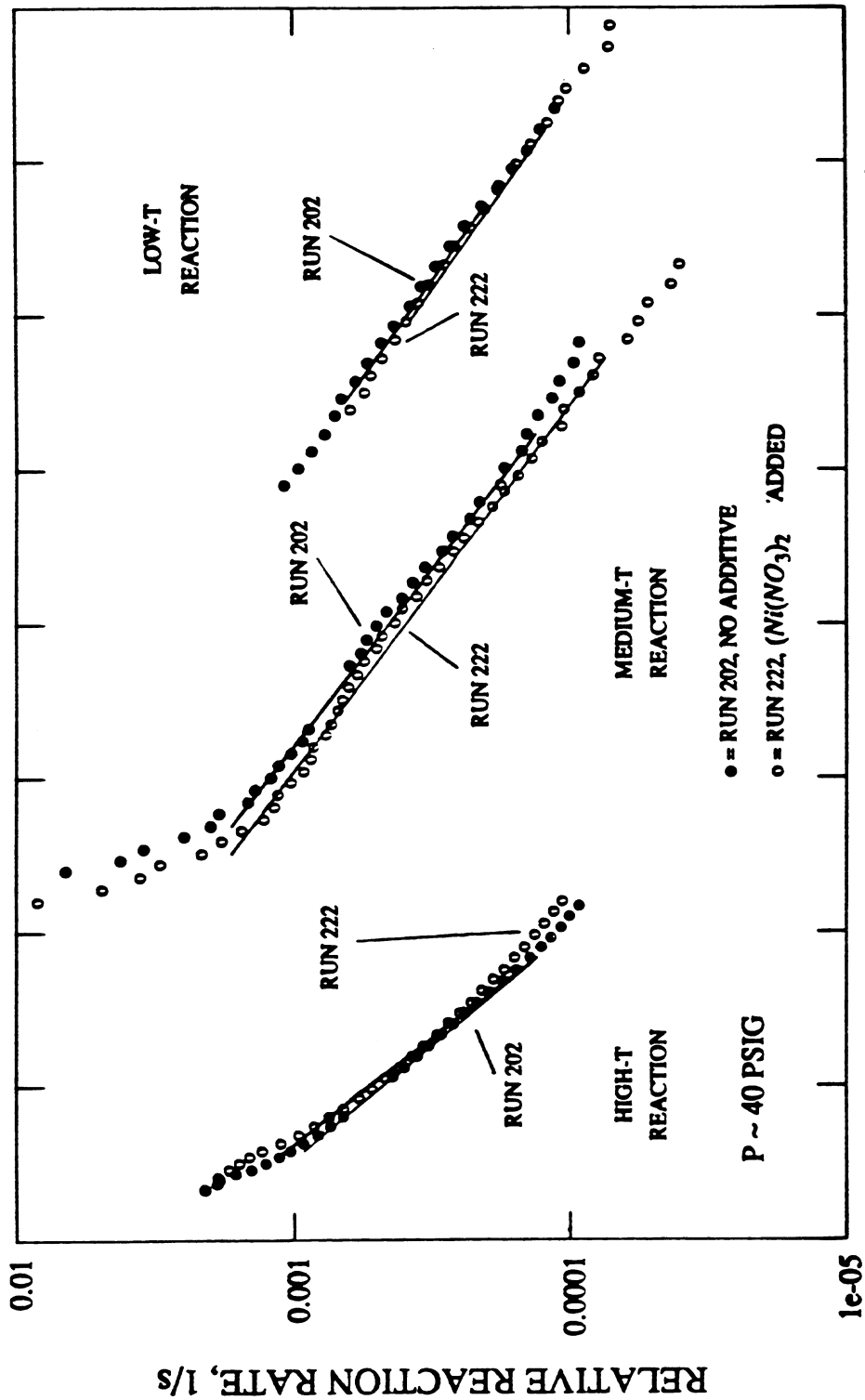

Fig. 6-32b. Effect of $Ni(NO_3)_2$ Additive on Arrhenius Graphs:
Run 202 (No Additive) and Run 222 ($Ni(NO_3)_2$ Added).

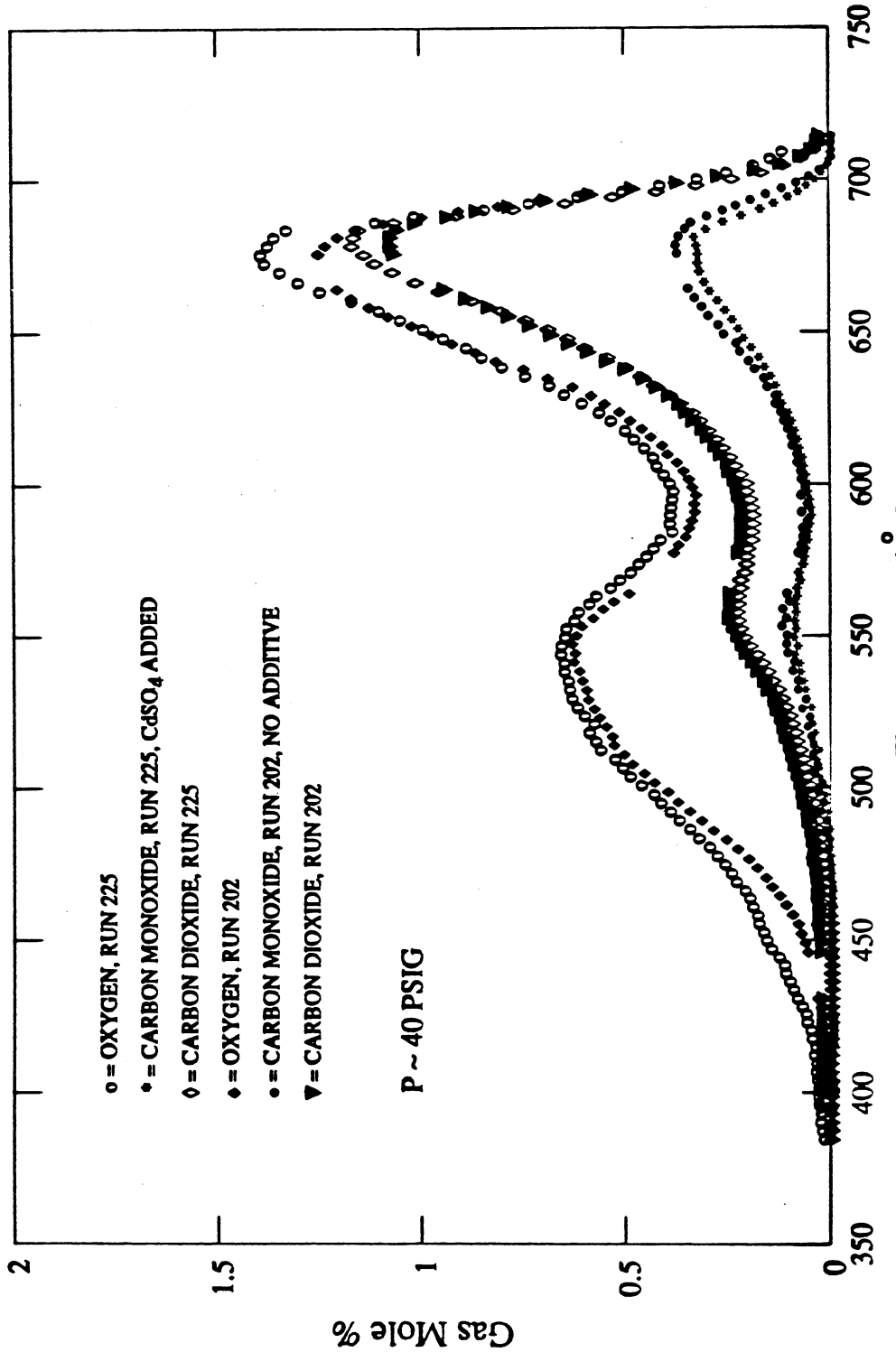

Fig. 6-33a. Effect of $CdSO_4$ Additive on Effluent Gas Composition: Run 202 (No Additive), Run 225 ($CdSO_4$ Added).

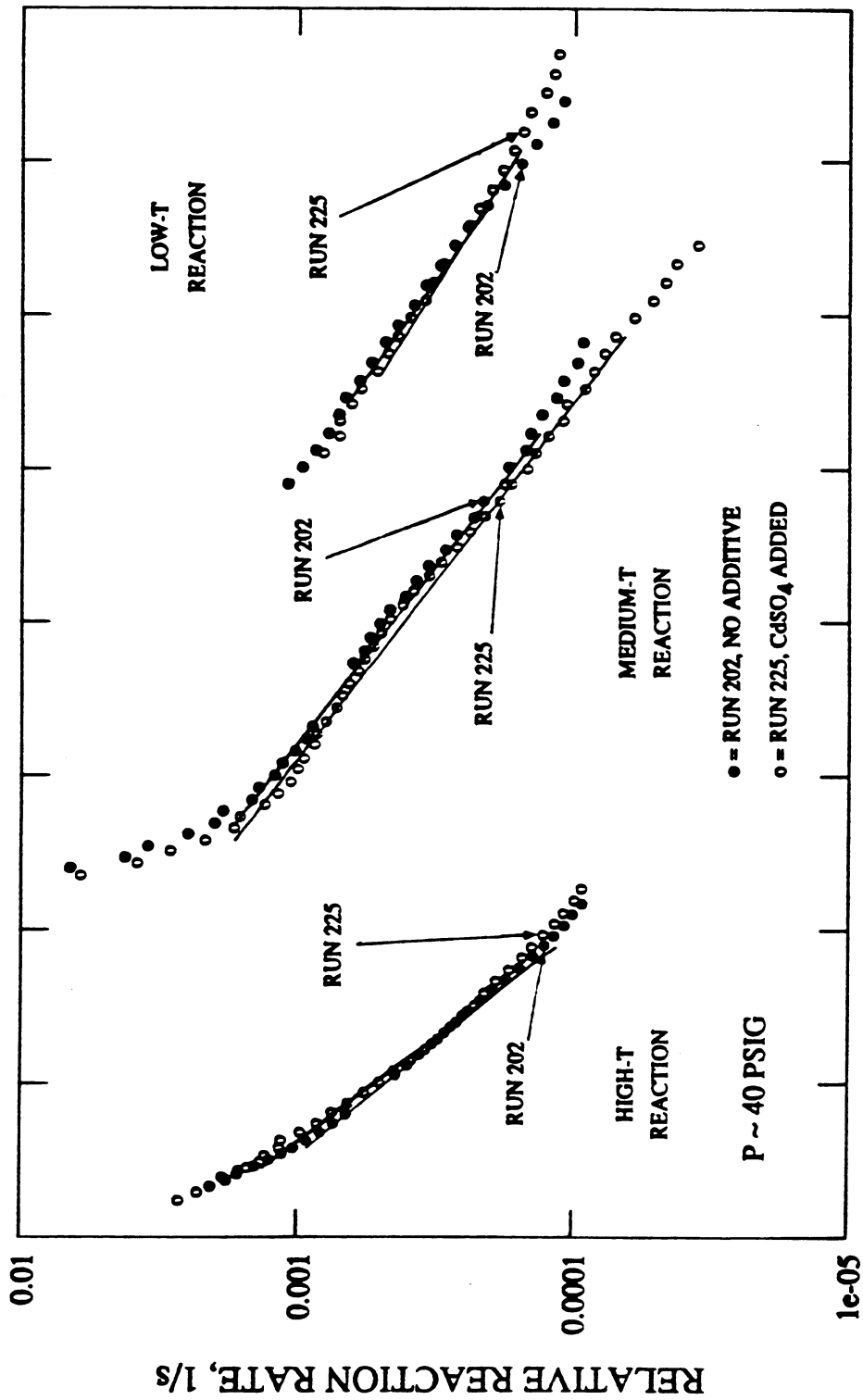

Fig. 6-33b. Effect of $CdSO_4$ Additive on Arrhenius Graphs:
Run 202 (No Additive) and Run 225 ($CdSO_4$ Added).

7. SUMMARY AND CONCLUSIONS

In this section, the results of the preceeding experimental analysis will be reviewed and summarized.

Oxygen consumption data from the kinetics experiments were analyzed by decoupling the total oxygen consumption curve into three parts representing the oxygen consumed by the three competing reactions. A curve fitting algorithm was devised in order to standardize the procedure by which the temperature ranges were chosen that characterize each reaction. This algorithm obtained optimum fits of each reaction peak by determining minimum standard deviations for data centered around oxygen consumption values that were near the peak maximum. This procedure resulted in several minima which corresponded to each centered data point. The curve fit corresponding to the minimum of these minima was selected as the best fit of the data.

The quality of resultant data matches was quite good near the reaction peaks, but was poor in the temperature range between the medium and high temperature peaks. This range of data corresponded to a temperature range in the Arrhenius graphs where none of the data aligned with the straight lines representing either the medium or the high temperature reactions. Hence, the kinetics model failed to fit the data in this temperature range. As a consequence, the kinetic parameters determined through this procedure failed to show trends consistent enough to quantitatively assess the effects of the metallic additives. These effects were therefore qualitatively evaluated through visual comparisons of the effluent gas composition data in combination with comparisons of the reaction rates as illustrated in Arrhenius graphs.

Comparisons of the effluent gas data and the Arrhenius graphs from runs at differing pressures showed that at increased pressure, oxygen consumptiom and carbon oxides production increased over the entire temperature range of the experiments. This increase in reactivity was the result of increased pre-exponential constants ($A_i P_{O_2}^m / \alpha$) for all three oxidation reactions. As expected, the activation energies (E/R) for the reactions were generally unaffected. The increase in oxygen reactivity due to higher pressure was larger when stannous chloride was present than when either ferrous chloride, copper sulfate, or no additive was present.

The presence of ferrous chloride, stannous chloride, and aluminum chloride additives induced similar effects on the oxidaton of the Huntington Beach crude oil, but to differing degrees. Addition of ferrous chloride and stannous chloride caused significant increases in the rates of oxidation, coupled to the rate with no additive, while the effects of aluminum chloride were less pronounced. Lower activation energies were found in the low temperature reaction, which in turn caused increased low temperature oxidation and fuel deposition. Greater reaction rates occurred in the medium temperature range as a result of the larger pre-exponential constants. In the case of the iron additive the activation energy was larger in the temperature range, which would ordinarily cause a lower rate, but the pre-exponential constant was so great that the reaction rate still increased. No significant changes occurred in the activation energies of the high temperature reactions due to these metals; however, the increased fuel deposition at lower temperatures led to higher reaction rates in the high temperature reaction, as reflected in larger pre-exponential constants.

Effluent gas data from runs containing compounds of zinc, magnesium, chromium, and manganese showed that they exerted similar influences on the rates of oxidation of the crude. The relative effects of these four metals varied on low and medium temperature oxidation, but generally, higher reaction rates were apparent, resulting in increased low temperature oxidation and fuel deposition. These effects were more pronounced in the cases of zinc, magnesium, and

chromium than with manganese. Each of these metals, however, caused a lower activation energy in the high temperature reaction. The net result was that the increased amount of fuel deposited at lower temperatures was allowed to burn over wider temperature ranges at high temperatures.

The addition of compounds containing copper, nickel, and cadmium produced only small changes in the effluent gas composition curves. In the case of copper, an increase in the activation energy of the low temperature reaction resulted in slightly reduced low temperature oxidation, whereas, the opposite effect was induced at low temperature by the presence of cadmium. In addition, slightly larger activation energies in the high temperature reactions resulted in somewhat sharper and narrower high temperature oxidation peaks in the cases of nickel and cadmium.

In reviewing these results, it is worthwhile to note that several of the metallic salts (iron, tin, aluminum, zinc, magnesium, chromium, and manganese) caused fuel deposition to increase, particularly iron and tin. Such metallic salts could possibly be used with higher gravity oils in an in-situ combustion process to artificially stimulate additional fuel deposition. Unfortunately, none of the additives induced the opposite effect. Had any such metallic additives been found, they would also prove to be useful in the case of low gravity oils, where excessive fuel deposition is undesirable. Still, it is logical to assume that the sensitivity of a given crude oil to the catalytic activity of a metal is highly dependent on the specific composition of that crude. Therefore, the effects of these metals, as witnessed in these experiments, may be entirely indigenous to the Huntington Beach crude and not applicable to other crudes, particularly ones of subtantially differing gravity. Studies of this type on other crudes could prove to be useful.

REFERENCES

1. Abu-Khamsin, S.: "The Reaction Kinetics of Fuel Formation for In-Situ Combustion," Ph.D. Dissertation, Stanford University (July, 1985).
2. Alexander, J. D., Martin, W. L., and Dew, J. N.: "Factors Affecting Fuel Availability and Composition During In-Situ Combustion," J. Pet. Tech. (Oct., 1962), pp. 1154-1164.
3. Bardon, C., and Gadelle, C.: "Essai de Labratoire Pour L'Etude de la Combustion In-Situ," Institute Francais du Petrole, Paris (May, 1977).
4. Bousaid, I. S., and Ramey, H. J., Jr.: "Oxidation of Crude Oil in Porous Media," Soc. Pet. Eng. J. (June, 1968), pp. 137-148; Trans. AIME, Vol. 243.
5. Burger, J. G., and Sahuquet, B. C.: "Chemical Aspects of In-Situ Combustion Heat of Combustion and Kinetics," Soc. Pet. Eng. J. (October, 1972), pp. 410-422.
6. Conner, J. E., Jr., Rothcock, J. J., Birkhimer, E. R., and Leum, L. N.: "Fluid Cracking Catalyst Contamination. Some Fundamental Aspects of Metal Contamination," Industr. Eng. Chem., Vol. 49 (1957), pp. 276-282.
7. Dabbous, M. K., and Fulton, P. F.: "Low-Temperature Oxidation Reaction Kinetics and Effects on the In-Situ Combustion Process," Soc. Pet. Eng. J. (June, 1974), pp. 253-262.
8. Donaldson, R. E., Rice, T., and Murphy, J. R.: "Metals Poisoning of Cracking Catalysts," Industr. Eng. Chem., Vol. 53 (1961), pp. 721-726.
9. Drici, O., and Vossoughi, S.: "Catalytic Effect of Heavy Metal Oxides on Crude Oil Combustion," Paper 63a presented at the AIChE National Meeting and Petroleum Exposition, Houston (March 24-28, 1985).
10. Earlougher, R. C., Jr., Galloway, J. L., and Parsons, R. W.: "Performance of the Fry In-Situ Combustion Project," J. Pet. Tech. (May, 1970), pp. 551-557.
11. Fassihi, M. R.: "Analysis of Fuel Oxidation in In-Situ Combustion Oil Recovery," Ph.D. Dissertation, Stanford University (May, 1981).
12. Gureyev, A. A., and Sablena, Z. A.: "The Role of Metals in Oxidation of Hydrocarbon Fuels in the Liquid Phase," Scientific Research Institute of Fuel and Lubricating Materials, Pergaman Press (1965).
13. Hardy, W. C., Fletcher, P. B., Shepard, J. C., Dittman, E. W., and Zadow, D. W.: "In-Situ Combustion in a Thin Reservoir Containing High-Gravity Oil," J. Pet. Tech. (Feb. 1972) pp. 199-208.
14. Nelson, T. W.,and McNeil, J. S., Jr.: "How to Engineer an In-Situ Combustion Project," Oil and Gas J. (1961), Vol. 39, No. 23, p. 58.
15. Raćz D.: "Development and Application of a Thermocatalytic In-Situ Combustion Process in Hungary," Paper presented at the European Meeting on Improved Oil Recovery, Rome, Italy (April 16-18, 1985).
16. Smith, J. M.: "Chemical Engineering Kinetics," McGraw-Hill Book Co. Inc., New York, N.Y. (1970).
17. Thomas, G. W., Buthod, A. P., and Allag, O.: "An Experimental Study of the Kinetics of Dry, Forward Combustion--Final Report," Report No. BETC-1820-1, distributed by Department of Energy (February, 1979).
18. Van Tiggelen, A., and Clement, G.: "Oxydations Radicalaires en Phase Liquide," Vol. 1, Chap. 12, Editions Technip, Paris (1981).
19. Weijdema, J.: "Determination of the Oxidation Kinetics of the In-Situ Combustion Process," Report from Koninklijke/Shell, Exploratie En Produktic Laboratorium, Rijswijk, The Netherlands (1968).

20. Wilson, L. A., Oygal, R. J., Reed, D. W., Gergins, R. L., and Henderson, J. H.: "Fluid Dynamics During an Underground Combustion Process," Trans. AIME (1958), Vol. 213, pp. 146-154.

NOMENCLATURE

A = Cross-sectional area, (cm^2)
a = Intercept of linear fitting equation
A_r = Arrhenius constant
b = Slope of linear fitting eqyation
C_f = Fuel concentration, (g fuel/100 g sand)
E = Activation energy, (J/g mole)
HPR = Hydrocarbon production rate, (g/hr)
k = reaction constant, (°C/s)
L = Length of pack, (cm)
m = Reaction order
m' = molar ratio of carbon monoxide to total carbon oxides
Me^{2+}, Me^{3+} = Metal cations
m_o = Mass of oil, (gm)
n = Reaction constant
p = Pressure , (psig)
P_{O_2} = Partial pressure of oxygen, (psig)
q = Gas flow rate, (cc/s)
R = Universal gas constant, (cal/g mole - °K)
$(R_{rr})_i$ = Relative reaction rate for i'th data point, (1/s)
$R-$ = Alkyl chain
$R\cdot$ = Alkyl radical
T = Absolute temperature, (°K)
x = Atomic hydrogen to carbon ratio in fuel
x_i = I'th value of abscissa
y_{calc} = Values predicted by model
y_i = I'th value of ordinate
w_i = I'th value of weighting factor
α = Proportionality factor
$\Delta\gamma$ = Change in molar concentration of oxygen, (mole %)
δ = Mole percent of oxygen converted to carbon oxides, (mole %), or constant controlling the distillation peak magnitude, (hr^{-1})
ε_i = I'th value of error between measured data and value predicted by a fitting equation
λ = Constant controlling the distillation peak spread, ($°K^{-2}$)
σ^2 = Standard deviation
σ^2_{new} = Modified standard deviation
τ = Constant controlling the distillation peak temperature, (°K)

APPENDIX A

DERIVATION OF MINIMIZING EQUATIONS

Kinetic parameters (i.e., E/R and $A_r P_{O_2}^m / \alpha$) for each reaction were determined from the slope and intercept of semi-logarithmic graphs of the relative reaction rate (R_{rr}) versus the inverse of temperature ($1/T$). The method of linear least squares was used to determine the best straight lines through the data. In this section, the derivation of the error minimizing equations used in the least squares fits is presented.

In general, the method of linear least squares obtains optimum data fits by assuming there is no error in the x values and by minimizing the sum of squared errors between the measured y values and those calculated from a linear fitting equation:

$$\sum_{i=1}^{n}[\varepsilon_i]^2 = \sum_{i=1}^{n}[y_{calc} - y_i]^2 = \sum_{i=1}^{n}[a + bx_i - y_i]^2 \tag{A.1}$$

The errors are minimized by setting the slopes of the sum of the squared error terms equal to zero:

$$\frac{\partial\sum[\varepsilon_i]^2}{\partial a} = na + b\sum x_i - \sum y_i = 0 \tag{A.2}$$

$$\frac{\partial\sum[\varepsilon_i]^2}{\partial b} = a\sum x_i + b\sum x_i^2 - \sum x_i y_i = 0 \tag{A.3}$$

The values of a and b corresponding to the best match of the data are therefore obtained through simultaneous solution of these equations, which implies:

$$b = \frac{n\sum x_i y_i - \sum y_i \sum x_i}{n\sum x_i^2 - (\sum x_i)^2} \tag{A.4}$$

$$a = (1/n)\sum y_i - (b/n)\sum x_i \tag{A.5}$$

The above formulation assumes that there is an equal probability of error for each data point. When this assumption is not true, weighting factors (w_i) may be applied to the minimizing equations in order to give greater consideration to the more accurate data; hence,

$$a\sum w_i + b\sum w_i x_i = \sum w_i y_i \tag{A.6}$$

$$a\sum w_i x_i + b\sum w_i (x_i)^2 = \sum w_i x_i y_i \tag{A.7}$$

When using these weighting factor equations, the values of a and b are given by:

$$b = \frac{\sum w_i \sum w_i x_i y_i - \sum w_i y_i \sum w_i x_i}{\sum w_i \sum w_i (x_i)^2 - (\sum w_i x_i)^2} \tag{A.8}$$

$$a = \frac{\sum w_i y_i}{\sum w_i} - \frac{b\sum w_i x_i}{\sum w_i} \tag{A.9}$$

In this specific application, x_i is actually $1/T$ and y_i is $log[(R_{rr})_i]$, where

$$(R_{rr})_i = \Delta\gamma \Big/ \int_{t_i}^{\infty} \Delta\gamma dt' \tag{A.10}$$

Hence, the above equations obtain a minimum of errors in $log[(R_{rr})_i]$. In fact, a minimum of errors in $(R_{rr})_i$ is desired rather than a minimum of errors in $log[(R_{rr})_i)$. Since a larger value of $(R_{rr})_i$ is more accurate in $log[(R_{rr})_i]$, the larger values of $(R_{rr})_i$ should be given greater consideration. This may be accomplished by using $(R_{rr})_i$ as a weighting factor in Eqs. A.6 through A.9.

An additional consideration is that as the integral term $\int_{t_i}^{\infty} \Delta\gamma dt'$ decreases, the error in $(R_{rr})_i$ increases. Consequently, each value of $(R_{rr})_i$ should be weighted by $\int_{t_i}^{\infty} \Delta\gamma dt'$ so that when the integral is small, the term will not be weighted as heavily. Hence, instead of using $(R_{rr})_i$ as a weighting factor, the relative accuracy of Rrr_i [which is $(R_{rr})_i \int_{t_i}^{\infty} \Delta\gamma dt'$] should be used. But, from Eq. 5.4 of the text:

$$(R_{rr})_i \int_{t_i}^{\infty} \Delta\gamma dt' = \Delta\gamma_i \tag{A.11}$$

Consequently, the weighting factor applied to Eqs. A.6 through A.9 is $\Delta\gamma_i$.

The minimizing equations in their final form are therefore:

$$(A_r P_{O_2}^m / \alpha)\sum \Delta\gamma_i + (E/R)\sum \Delta\gamma_i (1/T_i) = \sum \Delta\gamma_i \, log[(R_{rr})_i] \tag{A.12}$$

$$(A_r P_{O_2}^m / \alpha)\sum \Delta\gamma_i (1/T_i) + (E/R)\sum \Delta\gamma_i (1/T_i)^2 = \sum \Delta\gamma_i (1/T_i) \, log[(R_{rr})_i] \tag{A.13}$$

which implies:

$$E/R = \frac{\sum \Delta\gamma_i \sum \Delta\gamma_i (1/T_i) \, log[(R_{rr})_i] - \sum \Delta\gamma_i (1/T_i) \sum \Delta\gamma_i \, log[(R_{rr})_i]}{\sum \Delta\gamma_i \sum \Delta\gamma_i (1/T_i)^2 - (\sum \Delta\gamma_i (1/T_i))^2} \tag{A.14}$$

and:

$$A_r P_{O_2}^2 / \alpha = \frac{\sum \Delta\gamma_i log[(R_{rr})_i]}{\sum \Delta\gamma_i} - \frac{(E/R)\sum \Delta\gamma_i (1/T_i)}{\sum \Delta\gamma_i} \tag{A.15}$$

Equations A.14 and A.15 were used to obtain values of the activation energy and pre-exponential constant corresponding to the best straight line fit of the kinetic data.

APPENDIX B

EXAMPLE OF CURVE FITTING ALGORITHM HIGH TEMPERATURE DATA - RUN 201

In this section, results will be presented from the curve fitting algorithm outlined in Section 5 and the equations of Appendix A, as applied to the high temperature data from Run 201.

Figure B.1 shows high temperature oxygen consumption data from Run 201. The maximum of the curve occurs at a time of 4.80 hours. The algorithm begins with data centered around the data point that is four points to the left of the maximum (4.60 hours). First, data on relative reaction rate ($\Delta\gamma / \int_{t_i}^{\infty} \Delta\gamma dt'$) versus the inverse of temperature (1/T) corresponding to this point and the six adjacent points (4.45-4.75 hours) were used in Eqs. A.14 and A.15 to determine the activation energy (E/R) and pre-exponential constant ($A_r P_{O_2}^m / \alpha$). Next, these parameters are used to calculate a predicted oxygen consumption curve:

$$\Delta\gamma_{calc} = (A_r P_{O_2}^m / \alpha)\ exp[-(E/R)(1/T_i)] \int_{t_i}^{\infty} \Delta\gamma dt' \qquad (B.1)$$

A standard deviation (Eq. 5.9) was then calculated between the predicted and actual oxygen comsumption data.

The algorithm proceeded by including the two adjacent data points at each end of the range (4.40 and 4.80 hours) and by using these nine points to determine new values for E/R and $A_r P_{O_2}^m / \alpha$. These parameters were again used to predict another oxygen consumption curve (Eq. B.1), from which another standard deviation was determined.

The algorithm repeated the above procedure for points centered around 4.60 hours, including two additional data points each time, until a minimum standard deviation was found. Table B.1 shows the progression of these calculations. Listed in this table are the data points included in the calculation, the resulting values of E/R and $A_r P_{O_2}^m / \alpha$, and the calculated standard deviations. The minimum standard deviation for data centered around 4.60 hours corresponded to the data from 4.10 to 5.10 hours.

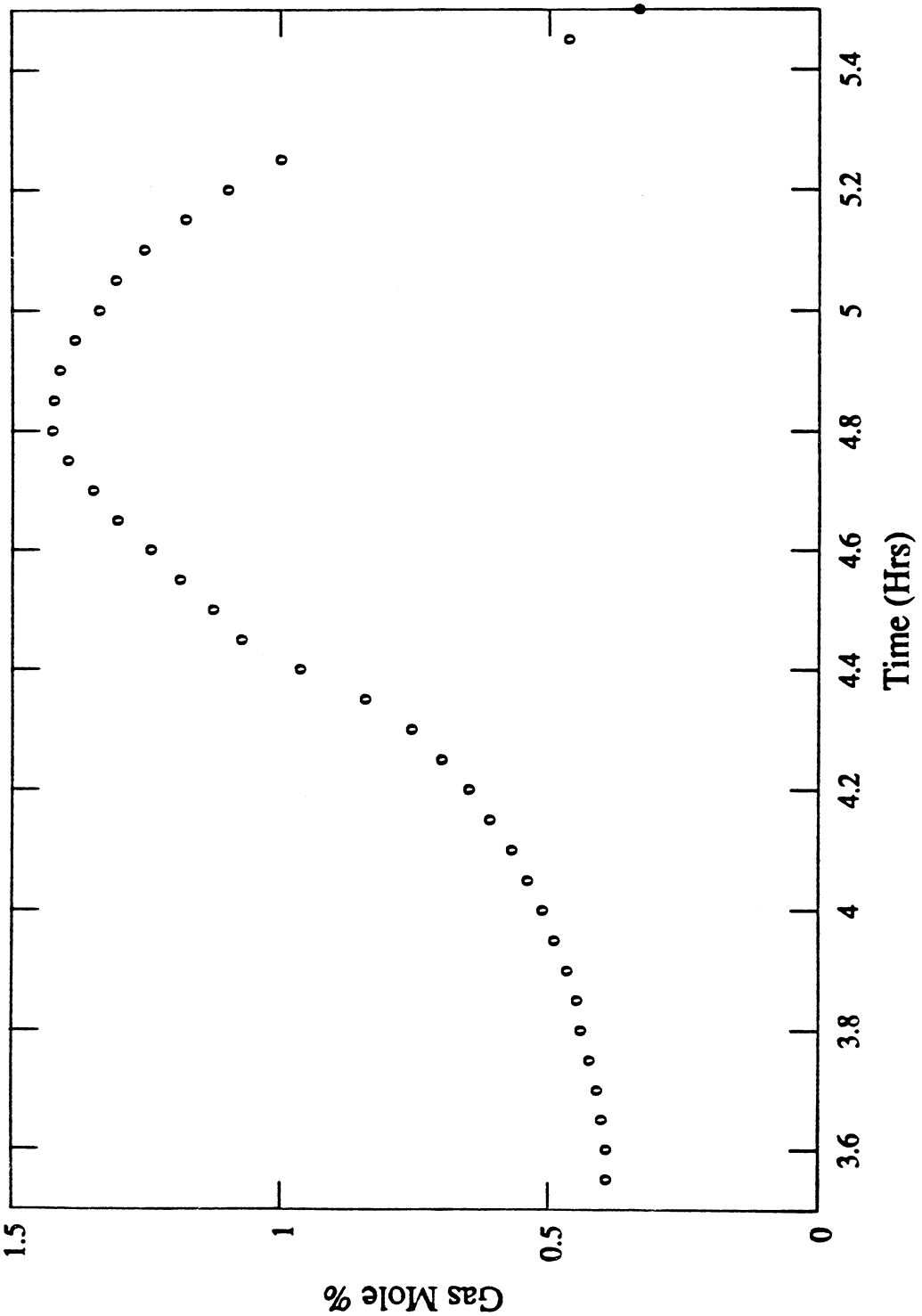

Fig. B.1. High Temperature Oxygen Consumption Data, Run 201.

TABLE B.1
PROGRESSION OF CALCULATIONS TO LOCATE MINIMUM STANDARD DEVIATION FOR POINTS CENTERED AROUND 4.60 HRS

DATA POINT RANGE (HRS)	E/R (°K)	$A_r P_{O_2}^n/\alpha$ (1/s)	STANDARD DEVIATION (MOLE %)
4.45-4.75	$1.376\ 10^4$	$5.097\ 10^5$	$2.163\ 10^{-3}$
4.40-4.80	$1.415\ 10^4$	$9.310\ 10^5$	$1.641\ 10^{-3}$
4.35-4.85	$1.452\ 10^4$	$1.642\ 10^6$	$1.370\ 10^{-3}$
4.30-4.90	$1.475\ 10^4$	$2.330\ 10^6$	$1.216\ 10^{-3}$
4.25-4.95	$1.485\ 10^4$	$2.702\ 10^6$	$1.123\ 10^{-3}$
4.20-5.00	$1.488\ 10^4$	$2.836\ 10^6$	$1.065\ 10^{-3}$
4.15-5.05	$1.492\ 10^4$	$3.019\ 10^6$	$1.035\ 10^{-3}$
4.10-5.10	$1.499\ 10^4$	$3.356\ 10^6$	$1.024\ 10^{-3}$ *
4.05-5.15	$1.503\ 10^4$	$3.591\ 10^6$	$1.026\ 10^{-3}$

* minimum standard deviation

The algorithm continues by determining minimum standard deviations, in a similar manner, for the data centered around each of the oxygen consumption values that are near the maximum; that is, in the range from 4.60 to 5.00 hours. Table B.2 lists these minima, the data point range included in each calculation, and the resulting kinetic parameters. The curve fit corresponding to the minimum of these minima (data from 4.10 to 5.10 hours) was selected as the best fit of these high temperature data. Each reaction peak in the reaction curve decomposition process was curve fitted in this manner.

TABLE B.2
MINIMUM STANDARD DEVIATIONS AND CORRESPONDING KINETIC PARAMETERS

DATA POINT CENTER (HRS)	DATA POINT RANGE (HRS)	E/R (°K)	$A_r P_{O_2}^n/\alpha$ (1/s)	STANDARD DEVIATION (MOLE %)
4.60	4.10-5.10	$1.499\ 10^4$	$3.356\ 10^6$	$1.024\ 10^{-3}$ *
4.65	4.15-5.15	$1.518\ 10^4$	$4.467\ 10^6$	$1.136\ 10^{-3}$
4.70	4.20-5.20	$1.543\ 10^4$	$6.619\ 10^6$	$1.268\ 10^{-3}$
4.75	4.30-5.20	$1.542\ 10^4$	$6.466\ 10^6$	$1.423\ 10^{-3}$
4.80	4.30-5.45 **	$1.617\ 10^4$	$2.049\ 10^7$	$1.597\ 10^{-3}$
4.85	4.40-5.45 **	$1.623\ 10^4$	$2.241\ 10^7$	$1.807\ 10^{-3}$
4.90	4.45-5.50 **	$1.692\ 10^4$	$6.318\ 10^7$	$2.237\ 10^{-3}$
4.95	4.60-5.45 **	$1.753\ 10^4$	$1.532\ 10^8$	$2.596\ 10^{-3}$

* minimum of minina
** data point range is not symetrical about the center point due to data missing during a calibration interval in the experiment.

★ U.S. GPO: 1988 561-025/80036